SIMULATION AND DEVELOPMENT OF A TRANSPORTABLE NEUTRON ACTIVATION ANALYSIS SYSTEM FOR THE ASSESSMENT OF ALUMINUM IN VIVO

by

Patrick J. Byrne

A Thesis

Submitted to the Faculty of Purdue University

In Partial Fulfillment of the Requirements for the degree of

Doctor of Philosophy

School of Health Sciences

West Lafayette, Indiana

August 2021

THE PURDUE UNIVERSITY GRADUATE SCHOOL
STATEMENT OF COMMITTEE APPROVAL

Dr. Linda Nie, Major Professor

School of Health Sciences

Dr. David Koltick

Department of Physics and Astronomy

Dr. Jim Schweitzer

School of Health Sciences

Dr. Keith Stantz

School of Health Sciences

Approved by:

Dr. Aaron Bowman

Dedicated to my family. Their support in this endeavor was everything.

ACKNOWLEDGMENTS

I would like to acknowledge the unceasing, flexible, and inclusive support of Dr. Linda Nie. I greatly appreciate her willingness to take on a part-time graduate student and sticking with what turned out to be a very long project. She has been an ideal, supportive advisor. I would like to thank the members of my committee, Drs. Koltick, Schweitzer, and Stantz, for also remaining supportive on this long journey. Finally, I would like to thank all my fellow lab mates, especially Dr. Yingzi Liu, Dr. Farshad Mostafaei, Dr. Aaron Specht, Colby Neumann, Dr. Mychaela Coyne, and Sana Tabbassum. I truly depended on their lab presence and assistance in completing all data acquisition and their camaraderie was a bonus.

TABLE OF CONTENTS

LIST OF TABLES

LIST OF FIGURES

ABSTRACT

Aluminum is present throughout the environment and in many industrial processes and consumer goods. While very useful in everyday lives, it has no inherent biological functions in humans. High quantities in the human body can be toxic, resulting a range of skeletal, neurological, and hematopoietic effects. A system has been developed to analyze aluminum using the neutron activation analysis (NAA) technique in vivo. NAA was performed with a transportable neutron generator as a neutron source and a high purity germanium (HPGe) detector for spectroscopy. The neutron generator and HPGe detector were completely modelled in MCNP6. Measurements were carried out to evaluate the accuracy of the MCNP6 simulations and to determine the detection capabilities of the system for aluminum. Simulations were also conducted to determine the acceptability of radiation dose to subjects undergoing analysis. The detection limit for the system was evaluated using skeletal bone as a long-term aluminum biomarker. The detection limit was determined to be 3.41×10^{1} μg of Al per g of dry bone for an irradiation time of six minutes. This detection level is below a point at which physiological effects have been observed in humans. A lower detection level was demonstrated to be possible with a longer irradiation time. The radiation absorbed dose was determined to be 7.30 mGy for an irradiation of six minutes. The system can therefore be utilized as a potential screening and monitoring tool for high skeletal burdens of aluminum that may lead to physiological effects.

The simulation and calculation techniques developed herein were applied to a set of human subject data that were acquired for a purpose other than evaluating aluminum. The human subject data included both bone Al from NAA and fingernail Al from mass spectrometry measurements. No significant aluminum signals were observed when assessing the in vivo NAA spectra data. Through simulation and calculation, it was demonstrated that the NAA experimental parameters resulted in an elevated detection limit for aluminum that is above Al skeletal loads observed in healthy individuals. The elevated detection limit prevented the in vivo detection of aluminum in a healthy population, thus confirming the NAA results.

CHAPTER 1. INTRODUCTION AND BACKGROUND

1.1 Aluminum

Aluminum is a lightweight, soft metal that was first isolated in pure form by Friedrich Wöhler in 1827. It is the most prevalent metal on Earth, comprising 8.1% of the crust. It is found in nature as a single stable isotope, aluminum-27, composed of 14 neutrons and 13 protons. While prevalent, it is not found in pure form naturally but is available in a wide variety of compounds including alum, feldspar, mica, clay, and bauxite ore [1]. At normal temperature and pressure (NTP), it has a physical density of 2.70 g/cm^3 and an atomic mass of 26.9815385 [2]. Being a metal, it has high thermal conductivity, good electrical conductivity, and is resistant to corrosion due to a thin, protective oxide layer that rapidly forms on its surfaces. It is frequently alloyed with another metal such as copper, magnesium, manganese, or zinc to alter its physical properties. As a lightweight, nonmagnetic, easy to weld, and non-toxic metal, it is found in a wide range of household products and industrial processes [3].

Figure 1.1 – Aluminum metal
Reproduced from https://images-of-elements.com/aluminium.php

1.2 Aluminum Exposure, Absorption, and Health Effects in Humans

Despite being the most common metal in nature, aluminum has no inherent function in the human body. This is not to say that humans are not exposed to or cannot incorporate aluminum in their bodies. Its shear ubiquity ensures exposure. In addition to being widely dispersed in the environment, it is found in a wide variety of occupational settings, medicinal uses, as well as daily practices. It is commonly found as aluminum chlorohydrate in deodorants, which many humans apply to their skin everyday as well as in over-the-counter antacid medications such as Maalox®, Gaviscon®, Gelusil®, and Mylanta® and in buffered aspirin in the form of aluminum hydroxide [4]. Medically, aluminum compounds are commonly used as phosphate binders for those undergoing dialysis to ensure their phosphorus levels remain within healthy ranges [5]. Many vaccines incorporate an aluminum salt as an adjuvant, to stimulate the immune system response [6]. It can be found to varying concentrations in drinking water and food, where an assortment of aluminum compounds are used as preservatives, coloring agents, and leavening agents [7]. Additionally, the packaging and storage of food and beverages in aluminum containers, along with the use of aluminum utensils function as further dietary sources. Overall, it has been estimated that the adult daily intake of aluminum from dietary sources in the United States is 6.9-7.2 mg/day for females and 7.2-9.4 mg/day for males [8]. A summary of non-occupational intakes of aluminum, taken from [9] is given in table 1.1.

Table 1.1 – Non-occupational daily aluminum intakes in humans

Al Exposure Source	Daily Al Intake (mg/day)	Amount Delivered Daily To Systemic Circulation
Natural Food	1-10	2.5-25 μg
Food with Al Additives	1-20	2.5-50 μg
Water	0.08-0.224	0.2-0.56 μg
Pharmaceuticals (antacids, buffered analgesics, anti-ulceratives, anti-diarrheal drugs)	126-5,000	315-12,500 μg
Vaccines (HepB, Hib, Td, DTP)	0.51-4.56	510-4,560 μg
Cosmetics, skincare products, and antiperspirants	70	8.4 μg
Cooking utensils and food packaging	0-2	0-5 μg

A variety of mining, welding, powder production, grinding, melting and other industrial processes have been shown over the years to lead to relatively high exposures to workers. Occupational exposures often result in the aluminum being available to the worker via the inhalation exposure pathway, as many processes will generate respirable dusts, fumes, and aerosols. Exposures can vary to a great degree, depending on the processes and the working environment. For example, a study of three groups of aluminum welders found those performing metal inert gas (MIG) welding were exposed to significantly higher airborne aluminum concentrations compared to those performing tungsten inert gas (TIG) welding. Although all workers were welding aluminum, the particular welding method had a significant impact on exposure, as the MIG technique generated much greater quantities of fumes [10].

While everyone is exposed to and takes in aluminum daily, the human body normally has no problem eliminating it, when functioning properly. The European Food Safety Authority reviewed all available literature and stated that the tolerable weekly intake (TWI) for aluminum should be set at one milligram of aluminum per kilogram of body weight per week, based on the lowest no-adverse-effect level observed [11]. In a healthy human, the bioavailability, that is the fraction absorbed, of aluminum is quite low. It does vary largely on exposure route, whether inhaled, ingested, or injected. Studies suggest that oral bioavailability from drinking water is most probably 0.3% and from food 0.1% [12]. Absorption is increased by low pH, which increases the solubility of the aluminum species. Additionally, the presence of small organic acids such as citrate and lactate have been shown to increase absorption, while phosphorus and silicon appear to reduce it [13]. In people with medical conditions such as uremia and celiac disease, increased aluminum absorption has been demonstrated, most likely due to higher rates of transfer across the intestinal tract [12, 14]. Bioavailability from skin exposures appears to be very low, for intact skin. A study applying aluminum directly to the skin of participants found only 0.012% absorption [15]. Transfer across a wound or non-intact skin would naturally be greater than this, although the magnitude could vary largely depending on the aluminum species and exposure conditions. Inhalation exposure to aluminum is typically only a concern for those occupationally exposed. Aluminum is present in the air, environmentally, in a range of 20-500 nanograms per cubic meter in rural areas to 1,000-6,000 nanograms per cubic meter in urban areas. Pulmonary absorption depends on the concentration in the air, the size of the particles, and the volume of air breathed. Given the range of environmental concentrations and an average

ventilation volume of 20 cubic meters per day, the average adult is only exposed to approximately 40 micrograms of aluminum per day due to inhalation [11]. The environmental aluminum tends to be insoluble, which furthers reduces the possibility of transfer to the blood. There are few studies that have assessed inhalation bioavailability, but one study did expose two individuals to aerosol particles of ^{26}Al-aluminum nitrate, with a mean aerodynamic diameter of 1.2 microns. From these exposures, the bioavailability via inhalation was estimated to be 1.9% [4].

In healthy adults, most of the aluminum they are exposed to will be readily excreted, primarily through the urinary system and to a lesser extent through the gastrointestinal tract. There is wide variation in the excretion rate among people and it does not seem to correlate with urine production. One study measured the urinary excretion in a single individual by intravenously administering ^{26}Al and found approximately 65% excreted via the urinary system within the first 24 hours and 1.3% via the gastrointestinal tract within the first 5 days [15]. A second study intravenously administered ^{26}Al to six individuals and found a range of 46.42% to 74.42% excreted within the first 24 hours via the urinary system and 1.2% via the gastrointestinal tract within the first 5 days [16]. Aluminum was found in both studies to rapidly clear from the blood. In individuals with impaired or a non-functional urinary system, the primary route of aluminum excretion is affected, and it is possible to build up significant body burdens.

Aluminum not cleared from the body will deposit in several tissues, including bone, lung, muscle, liver, brain, heart, kidney, and spleen. Measurements of body burdens in non-occupationally exposed workers are given in table 1.2, taken from [17].

Table 1.2 – Aluminum body burdens in non-occupationally exposed workers

Tissue	Concentration (mg Al per kg wet weight)
Lung	20
Bone	1-3
Liver and Spleen	1
Kidney	0.5
Heart	0.45
Muscle	0.4
Brain	0.25
Blood	0.002

Body burdens increase with age and are estimated later in life to be 20 milligrams in the lungs, 25-50 milligrams in bone and 9-24 milligrams in soft tissue, with the total burden being 50-100 milligrams [18]. Given typical organ weights, the distribution of aluminum in a 70-kilogram adult, taken from [17] is displayed in table 1.3.

Table 1.3 – Aluminum body burdens by organ in adults

Tissue	Percent Aluminum Body Burden
Bone	58
Lung	26
Muscle	11
Liver	3
Brain	0.95
Heart	0.3
Kidney	0.25
Spleen	0.2

Most measurements assessing body aluminum loads have been carried out on people either occupationally exposed to aluminum or those experiencing some medical condition such as impaired renal function, where the body's elimination of aluminum has been overcome with the intake. In such individuals, much higher tissue concentrations have been measured. In one study [11], aluminum concentrations were measured in patients with uremia and dialysis encephalopathy syndrome and compared to a control group. Marked increases were found in tissue aluminum concentrations in the patients. Another study took urine, blood, and iliac bone biopsies from two individuals who had welded aluminum for more than 20 years. The samples were analyzed using electrothermal atomic absorption spectrometry (ETAAS) and showed one worker to have a bone burden of 29 micrograms of aluminum per gram of dry weight bone and

the other worker 18 micrograms of aluminum per gram of dry weight bone. Neither worker was reported as having any known physiological or neurological problems at these skeletal aluminum burdens. The authors compared these results to 19 patients on dialysis and four control subjects without renal disease that underwent iliac bone biopsy. The patients on dialysis had an aluminum bone burden that ranged from 12 to 100 micrograms per gram of dry weight bone, and which demonstrated an increased correlation with number of years of renal failure. The four control subjects were found to have an aluminum bone burden that ranged from 0.6 to 5 micrograms of aluminum per gram of dry weight bone [19].

Several studies have attempted to evaluate whether aluminum exposures correlate with tissue burdens. One study of aluminum welders assessed the occupational aluminum air concentrations and took blood and urine samples from the workers. There was a correlation between aluminum in the air and the blood serum levels of the workers but there was poor correlation between aluminum in the air and the quantity in the urine during the work shift and subsequent 16 hours [20]. A second study compared a group of bauxite miners to a group of workers not occupationally exposed to aluminum. Blood samples were taken from both groups and analyzed with atomic absorption spectrometry, with the result that no significant differences were observed between the two groups [21]. This result indicated that any aluminum taken in occupationally was being quickly extracted from the blood and excreted. A third study compared workers in four different types of industrial processes involving aluminum to a group of workers not occupationally exposed to aluminum as well as a group of patients with renal failure undergoing dialysis. The four groups were involved in the electrolytic production of aluminum, the production of aluminum powder, the production of aluminum sulfate, and the welding of aluminum. Selecting four different types of work ensured that the workers were exposed to a variety of different aluminum compounds and particle sizes. Blood and urine samples were taken at the end of each day of work and analyzed with atomic absorption spectrometry. The patients on dialysis had the highest concentration of aluminum in their blood, not surprisingly, as the primary route of elimination was impaired. Three of the four groups of occupationally exposed workers had higher blood concentrations compared to the group of non-occupationally exposed. All four groups of occupationally exposed workers demonstrated higher aluminum concentrations in their urine compared to the non-occupationally exposed group. A correlation between urine concentration and the number of years of exposure was observed in the

welders but not in any of the other three groups. A linear relationship was seen between blood and urine concentrations among the workers but as pointed out by the authors, this affect was largely the result of a few individuals with extreme values [22].

Table 1.4 – Measured aluminum tissue concentrations in patients

	Tissue Aluminum Concentration (mg/kg dry weight)				
Patient	Bone	Muscle	Liver	Lung	Brain
Healthy Control	3.3	1.2	4.0	56	2.2
Uremia, Non-dialyzed	27	2.6	25.5	75	4.1
Uremia, Dialyzed	115	9.1	160	89	8.5
Dialysis Encephalopathy Syndrome	281	15	301	215	24.5

Assessments of aluminum in the body with the goal of monitoring potential pathological and neurological disorders should probably focus on the storage in the skeleton. Bone storage clearly correlates when aluminum exposure exceeds the excretion capabilities of the body. There are retention variations among individuals, so it may be impossible to make absolute quantitative estimates of exposure based on current bone burdens. Sampling of urine and blood do not demonstrate consistent correlations with the magnitude of exposure, likely due to wide variations in bioavailability and excretion rates among individuals, which are in turn affected by the chemical and physical characteristics of the aluminum compound. Such sampling can differentiate between non-exposed and exposed groups.

At typical, environmental exposures in healthy individuals, the human body does not express any negative impacts from aluminum. In situations where exposures greatly exceed environmental levels and/or where an individual is not healthy, it is possible that the body burden of aluminum could have several deleterious effects and become toxic. In fact, the first published report of aluminum toxicity was reported in 1897, in a study involving animals [23]. Unfortunately, much information concerning aluminum toxicity has come from direct experience in humans, both from those exposed occupationally as well as medical patients. The first description of aluminum toxication in humans in a scientific paper was in 1972 by Alfrey et al in patients undergoing hemodialysis [24]. The patients were experiencing chronic renal failure for

which they were receiving hemodialysis treatment. As hemodialysis treatments progressed, they developed encephalopathy that manifested as speech abnormalities, dysnomia, dyspraxia, tremors, myoclonus, asterixis, memory impairment, personality changes, and seizures. The patients all eventually passed away. It was subsequently determined that aluminum was in the water that was utilized to prepare the dialysate. Aluminum is often found in tap water as it is added during the water treatment process [25]. Additionally, patients undergoing dialysis often had aluminum compounds added to their diets as well, to act as phosphate binders and maintain healthy phosphorus levels. These patients were thus exposed to aluminum from the dialysis procedure as well as from medicine, all while having an impairment in their bodies' excretory capacity [26]. It should be noted that in the United States, the Food and Drug Administration now limits the amount of aluminum that can be in parenteral nutrition products to no more than 25 micrograms of aluminum per liter, so these types of exposures have been eliminated in this country [27, 28]. For patients undergoing dialysis, the levels of aluminum in the dialysate are maintained below 10 micrograms per liter, a level considered to be safe [5].

At toxic levels of exposure, aluminum has been demonstrated to cause osteomalacia, microcytic anemia, and neurologic deficits [29]. Osteomalacia is a softening of the bones and can result in an increase in the occurrence of fractures. It appears to occur at aluminum loads lower than that of neurological effects and usually only in renal patients [4]. Due to the limited number of aluminum measurements in bone, the exact skeletal concentration at which osteomalacia becomes a concern is not known, but a possible threshold is assumed to be above 5 mg of Al/g of dry bone [99]. In bone, aluminum deposits on the bone surfaces and has three possible effects: 1. It inhibits the formation and growth of hydroxyapatite; 2. It inhibits the proliferation of bone cells; and 3. It inhibits bone cell activity. These effects reduce bone mineralization, formation, and mass [30]. While aluminum does not directly displace calcium in bone, it may affect it indirectly by reducing the secretion of parathyroid hormone (PTH) from the parathyroid gland. PTH regulates the relationship between calcium and phosphorus and its reduction may interfere with calcium deposition [26].

A second aluminum effect demonstrated in humans was that of causing microcytic anemia. Microcytic anemia is a condition characterized by red blood cells that are small in volume. It was first noted by Touam in a group of patients undergoing dialysis. The anemia reversed after the dialysate was prepared with deionized water [11].

The final significant aluminum intoxication effect in humans are adverse neurological changes. The development of encephalopathy in patients undergoing hemodialysis was the first indication of toxicity issues [24]. Since then, neurotoxicity has been well documented in both humans and animals. Aluminum may be able to enter the brain intranasally, through the olfactory neurons in the nasal cavity. This route was proposed based off exposure in rabbits and has not been proven in humans [30]. Aluminum is known to be able cross the blood-brain barrier (BBB) and it can do so through at least a couple of different pathways. The aluminum cation (Al^{3+}) will form a complex with transferrin, which typically complexes with the iron cation (Fe^{3+}). Iron-transferrin is transported into the brain by the transferrin receptor and the aluminum-transferrin complex will also be transported by this receptor. In addition to the transferrin receptor, aluminum that has complexed with citrate, which is the second most common ligand in blood for aluminum, can cross the BBB mediated by monocarboxylic acid transporters (MCTs). MCTs normally transport monocarboxylates into the brain and when aluminum complexes with citrate, there is a free carboxylate, which allows transport [31]. The brain appears to have the ability to clear aluminum citrate through the MCT transport system. Clearance is a rather slow process, with an elimination half-life from the brain calculated to be seven years [12]. Once in the brain, aluminum can negatively affect several physiological functions. At high concentrations, aluminum can cause oxidative stress, which is an imbalance between oxidants and antioxidants that favors oxidants. This can interfere with redox signaling and control and lead to possible molecular damage. Aluminum also can bind to various membranes such as myelin and synaptosomal membranes, altering their function. In these situations, processes that rely on the membranes will be subsequently changed [32]. Additionally, it has been shown that aluminum can interfere with neurotransmitters in a variety of ways, although the specifics of the mechanisms in humans require more research [33]. Aluminum has also been proposed as a contributing factor for a multitude of disease states such as Alzheimer disease (AD), Parkinson disease (PD), amyotrophic lateral sclerosis (ALS), multiple sclerosis (MS), and autism [34]. The contribution of aluminum to AD development is based largely on aluminum being detected in amyloid plaques, neurofibrillary tangles (NFTs) and neuronal nuclei on patients diagnosed with AD [9]. Additionally, epidemiological studies seemed to show an association between aluminum in drinking water and an increase in AD prevalence [97, 98]. Currently, aluminum as a potential cause or confounding factor for

conditions such as AD remains controversial, as several other studies were not able to find elevated aluminum levels in AD patient brains or similar correlations with drinking water exposure [35, 36, 11]. It is worth pointing out that the prevalence of aluminum in the environment at levels much higher than those being measured in tissues such as the brain mean that sample contamination is a distinct possibility and can possibly explain the truly mixed results observed in studies examining similar targets. Aluminum's role as a neurotoxin is confidently documented but its contribution to disease states such as AD or ALS remains an open area of research.

A number of deleterious effects of aluminum in human populations have been identified in the past and an even larger number of potential effects remain to be proven or disproven. Aluminum as the primary cause of or at least a contributing factor to many of the potential disease states such as AD or ALS remains controversial, even after decades of study. The basis of why there remains so many equivocal results after so much study is largely due to difficulties in measuring aluminum in living humans. Oftentimes, studies have relied on surrogate measures of environmental aluminum such as concentrations in municipal drinking water or the air, with the assumption that there was direct correlation between those concentrations and intake by people in the area. These approaches suffer from significant confounding factors such as discrepancy with actual subject intakes and bioavailability of aluminum taken in. Improvement in study information can be gained by analyzing actual biomarkers of aluminum exposure. A variety of biomarkers have been investigated including blood, urine, feces, and bone. From the published human data, blood, urine, and feces do not appear to be strong indicators of the potentially dangerous accumulation of aluminum, as the concentrations of aluminum in those compartments change rapidly following an exposure. Several tissues have been demonstrated to accumulate aluminum, with the greatest percentage being stored in bone. Additionally, the long-term storage of aluminum in the body appears to be in the skeleton, making it an excellent biomarker of large or chronic exposures [15]. Unfortunately, taking bone tissue samples is a very invasive process and cannot be performed as either a screening or monitoring exam. This makes prolonged or large scale follow up of subjects all but impossible, thereby hindering the ability of researchers to definitively resolve the controversial associations with aluminum and health. The project described herein develops a simple way to monitor the most significant biomarker, in a manner that is not invasive to subjects. The method utilizes a setup that is

relatively mobile, allowing it to be brought to the locations of research subjects rather than they having to travel to a distant laboratory. The use of such a method increases up the possibility of monitoring aluminum in humans in an unequivocal manner.

1.3 Neutrons and Neutron Activation Analysis

1.3.1 Neutron Properties and Physics

The neutron is one of the fundamental particles of nature in the standard model of particle physics. Its potential existence was discussed by E. Rutherford as early as 1920 and its presence in the nucleus, along with the proton, was suggested by W. Heisenberg in 1932 [38, 39]. Neutrons were observed by W. Bothe and H. Becker when they bombarded several low atomic number elements with alpha particles from polonium. While they identified the resulting radiation as highly penetrating, they did not correctly identify it as being neutrons and instead assumed it was gamma rays. Following up on the experiments of W. Bothe and H. Becker, I. Curie and F. Joliot also generated neutrons by bombarding beryllium and boron with alpha particles from polonium. They also identified recoil protons being produced by neutron interactions, but they theorized they were being generated through gamma ray interactions. In 1932 J. Chadwick measured the recoil protons produced by the neutron interactions with low atomic number elements but he realized they could not be caused by gamma rays based on the conservation of energy. He concluded that a neutral particle, having a mass close to that of the proton, must be coming out of the low atomic number materials when bombarded with alpha particles and correctly identified the neutron for the first time [40]. Chadwick was recognized as the discoverer of the neutron with the awarding of the 1935 Nobel Prize in Physics.

The neutron is of the baryon family of particles, being composed of two down quarks and one up quark. It is electrically neutral and has a rest mass of 939.6 MeV/c^2. It, along with the proton, is present in the nuclei of nuclides, with the single exception being hydrogen-1. In the nucleus, the neutron is stable but outside of the nucleus it is unstable and decays with a mean lifetime of 14.76 minutes to a proton, electron, and electron antineutrino [41].

Neutrons are characterized by their kinetic energies. Various kinetic energy ranges have been assigned names and the common ones are listed in table 1.5 [42]. The number of classes and energy ranges are not completely standardized, and some variety can be found in various

authors. Kinetic energy is important however as neutron interactions are strongly influenced by it. It is important to note that as a neutral particle, the neutron cannot be accelerated in the same manner as a charged particle. Neutrons may be generated from reactions with high kinetic energies and therefore high velocities, but after generation, they can only be slowed down, that is, their kinetic energies can only be reduced and not increased.

Table 1.5 – Neutron classifications

Neutron Energy	Classification Name
< 0.025 eV	Cold
≈ 0.025 eV	Thermal
0.025 – 0.4 eV	Epithermal
0.4 – 0.6 eV	Cadmium
0.6 – 1 eV	Epicadmium
1 – 10 eV	Slow
10 – 300 eV	Resonance
300 eV – 1 MeV	Intermediate
1 – 20 MeV	Fast
> 20 MeV	Relativistic

Neutron interactions are strongly energy dependent. They are also highly dependent on the isotopic makeup of the material that they are interacting with. The probability of a particular reaction occurring between a neutron and a material is known as the microscopic cross section, symbolized by σ. The microscopic cross section can be described by considering a beam of neutrons with a flux of I (neutrons/cm^2/s) incident on a target of a certain isotope containing an amount of atoms N (atoms/cm^2) equal to the product of the target thickness, atomic density of the atoms in the target, and the area of the target. If a detector were set up at a particular angle to measure the neutrons emerging from the target per unit time such as demonstrated in figure 1.2, then the cross section would be equal to:

$$\sigma = \frac{R\left(\frac{neutrons}{second}\right)}{I\left(\frac{\frac{neutrons}{cm^2}}{second}\right) * N(atoms)} = cm^2/atom \qquad \text{(Equation 1)}$$

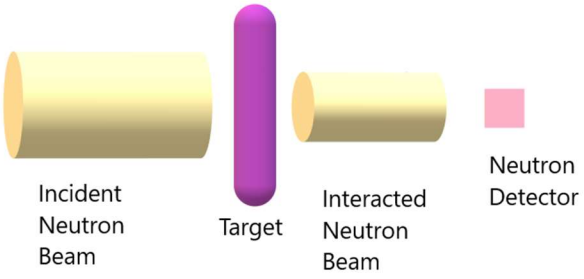

Figure 1.2 - Neutron cross section measurement setup

The cross section has units of area per atom and the special unit barn (b) has been designated as being equal to 1 x 10^{-24} cm^2. The cross section is essentially a reaction probability and is the effective cross-sectional area of the atom as experienced by the interacting neutron. This effective cross-sectional area may be markedly different from the actual physical cross section of the target atom and will vary depending on the kinetic energy of the neutron. Cross sections are specified for all types of nuclear reactions, including scattering, radiative capture, and charged particle emission. Generally, the cross section will be inversely proportional to the velocity of the neutron, across a wide range of low energies. This phenomenon is known as 1/v region in cross section data and is visualized in figure 1.3. At higher neutron kinetic energies, a series of dramatic increases may be seen in the cross section. These are resonances and they describe situations in which the likelihood that the incident neutron will be absorbed by the target nucleus is much increased due to the wavefunction of the incident neutron matching the wavefunction of the target nucleus, resulting in a high chance of penetration into the nucleus by the neutron. The result of the resonance absorption of a neutron is the formation of a compound nucleus with subsequent emission of the neutron, either elastically or inelastically, or the emission of a gamma ray [42].

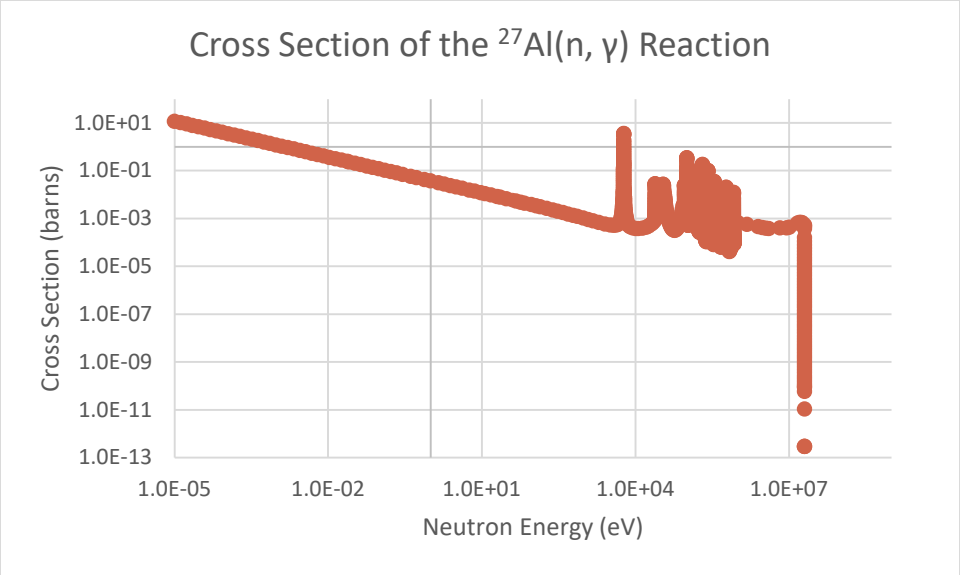

Figure 1.3 – Aluminum neutron activation cross section

When working with neutrons, whether it be shielding, detecting, or desiring their interaction with another material, usually effort is made to reduce their kinetic energy and thereby increase the probability that they will interact. The reduction in kinetic energy of a neutron is mediated through scattering interactions with atomic nuclei and the overall process is referred to as moderation. Scattering can either be elastic, where the nucleus remains in its ground state after the interaction, or inelastic, where the nucleus is left in an excited state. In describing the scattering of a neutron with a nucleus, the collision parameter, α, is given as:

$$\alpha = \left(\frac{A-1}{A+1}\right)^2 \qquad \text{(Equation 2)}$$

where A is the mass of the atom interacted with. The average fraction of neutron energy lost in an elastic isotropic scattering interaction is:

$$\frac{1-\alpha}{2} \qquad \text{(Equation 3)}$$

and the average fraction of neutron energy lost in an inelastic isotropic scattering interaction is:

$$\left(\frac{1-\alpha}{2}\right)\left(1-\left(\frac{A}{2}\right)\left(\frac{Q(A+1)}{AE}\right)\right) \qquad \text{(Equation 4)}$$

where E is kinetic energy of the neutron and Q is the difference in mass energy from the initiation to conclusion of the reaction [43]. The implication of the collision parameter is that for elastic scattering, energy loss by the neutron depends solely on the mass of the atom. The greatest possible energy loss in an interaction occurs with low mass number nuclei and the least amount of energy loss in an interaction occurs with high mass number nuclei. The average kinetic energy of an elastically scattered neutron can be determined by multiplying the collision parameter by the initial kinetic energy of the neutron [44]:

$$\Delta E = E_{initial} * \frac{1-\alpha}{2} \qquad \text{(Equation 5)}$$

The energy given up by the neutron in an interaction is not constant, due to it being dependent on the initial amount of energy carried into the reaction by the neutron. As interactions occur, the amount of kinetic energy of the neutron changes, resulting in a change in energy loss for subsequent interactions. To specify an average energy loss per interaction that is constant, the concept of lethargy was conceived. Lethargy is:

$$u = ln\left(\frac{E_{highe}}{E_{lower}}\right) \qquad \text{(Equation 6)}$$

where E_{higher} is the upper neutron energy and E_{lower} is the lower neutron energy. The power in the lethargy concept is that the average lethargy is not energy dependent, and it remains constant. The change in lethargy is then:

$$\xi = 1 - \frac{(A-1)^2}{2A} ln\left(\frac{A+1}{A-1}\right) \qquad \text{(Equation 7)}$$

This allows for the calculation of the average number of interactions it will take to reduce a neutron from the upper energy E_{higher} to the lower energy E_{lower} by:

$$n = \frac{1}{\xi} ln\left(\frac{E_{upper}}{E_{lower}}\right) \qquad \text{(Equation 8)}$$

As an example, six materials and their ability to moderate neutrons from 1 MeV down to 0.025 eV are presented in table 1.6 [39]. The lower mass materials are much more effective at reducing the energies of the neutrons. For this reason, moderating materials tend to be chosen such that they are primarily comprised of low mass number materials. Hydrogenous materials such as water, plastics, and paraffin are highly utilized to reduce the kinetic energies of neutrons.

Table 1.6 – Moderating properties of various materials

Material	A	α	ξ	n
Hydrogen	1	0	1	17.5
Light Water	1 and 16	N/A	0.920	19.0
Heavy Water	2 and 16	N/A	0.509	34.4
Carbon	12	0.716	0.158	110.8
Iron	56	0.931	0.035	495.9
^{238}U	238	0.983	0.0084	2083.9

1.3.2 Sources of Neutrons

There are a variety of sources of neutrons available to an investigator wishing to work with this fundamental particle. Each source has its own emission properties and wide variability is seen in availability. Sources include both deliberate and spontaneous fission neutrons, photoneutrons, mixtures of alpha emitting isotopes with certain nuclides, activation neutrons, and fusion neutrons [43].

Fission is the splitting apart of a nuclide and is typically a process only experienced with atoms having very heavy masses. It may be performed purposely, such as in a nuclear reactor or it may occur spontaneously in nature. When performed in a nuclear reactor, neutrons are absorbed by the heavy nuclide, forming a compound nucleus. The compound nucleus may decay

by fissioning, that is splitting apart into two unequal halves, known as fission fragments. Along with the splitting of the nucleus, between zero and eight neutrons are promptly emitted within a fraction of a second, depending on which fragments are created. The average number of prompt neutrons emitted in the fission reaction ultimately depends on the identity of the fissionable material. In a nuclear reactor, the emitted neutrons are utilized to maintain a constant amount of subsequent fission reactions, thereby creating a sustained controlled reaction. In addition to the prompt neutrons, there will be emission of delayed neutrons from the decay of some of the fission fragments. Delayed neutrons may be emitted seconds to minutes after the fission event that created the fragments they come from. The promptly emitted neutrons are produced with a spectrum of energies, with the greatest number peaking around 0.7 MeV and the average energy around 2 MeV [39]. The delayed neutrons make up a mere fraction of the fission neutrons and their average energies range from 0.2 to 0.4 MeV [44]. Utilizing neutrons produced in a nuclear reactor can be accomplished several different ways. One set of methods is to place a sample inside the reactor, near to the core, allowing exposure to the neutrons. The sample may be physically placed by remote handling tools in a pool reactor or it may be transported and retrieved via pneumatic delivery system, if the reactor is equipped. A secondary method of exposure is to place a void in the reactor shielding, which will allow neutrons to escape the core without absorption. The void is known as a beam port and a sample to be irradiated can be placed in the flux of neutrons exiting the reactor through it.

Fission can also occur spontaneously in certain very heavy nuclides, without the need to be exposed to neutrons. In spontaneous fission, the heavy nuclide splits into two fission fragments and emits typically two to four prompt neutrons. Delayed neutrons may be released from the decay of the fission fragments. A total of 127 different nuclides have been identified as being able to spontaneously fission [45]. Spontaneous fission is a competing decay process, usually with alpha particle emission. For the vast majority of the 127 nuclides that can spontaneous fission, it is an insignificant decay mode. Table 1.7, partially taken from [27], lists several nuclides that can undergo spontaneous fission, along with their half-lives and the number of alpha particle emissions per fission. Given the generally long half-lives and amounts of other decay modes, spontaneous fission is usually rare. A notable exception to this is californium-252, which has a half-life of 2.638 years and fissions in about 3% of decays. The length of its half-life and the relative abundance of spontaneous fission have made it a useful source of neutrons.

It produces 3.73 neutrons per fission on average, with an average neutron kinetic energy of 1-3 MeV [43, 42].

Table 1.7 – Decay properties of several heavy isotopes

Nuclide	Half-life (years)	Fission Probability per decay (%)	Alpha Particles per Fission
^{235}U	7.04×10^{8}	2.0×10^{-7}	5.0×10^{8}
^{239}Pu	2.41×10^{4}	4.4×10^{-10}	2.3×10^{11}
^{241}Am	433.6	4.1×10^{-10}	2.4×10^{11}
^{248}Cm	3.39×10^{5}	8.26	11
^{252}Cf	2.638	0.077	31
^{254}Fm	3.699×10^{-4}	0.053	1.9×10^{3}

Neutrons can also be generated from mixed sources that place an alpha emitting isotope in contact with a secondary nuclide such as beryllium, boron, or oxygen. These sources produce neutrons through an (α, n) reaction and were in fact the original sources that led to the discovery of the neutron. The most common nuclide in mixed sources is beryllium-9, which has a relatively loosely bound neutron in its nucleus. The neutrons are generated via the reaction:

$$^{9}_{4}Be + ^{4}_{2}\alpha \longrightarrow ^{12}_{6}C + ^{1}_{0}n \qquad \text{(Equation 9)}$$

Neutrons produced from mixed nuclide sources tend to have large amounts of energy and are emitted with a complicated energy spectrum. The number of neutrons produced is strongly dependent on the energy of the alpha particle. Some typical mixed nuclide sources, partially taken from [46] are listed in table 1.8.

Table 1.8 – Mixed nuclide neutron source characteristics

Source	Maximum Neutron Energy (MeV)	Average Neutron Energy (MeV)	Yield (neutrons x 10^6 / second per curie)
^{210}Po-Be	10.8	4.3	2.5
^{226}Ra-Be	13.2	3.6	15
^{210}Po-^{10}B	6.1	2.8	0.8
^{210}Po-^{19}F	2.8	1.4	0.1

As with the (α, n) reaction, neutrons can also be generated from the (γ, n) reaction. Neutrons produced in such reactions are known as photoneutrons as they are generated as a result of the absorption of a photon by an atom. Photoneutrons can be produced as a consequence of the operation of an electron accelerator, which generates high energy bremsstrahlung photons when the electrons interact with the target material. The energy of the generated photoneutrons depends on the mass number of the interacted material, the energy of the incident photon, the energy threshold of the reaction, and the angle between the incident photon and neutron emission [43]. In addition to incident photoneutron production, mixed nuclide sources can be made that combine a high energy gamma emitting radionuclide with a stable nuclide that readily emits a neutron upon interaction with the gamma ray. These sources generally utilize beryllium or deuterium as the stable nuclide and the reaction is as follows:

$$^{9}_{4}Be + ^{0}_{0}\gamma \longrightarrow ^{8}_{4}Be + ^{1}_{0}n \qquad \text{(Equation 10)}$$

Several (γ, n) mixed nuclide sources, taken from [43], are listed in table 1.9. An advantage of (γ, n) mixed nuclide sources is that the emitted neutrons are relatively monoenergetic. A significant disadvantage is that the gamma ray dose can be significant around these sources if not properly shielded, as the neutron yield is a very small fraction of the total high energy gamma rays produced by the decay of the radionuclide.

Table 1.9 – Gamma, neutron source characteristics

Source	Photon Energy (MeV)	Photons per Decay	Average Neutron Energy (MeV)	Neutron Yield (neutrons per $1x10^6$ decays/g at 1 cm)
^{24}Na + Be	2.754	1.0	0.967	3.5
^{88}Y + Be	1.836 2.734	0.993 0.006	0.151 0.949	2.7
^{124}Sb + Be	1.691 2.091	0.490 0.057	0.022 0.378	5.1
^{140}La + Be	2.522	0.034	0.761	0.08
^{226}Ra + Be	Many		0.68 max	0.8

The final source of neutrons is from accelerators, which accelerate charged particles and direct them into a target material in order to produce nuclear reactions. Neutrons may be the desired outcome of the nuclear reactions or they may be produced as a byproduct of them. A variety of different accelerators have been developed including electrostatic/constant-voltage and radiofrequency. The profile of the neutrons arising from each type of accelerator depends on their construction and operation. Electrostatic/constant-voltage accelerators include the Cockroft-Walton Accelerator and the Van de Graff Accelerator. The Cockroft-Walton Accelerator uses a pressure tank filled with an insulating gas to allow the generation of an accelerating voltage up to six million volts. The Van de Graff Accelerator utilizes an insulated belt that runs between the ground and high voltage terminals to build up charge. Voltages up to 15 million volts can be produced. A further development in the design of the Van de Graff Accelerator is the Tandem Van de Graff Accelerator, which accelerates negatively charged ions, then strips one or more electrons from the particle and finally accelerates the entity again. Tandem Van de Graff Accelerators can accelerate protons and deuterons up to 20 million volts [47]. Radiofrequency accelerators include the cyclotron, the linear accelerator (LINAC), the betatron, and synchrotron, and plasma neutron generators. The cyclotron works by accelerating a charged particle in a circular motion, starting near the center of the unit. A gap or gaps are placed in the cyclotron and as the accelerated particle reaches a gap, the polarity of the electric field accelerating the particle is reversed and the particle continues to be accelerated. As the kinetic energy of the particle increases, its velocity increases. The increase in velocity is matched by an increase in its path length as it travels in an outward circular motion. The increase in path length as velocity increases allows the reversing of the electric field to remain constant. Cyclotrons can accelerate particles to very high energies and are essentially limited by relativistic concerns, when the mass of the particles begins to significantly increase thereby affecting the ability of the acceleration to remain synchronized. The linear accelerator (LINAC) works by injecting charged particles into an evacuated chamber. The chamber contains several cylindrical electrodes, the length of which increase as the distance from the ion source increases. The ion moves down the length of the chamber, experiencing acceleration due to the switching of the polarity of the electric field. As the ion reaches the end of one electrode it feels the repulsion of the electric field. The polarity then switches so that it feels the attraction of the subsequent electrode. The attraction accelerates the ion, which increases in kinetic energy and

velocity. The increasing lengths of the electrodes compensate for the increased ion velocity, allowing the switching electric field polarity to remain synchronized with the acceleration. Betatrons and synchrotrons work by accelerating charged particles in closed loops using magnetic fields. Betatrons were developed to accelerate electrons while synchrotrons may accelerate electrons or other charged particles [48]. The final radiofrequency accelerator is the plasma neutron generator. These types of accelerators are used to purposely produce neutrons. They do so by using a radiofrequency ion plasma source to generate ions that are then accelerated into a target material, typically a metal hydride. Accelerated ions interact on the metal hydride and undergo a fusion reaction. The most common plasma neutron generators create neutrons via the deuterium-deuterium or deuterium-tritium reactions:

$$^{2}_{1}H + ^{2}_{1}d \rightarrow ^{3}_{2}He + ^{1}_{0}n \qquad \text{(Equation 11)}$$

$$^{3}_{1}H + ^{2}_{1}d \rightarrow ^{4}_{2}He + ^{1}_{0}n \qquad \text{(Equation 12)}$$

The number and energy distribution of neutrons generated by accelerators can vary greatly. Photoneutrons may be produced when high energy bremsstrahlung photons are generated from the acceleration of light particles, especially electrons. There will also be a wide variety of neutrons produced via nuclear reactions when accelerated particles strike accelerator target materials. The greater the energy the particles are accelerated to, the greater the number of potential nuclear reactions that are possible. In the deliberate production of neutrons using accelerators, several reactions are commonly used. Deliberately using a specific reaction allows for the production of neutrons that are relatively monoenergetic, in that the energies of the neutrons are constant in each reaction and well characterized. Commonly used reactions for deliberate neutron production, taken from [49] are listed in table 1.10.

Table 1.10 – Light ion neutron generating reaction characteristics

Reaction	Q Value (MeV)	Emitted Neutron Energy at Threshold Bombarding Energy (MeV)
$^{2}H(d, n)^{3}He$	3.266	2.448
$^{3}H(p, n)^{3}He$	-0.764	0.0639
$^{3}H(d, n)^{4}He$	17.586	14.064
$^{9}Be(\alpha, n)^{12}C$	5.708	5.266
$^{12}C(d, n)^{13}N$	-0.281	0.0034
$^{13}C(\alpha, n)^{16}O$	2.201	2.07
$^{7}Li(p, n)^{7}Be$	-1.646	0.0299

1.3.3 Neutron Activation Analysis

Neutron activation analysis (NAA) is a technique that can non-destructively identify the isotopic components of a material. It was initially developed in the 1930s based on the work of G. Hevesey and H. Levi. The technique became more widespread in the late 1950s with the availability of neutron generating accelerators [49]. NAA has seen an even greater distribution since then with the development of small, tabletop neutron generators that are able to produce neutron fluxes up to 1 x 10^{11} neutrons/second [50].

The basis of the NAA technique is to expose an analyte to a source of neutrons. If energetically possible, a portion of the atoms within the analyte will capture neutrons and become activated. The activity of the radionuclides produced will be equivalent to:

$$Activity = N\sigma\phi\left[1 - e^{-\lambda t_i}\right] \quad \text{(Equation 13)}$$

where N is the number of atoms of a particular isotope in the sample, σ is the cross section for a neutron capture reaction involving the isotope, φ is the neutron flux, λ is the physical decay constant of the activated isotope, and t is the irradiation time. The term $\left[1 - e^{-\lambda t_i}\right]$ accounts for the fact that during the irradiation period, the activated atoms are immediately subject to physical

decay. As more atoms are being activated, a portion of the already produced activity is physically decaying and will not be available for subsequent analysis.

Following activation, the photon radiations coming from the decay of the activated atoms are analyzed with a radiation detector having spectroscopic capabilities, typically a scintillator such as sodium iodide or a semiconductor such as high purity germanium (HPGe). Since specific photon energies are particular to given nuclear decays, their detection can be used for identification purposes. The activity of a given photon x from the decay of the activated atoms is equivalent to:

$$Activity_x = F_x N\sigma\phi\left[1 - e^{-\lambda t_i}\right]\left[e^{-\lambda t_t}\right] \qquad \text{(Equation 14)}$$

where the variables are the same as in equation 13 with the addition of F_x, which is the fraction of decays that result in a particular photon under analysis. If 100% of decays result in the photon being emitted, then the term F_x is superfluous, but this is an uncommon scenario among the known radioisotopes. The term $\left[e^{-\lambda t_t}\right]$ accounts for the decay of the radioisotope between the conclusion of the activation irradiation and the start of the radiation detection.

Ultimately, the number of counts detected at a certain energy is equivalent to:

$$Counts_x = \frac{F_x E_x N\sigma\phi\left[1-e^{-\lambda t_i}\right]\left[e^{-\lambda t_t}\right]\left[1-e^{-\lambda t_c}\right]}{\lambda} \qquad \text{(Equation 15)}$$

where the variables are the same as in equation 14 with the addition of E_x, which is the efficiency of the detection system for the particular photon under analysis. The term $\left[1 - e^{-\lambda t_c}\right]$ accounts for the integration of counts during the measurement process. The measurement period usually is not long enough to allow the complete decay of the activated atoms and this term integrates for the fraction of total decay taken up by the measurement process.

NAA can be performed to identify isotopic composition of a sample or to quantify the amount of an isotope in a sample. Identification studies are usually straightforward as given photons are characteristic of particular radioactive decays. By comparing the energies of the detected photons to photon databases, identification can be made. The confidence of the identification does depend on the energy resolution of the detection system as well as the

detected photon energy. At lower energies, the energy resolution of imaging system may not allow the accurate separation of closely spaced photopeaks. Additionally, there are several radioisotopes that emit identical or nearly identical gamma rays. If potentially interfering isotopes are present in a sample, it may be impossible to determine the origin of a detected photon. Table 1.11, taken from [51] gives a small portion of potential interferences commonly encountered as an example of the issue.

Table 1.11 – Several potential gamma ray spectroscopy interfering nuclides

Nuclide Under Study	Photon Energy (keV)	Interfering Nuclide	Interference Photon Energy (keV)
^{46}Sc	1120.5	^{182}Ta	1121.3
^{51}Cr	320.1	^{147}Nd	319.4
^{64}Cu	511	^{24}Na	511
^{64}Cu	511	^{65}Zn	511
^{75}Se	136.0	^{181}Hf	136.5
^{113}Sn	391.7	^{160}Tb	392.5
^{203}Hg	279.1	^{75}Se	279.5

NAA studies attempting quantification can do so either absolutely or relatively. Absolute quantification involves measuring or estimating the efficiency of the detection system for a particular radiation as well as the neutron flux and combining that with known values for the reaction cross section, irradiation, transfer, and count times, decay constant of the radionuclide under study, and branching ratio for the detected radiation to arrive at the number of counts from the nuclide under study. The counts in the photopeak from the radionuclide are then used to determine the mass of the analyte in the sample by comparison with a calibration curve for the system. The calibration curve, like the sample one in figure 1.4, gives the response of the detector system to known amounts of the radionuclide.

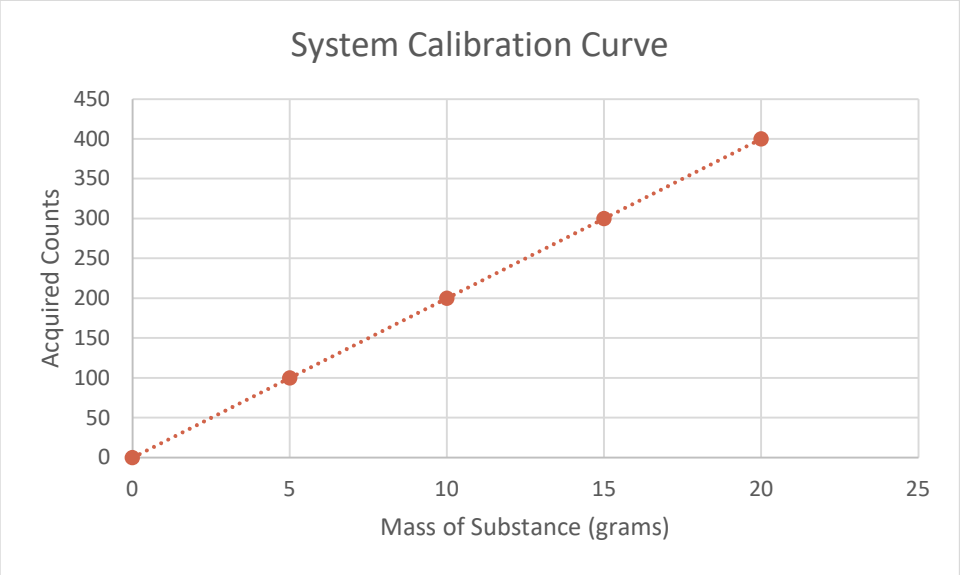

Figure 1.4 – Sample detection system calibration curve

There are several potential difficulties with absolute quantification with the most significant being an accurate estimate of detector efficiency, an accurate assessment of the neutron flux used for the irradiation, and the correct application of neutron cross section. Detector efficiency is specific for a given photon energy and counting geometry. Measurement of detector efficiency may be made with the same or very similar photon energies as those emitted by the analyte, but it is unlikely that the geometry of the efficiency source and the analyte will be equivalent. Any changes to the geometry will impact the efficiency. In terms of neutron flux, the amount of activation is linearly proportional to it. Any alterations to the neutron flux during the irradiation period will have a linear effect on activation. Usually, neutron fluxes are estimated and assumed to be constant during the irradiation. However, the actual flux impinging on the sample may deviate from the assumption and if using a neutron generator, may not be constant during the complete irradiation. It is possible to measure the neutron flux during irradiation by utilizing irradiation foils. This is an additional step in the measurement process and activation foils are energy dependent. Assessment of the various energy components of the neutron spectrum is a very involved process. Finally, there are potential errors associated with the neutron capture cross section used in the calculations. Cross sections are strongly energy dependent and the analyte will ultimately be exposed to a variety of neutron energies as the neutrons pass through moderator, reflector, and surrounding materials.

The utilization of a single cross section assumes all the neutrons possess the same energy and this will inject a certain amount of error into the calculation, the magnitude of which depends on the distribution of the neutron energies as well as the nuclide under analysis.

A second technique for quantification is the use of relative calibration, also known as the direct comparator method. In direct comparator, the analyte undergoes irradiation along with a calibrator that has a known quantity of the same exact nuclide that is being analyzed. The analyte and the calibrator are then counted separately with the same detector, under the exact same measurement conditions. Analyzing the net peak counts in the photopeak for the nuclide under study allows the direct determination of the unknown mass in the analyte by:

$$mass_{unknown} = mass_{calibrator} * \frac{Net\ Counts_{unknown}}{Net\ Counts_{calibrator}} \quad \text{(Equation 16)}$$

The power of this method is that variables such as neutron flux, cross section, and efficiency are largely cancelled out. There could still be significant error introduced into the measurement if the geometry of the calibrator deviates from that of the analyte as this would result in efficiency differences. Additionally, if the activities of the unknown analyte and the calibrator were significantly different, there could be dead time effects in the detection system that would result in efficiency differences.

1.3.4 In Vivo Neutron Activation Analysis

NAA has been performed on a wide variety of samples and for the analysis of a wide variety of isotopes. Usually, it is performed on non-living samples such as for contraband detection, mineral composition determination, or non-destructive testing of sensitive materials. It is possible however to perform NAA on living people or animals, a concept known as in vivo neutron activation analysis. A variety of elements have been analyzed in vivo over the years including calcium, nitrogen, carbon, oxygen, potassium, chlorine, sodium, phosphorus, hydrogen, manganese, gadolinium, and aluminum [50, 52, 53, 54, 55, 56].

The most significant advantage of in vivo NAA is that it is a non-invasive technique for determining the presence or quantity of a substance in the body. Alternative sampling

techniques typically require the collection of tissues or fluids from the body, depending on the chemical substance under evaluation. If a substance is readily excreted, then collection may be simplified to acquiring the bodily fluid the substance excretes in and analyzing it. If the substance is not readily excreted, then collection of a tissue through biopsy is required. Depending on the tissue to be sampled, biopsy can be an incredibly invasive procedure, requiring anesthetization of the patient and carrying additional risks of infection from the collection procedure itself. For substances that may be resident in critical organs such as the heart and brain, biopsies would only occur once a tissue is suspected of being abnormal. They would never be performed as part of a monitoring program. In vivo NAA does not carry the risk of the invasiveness of performing a biopsy. It can be performed readily on a wide range of people and animals without the need for anesthesia or surgery. Because there is no destruction or removal of tissue, it can potentially be utilized as a monitoring technique for a wide range of elements and substances, that is sequential samples can be taken over a period of time. Use as a monitoring technique can be conducted for a number of reasons including to identify events in which an individual has suffered an acute exposure to a substance or to monitor the buildup of a substance from a chronic exposure to ensure a safe body burden level is not exceeded.

There are some limitations to performance of in vivo NAA. As with any procedure performed on living individuals, there are potential risks. The main risk from NAA is that it requires the exposure to radiation. At very high dose levels, radiation has been proven to generate a variety of tissue reactions. It would not be expected that NAA ever be performed at such dose levels as there is no justification in getting information at the cost of knowingly imparting some level of harm to the individual. Also at high dose levels, radiation has been demonstrated to result in an increase in several cancer rates. At lower radiation dose levels, the increases in cancer rates have not been demonstrated above background cancer rates. It may be that at low levels, radiation has no effect on cancer induction or that its effect is so small as to not significantly increase the overall rate. Nevertheless, the linear no-threshold theory is applied to cancer induction by radiation, whereby a linear response from high radiation doses is extrapolated down to the point of no radiation dose. This relationship assumes that all radiation dose carries with it some quantity of stochastic risk to the human and that there is no threshold below which there is assumed no risk. Exposures to radiation from in vivo NAA would fall within the extrapolated area of the linear, no-threshold theory. That is, while the radiation doses

would not be large enough to experience a significant increase in cancer rates, they would not be assumed to be zero risk. Individuals undergoing in vivo NAA would be exposed to a theoretically increased risk of stochastic detriment.

In vivo NAA has an additional, more physical limitation in that it is not able to detect all isotopes at biologically significant levels. Detection is a function of the flux of neutrons available, the cross section of the isotope under analysis, and the number of atoms in the substance to the irradiated. Many isotopes do not have neutron capture cross sections large enough to allow for the production of a significant amount of activation. Other isotopes are not present in the human body, either naturally or unnaturally, in quantities that exceed the capabilities of the detection system. Some isotopes may be present in large amounts but the radiations they emit upon activation are not of the kind and frequency that allows ready detection. Finally, the half-life of the activated atoms must be long enough to allow transfer from the irradiation to the counting portions of the system but not so long that very few decays occur during the measurement period.

1.3.5 Detection Limit

A key point of this work is to determine the detection limit of our laboratory's NAA system for aluminum. It is important to define what is meant by detection limit, as a wide range of formulas and values have been traditionally used. Concepts of detection limit have been loosely applied for counting radioactivity, regardless of the types or quantity of signal. From a strictly technical sense, applicability of statistical models and ultimately their appropriate use, depends on how much signal is being detected and what type of interpretation we are trying to make of the signal. In this project, we are trying to determine the minimum amount of aluminum-28 that can be detected. Crucial to our detection limit description is the fact that we are detecting the 1.779 MeV gamma ray resulting from the radioactive decay of aluminum-28. This gamma ray is of high enough energy that there are close to zero background counts that fall within its energy window in a gamma ray spectrum. Any count detected in the energy window can be assumed to arise from the decay of aluminum-28, meaning we can detect down to a level of an individual atom. Traditionally, detection limits have been specified based on the Gaussian distribution, which is not directly applicable to limited counts over zero background.

1.3.5.1 Statistical Distribution Models

There are many statistical distributions that have been described mathematically, but three are typically applied to data arising from the detection of radiation: Binomial, Poisson, and Gaussian/Normal. Which distribution is the most appropriate to utilize depends ultimately on the quantity of data that has been collected.

The Binomial distribution applies to an event that has one of two possible outcomes. It is defined as:

$$P(x) = \frac{n!}{(n-x)!x!} p^x (1-p)^{n-x} \qquad \text{(Equation 17)}$$

where P(x) is the probability of x number of successes, p is the probability of an individual success, and n is the number of trials. We can consider the detection of radiation a binary process in that we either detect a decaying atom or we fail to detect a decaying atom. The number of trials is the number of atoms being investigated and the probability of individual success is the detection of radiation emitted from an atom that has decayed. As we generally are investigating a large number of atoms, it is readily apparent that the mathematics of the Binomial distribution can quickly become difficult to work with given the number of exponents and factorials in the equation.

Under conditions where the probability of an individual success is small, such as we have with detecting radiation, the Binomial distribution is approximated by the Poisson distribution. The Poisson distribution is given by:

$$P(x) = \frac{(pn)^x e^{-pn}}{x!} \qquad \text{(Equation 18)}$$

where P(x) is the probability of x number of successes, p is the probability of an individual success, and n is the number of trials. It is evident from equation 18 that the Poisson distribution is mathematically simpler to work with compared to the Binomial distribution, as there is only one factorial term.

The Gaussian/Normal distribution is the third one that may be applied to radiation detection measurements. The Gaussian distribution is given by:

$$P(x) = \frac{1}{\sqrt{2\pi\bar{x}}} e^{\left(\frac{-(x-\bar{x})^2}{2\bar{x}}\right)} \qquad \text{(Equation 19)}$$

where P(x) is the probability of x number of successes and $\bar{x}$ is the mean count value, which is equal to the individual probability of success times the number of successes [57]. Mathematically, the Gaussian is much simpler for large values of counts, relative to the Binomial and Poisson distributions. Use of the Gaussian distribution is valid when the mean count value is large and the greater the mean count value, the closer the values determined by the Gaussian and Poisson distributions will be. Both the Poisson and Binomial distributions are discrete and asymmetric, while the Gaussian specifies continuous values and is perfectly symmetric about the mean. When describing larger numbers of detected counts, the Poisson and Binomial distributions approach more symmetric shapes and can be better approximated by the Gaussian distribution [58]. Typically, as a rule of thumb, the Gaussian approximation is valid when x is equal to or greater than 20 [59]. This rule of thumb makes an assumption about the desired error level with the detection process. It was determined by Justus that as the level of accepted error is reduced, the number of counts needed for convergence between the Gaussian and Poisson distributions increases [60]. When the number of counts is expected to be less than 20, or when very small error levels are desired, the Gaussian may not provide a good approximation and should not be used. In these situations, such as we have with extreme, low-level counting, the Poisson distribution should be employed.

1.3.5.2 Detection Limit (DL) Expressions and the DL for IVNAA Al Quantification

There have been a variety of critical limit, detection limit, and minimum detectable activity expressions made over the past several decades. Most are based in part on the work published by Currie in 1968. In that paper, the critical level L_C is defined as the point at which a result indicates detection has been made. The critical level is set by the acceptable amount of α (also known as Type I or false positive) error and the standard deviation of the net signal, σ_o, when the sample mean is equal to zero. The critical level is given as:

$$L_C = k_\alpha \sigma_o \qquad \text{(Equation 20)}$$

If the magnitude of signal under analysis were exactly equal to the critical level, it would correctly be detected one-half of the time. Setting α equal to 0.05 would result in the background being incorrectly identified as signal 5% of the time when no signal was actually present. Based on the critical level, an acceptable amount of β (also known as Type II or false negative) error, and the standard deviation, σ_D, of the distribution when the net signal has no systematic error, the detection limit L_D can be determined. The detection limit was expressed as:

$$L_D = L_C + k_\beta \sigma_D \qquad \text{(Equation 21)}$$

The detection limit is the smallest amount of signal that a given analytical procedure requires in order to give a reliable detection of what is being analyzed. Currie based his work on hypothesis testing and the Gaussian distribution. Examples in his work were taken from situations in which the Gaussian distribution applied, that is, situations where the number of counts detected were large enough that the Gaussian distribution matched the results that would be determined from the Poisson distribution. For situations involving paired observations, such as a sample count and a background count, Currie gave the critical level and detection limit expressions as:

$$L_C = 2.33\sqrt{\mu_B} \qquad \text{(Equation 22)}$$

$$L_D = 2.71 + 4.65\sqrt{\mu_B} \qquad \text{(Equation 23)}$$

where μ_B is the blank or background mean value. This expression of detection limit results in a signal being correctly identified 95% of the time and the background being identified incorrectly as true signal 5% of the time. These expressions not only assumed a Gaussian distribution applied but they also assumed equal levels of 0.05 for both α and β errors [61]. Nearly all expressions of the limit of detection are based on the work of Currie. Frequently, the applicability of his assumptions of Normality or error levels to individual radiation detection tasks are not critically analyzed to determine their validity.

For extreme low-level count scenarios, Normality cannot be assumed and the Currie expression of the detection limit may not be appropriate. A variety of alternative expressions of the detection limit have been proposed over the years, using a number of different distributions

as well as Bayesian techniques [62, 63, 64, 65, 66, 67, 68, 69, 70]. Many of the attempts to specify detection limits with a distribution other than a Gaussian still relied on error levels taken from the Gaussian distribution – a hybrid solution that is not completely valid but is more conservative.

A Poisson-based detection limit was developed by Alvarez that better estimates probabilities involving few total counts [66]. He derives the critical level as:

$$L_c = \frac{k^2+\sqrt{k^2+8k^2\mu_B}}{2} \quad \text{(Equation 24)}$$

where k is the probability level of error and μ_B is the mean blank count. He further derives the detection limit as:

$$L_D = \frac{4k^2+\sqrt{16\ ^4+32k^2\mu_B}}{2} \quad \text{(Equation 25)}$$

Alvarez makes a comparison between the critical levels and detection limits derived by himself and Currie, a portion of which is stated in table 1.12.

Table 1.12 – Comparison of Currie and Alvarez critical and detection limits

Mean Background	L_C Currie	L_C Alvarez	L_D Currie	L_D Alvarez
1	2.3	4.0	7.3	12.5
2	3.3	4.9	9.3	13.9
3	4.0	5.6	10.7	15.1
5	5.2	6.7	13.1	17.1
10	7.3	8.8	17.3	21.1
20	10.3	11.8	23.4	26.9
30	12.7	14.2	28.0	31.5
50	16.4	17.9	35.4	38.8
100	23.1	24.7	49.0	52.3
200	32.7	34.3	68.1	71.4

As discernable from table 1.12, at low numbers of counts, the critical level and detection limit determined by Alvarez are conservative relative to Currie. As Currie's equations are based on an assumption of Normality, which does not hold at few counts, employing a more

conservative approach ensures fewer false positive detections. As the number of detected counts increases and Normality is approached by the data, the two methods converge and the use of Currie's formulas would be appropriate.

1.4 Monte Carlo Simulation Technique

Monte Carlo (MC) simulation techniques were first developed in the 1940s at Los Alamos National Laboratory (LANL) to solve neutron transport problems in the development of atomic weapons. The method was invented by Stanislaw Ulam in 1946, who discussed it with John von Neumann. Von Neumann recognized that the technique could be applied to electromechanical computers which were just beginning to be developed. Von Neumann developed the first Monte Carlo program with the support of Robert Richtmyer. The initial calculations were completed on the ENIAC computer in 1948. Further development was extended on the MANIAC computer by Nicholas Metropolis, who along with Ulam published the first paper in which the term Monte Carlo appeared in 1949 [71]. Over the past several decades, Monte Carlo simulation techniques have been extended to a variety of problems in business, engineering, and science, not just those involving radiation transport.

The technique uses a mathematical model to simulate physical systems. Interactions between objects are randomly sampled repeatedly to develop the probability of a particular outcome. The result is a prediction about the outcome of a process that is stochastic, that is, a process that has a random component [72].

Many Monte Carlo simulation codes have been developed over the years, including those that simulate radiation transport as well as those that simulate phenomenon other than radiation transport. The original Monte Carlo code developed by Ulam and von Neumann has continued to be developed, extended, and improved and is now known as Monte Carlo N-Particle (MCNP). A wide variety of other radiation transport Monte Carlo codes have been developed by research groups around the world. Some of the more widely utilized codes include FLUKA, GEANT4, PENELOPE, and TRIPOLI-4.

1.4.1 MCNP6

The work in this project utilized MCNP6. MCNP6 is the merging of MCNP5, which simulates the transportation of neutrons, photons, and electrons, with MCNPX, which simulates the transportation of 33 other particle types. There are additional features present in both codes and all were combined into MCNP6, along with features that were not previously available such as a high energy physics model and the ability to model magnetic fields [73]. MCNP6 is a general-purpose Monte Carlo radiation transport code that can track a large variety of particles over a wide range of energies [74]. The code can track neutrons, photons, electrons, and deuterons among other particles over the complete range of energies encountered in this project.

Initial simulation work on this project was performed utilizing both MCNPX, release 2.7.0 and MCNP5. Following the release of MCNP6, version 6.1, simulation work was transitioned to it. Eventually MCNP6, version 6.2 was released and utilized for all simulations. Previous simulations performed on versions X, 5, and 6.1 were all executed on version 6.2 to ensure complete and up to date results.

1.5 Research Goals

The goals of this project are threefold. First, to develop a simulation model of a neutron activation analysis system. Simulation allows the optimization and assessment of the system without its physical operation. Operation of the system requires dedication of resources and results in the production of radiation. The development of an accurate simulation means that the system can be physically operated only when actual activation analysis measurements are to be conducted.

A second goal is the determination of detection limit for Al quantification using the DD neutron generator neutron activation system. The uniqueness in the system lies in the fact that it is a tabletop neutron generator, able to be transported out of a centralized laboratory setting. The system can be moved closer to locations where activation is desired to be conducted, rather than the samples being transported to a laboratory.

The final goal is to determine the capability of the tabletop neutron activation system to measure aluminum in vivo in humans. Aluminum has no endogenous function in humans and at

high concentrations, it can cause a variety of biological complications. If the system is determined to have a detection limit below a level of in vivo aluminum that causes biological effects, then it could theoretically be utilized as a non-invasive screening or monitoring tool. It could be used to identify individuals in need of having their aluminum exposures limited or their body burdens therapeutically treated.

1.6 Significance

The significance of this work is primarily two-fold. First, is the presentation of a complete description utilizing Monte Carlo techniques of an NAA system used to analyze aluminum. The evaluation includes not only the activation portion of the system, whereby the sample is activated by neutrons produced by a tabletop neutron generator, but also the detection of the resultant decay radiation arising from the activated atoms. Simulation results are compared to experimental values to evaluate accuracy. Simulation techniques developed herein can be extended to other nuclides analyzed with the system. This will allow the determination and setting of valid experimental parameters without the need to expose people to radiation until data is to be collected.

The second significant aspect of this work is that it describes the detection capabilities of an NAA system utilizing a tabletop DD neutron generator as a neutron source and a HPGe detector for the evaluation of aluminum. The evaluation of aluminum via NAA has been reported by other groups utilizing neutron sources other than a tabletop DD neutron generator or with scintillation detectors. Detection capabilities depend strongly on the neutron source as well as the detector(s). This is a unique report of the detection capability for aluminum of a tabletop DD neutron generator being used in conjunction with a HPGe detector.

1.7 Dissertation Structure

This dissertation is structured such that it begins with an introduction to and background information on the element aluminum and a description of neutron activation as well as the analysis of the phenomenon. Finally, there is a discussion of Monte Carlo simulation techniques.

Following the introductory material, chapter two describes the simulation of the tabletop neutron generator systems. The first system our laboratory possessed was an Adelphi DD-108M.

Initial simulations of the unit were performed. Eventually, the laboratory came into possession of a DD-109M neutron generator, which was also simulated in MCNP. Development and enhancement of the MCNP simulation shifted completely to the DD-109M, including a more accurate method to specify the neutron source within the generator.

Chapter three describes the development of the MCNP simulation of the high purity germanium detector used by our NAA system. The detector was simulated and tallies developed that allow the estimation of the spectra generated by the system. The generated spectra can be used for a variety of purposes including estimation of the system sensitivity and detection limit.

Chapter four evaluates NAA data that was acquired with the DD-108M neutron generator for a purpose other than analyzing aluminum. The acquired data is assessed to determine if aluminum can be detected in the experimental data, even though it was not optimized for aluminum detection. The experimental parameters are analyzed with MCNP simulation to estimate the detection limit for aluminum.

Chapter five is a summarization of all the results and their implications. It draws conclusions on the work, including highlighting areas for future improvement and development.

CHAPTER 2. MCNP SIMULATION OF NEUTRON GENERATOR SYSTEMS

2.1 Introduction

Modelling in MCNP was performed to investigate the design of the experimental setup with the generator. Neutrons emerging from the DD reaction have approximately 2.45 MeV of kinetic energy and at these energies, absorption by target aluminum atoms is not maximized. It is necessary to reduce the neutron energies down to thermal levels in order to increase the probability of absorption and thereby activation of the aluminum, a process known as moderation. Materials that are used to reduce the neutron kinetic energies are known as moderators. Additionally, most neutrons are emitted at angles not directed towards the sample under investigation, or they pass through the sample, unreacted. The efficiency of the activation process can be increased if some of these unreacted neutrons are directed back towards the sample. Materials used to direct the neutrons back towards the sample being analyzed are known as reflectors [75]. Neutron reaction rates are complicated by the fact that they are highly dependent on the energies of the neutrons, which are constantly changing as they pass through materials and undergo interactions. MCNP is ideally suited to performing these calculations as it tracks neutron energies as they interact with materials and can be used to determine the types and quantities of reactions. To determine the optimal type and quantity of moderator and reflector, the first step was an accurate description of the DD-108M generator in MCNP.

2.2 Materials and Methods

Initial work on this project began with an Adelphi Technology Inc. (Redwood City, CA) DD-108M neutron generator. The generator utilizes the DD reaction, which results in the production of 2.45 MeV neutrons in the zero-degree direction. A neutron yield of up to 1 x 10^9 neutrons/second can be produced by the system [76].

The DD-108M generator was modelled in MCNPX, Version 2.7.0, a general-purpose Monte Carlo code for radiation transport developed and maintained by Los Alamos National Laboratory [77]. A complete description of the input for the DD-108M generator is given in Appendix A, updated to MCNP6.

2.2.1 DD-108M Neutron Generator System

A confidential and not reproduced in this document computer-aided design (CAD) drawing of the generator head was received from the manufacturer. The CAD drawing allowed for the determination of the sizes and relative positions of components within the generator. Based on these measurements, the generator head was modelled as an aluminum cylinder, with the inside consisting of air under a vacuum. Deuterons are accelerated in the generator to a V-shaped target that is composed of copper with a thin layer of titanium. The angle of the sides of the target V was measured to be 16 degrees. The target is shown in figure 2.1.

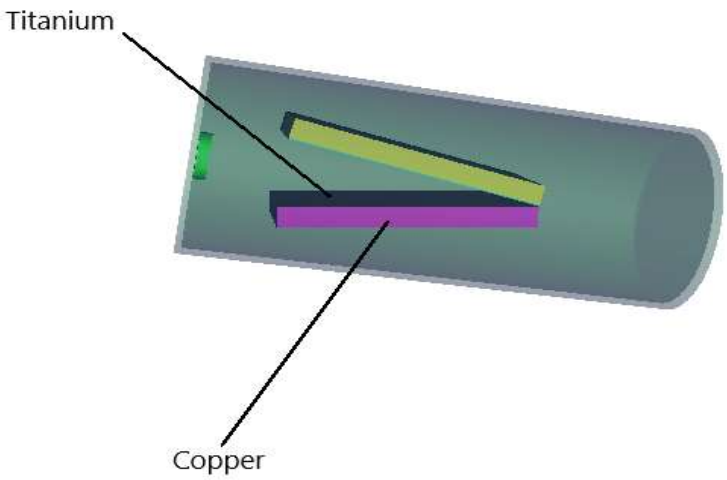

Figure 2.1 – MCNP simulation of generator head

Deuterons interact with the titanium of the target, forming titanium hydrate [78]. Subsequent deuterons strike the titanium hydrate and cause the production of 2.45 MeV neutrons. Detailed information as to exactly where on the target or how large an area is involved in neutron production was not known. The source was modelled as a circular plane of neutrons with a radius of 2-cm, directed towards the vertex of the titanium target V.

Optimization of the moderator and reflector was performed by adding a sample of aluminum to the MCNP input and tallying the amount of activated aluminum-28 produced. An F4 tally was employed to determine the amount of created Al-28. F4 tallies give flux averaged over a cell in units of neutrons/cm^2. The tally can be modified to yield the number of activated

atoms using the tally multiplier, FM, and segment divisor, SD, cards. The tally multiplier card takes the form:

FM# c m i

where # specifies the tally number, c is a multiplicative constant, m is the material number of the sample under consideration, and i is the evaluated nuclear data file (ENDF) number for the reaction of interest. The determination of the multiplicative constant requires the inclusion of the mass and density of the material under analysis. For example, if 1.0 gram of aluminum were used as a sample, the multiplicative constant would be:

$$c = \frac{6.02204344692 \quad {}^{23}atoms}{mol} * \frac{mol}{26.981538\ g} * \frac{1x10^{-24}cm^2}{barn} * 1.0\ g \qquad \text{(Equation 26)}$$

$$= \frac{0.022319126\ atoms * cm^2}{barn}$$

where 6.0220434469282x10^{23} atoms/mol is Avogadro's constant and 26.981538 g/mol is the molar mass of aluminum. The material number is specified as the same as what is listed in the input for aluminum, 208 in the case of the DD-108M MCNP simulation. Material numbers are the designation of the input file creator. The specification of the reaction number, i, is taken from the standard list of ENDF reactions. As we are interested in neutron capture, the reaction 102, denoting the (n, γ), was chosen.

To have the tally measure all the aluminum-28 atoms activated in the cell containing the natural aluminum, it is necessary to also specify a segment divisor card. The segment divisor card takes the form:

sd# 1

where # is the tally number and the number 1 directs the tally to integrate over the complete cell.

Setting up a simple activation tally and quantifying the amounts of activated atoms allowed the optimization of both reflector and moderator. For example, in determining the optimal thickness of moderator between the generator and the irradiated sample, a variety of moderator

thicknesses were simulated. The results are given in table 2.1 and demonstrate that the optimal thickness to utilize would be 6.0 centimeters, as activation peaks at that amount. Increasing or decreasing the thickness away from the optimal value would result in a reduction in the amount of activation.

Table 2.1 – Activation at varying moderator dimensions

Moderator Thickness (cm)	Tally Result (Al-28 atoms/source particle)
0.0	1.82×10^{-8}
1.0	5.48×10^{-8}
2.0	1.87×10^{-7}
3.0	3.66×10^{-7}
4.0	5.67×10^{-7}
5.0	7.14×10^{-7}
6.0	7.78×10^{-7}
7.0	7.28×10^{-7}
8.0	6.78×10^{-7}

Additionally, the selection of moderator and reflector material could be evaluated using the simple activation tally. When trying to moderate or reflect neutrons, one tends to focus on low atomic number materials, such as hydrogen or compounds that contain significant amounts of hydrogen, such as water, plastic, or paraffin. A variety of materials were investigated via simulation, simply by altering the material identification of the materials contained in the moderator/reflector cells specified in MNCP as well as those identified on the tally multiplier. Sample results are given in table 2.2 for one reflector cell that was simulated with three different materials.

Table 2.2 – Activation tally results with different moderators

Material	Tally Result (Al-28 atoms/source particle)
Graphite	1.21×10^{-7}
Polyethylene	1.27×10^{-7}
Water (light)	1.25×10^{-7}

From the results, which only represent one reflector cell, it is apparent there is not a large variation in the materials available for use. Ultimately, polyethylene was selected as the material to be employed as both moderator and reflector due to its ease-of-use relative to graphite and water.

The method for moderator optimization was demonstrated. In practice however, as multiple projects and multiple types of materials were to be analyzed by the neutron generator, it would not be practical to completely alter the moderator and reflector beyond small changes. Eventually a machined set of 47 polyethylene moderator/reflector blocks were purchased and placed around the generator. The blocks were carefully modelled and added to the MNCP input according to their machined size. The blocks fit together and included an irradiation cavity where samples could be inserted. Figure 2.2 shows the machine drawings of the generator with moderator/reflector in place and figure 2.3 shows an image of the MCNP input, as generated by Visual Editor version X_25.

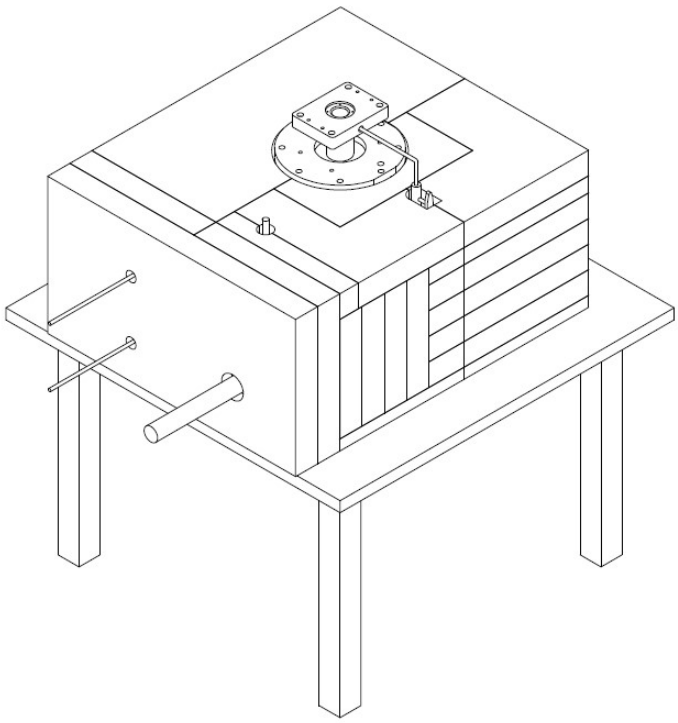

Figure 2.2 – CAD model of DD-108M moderator

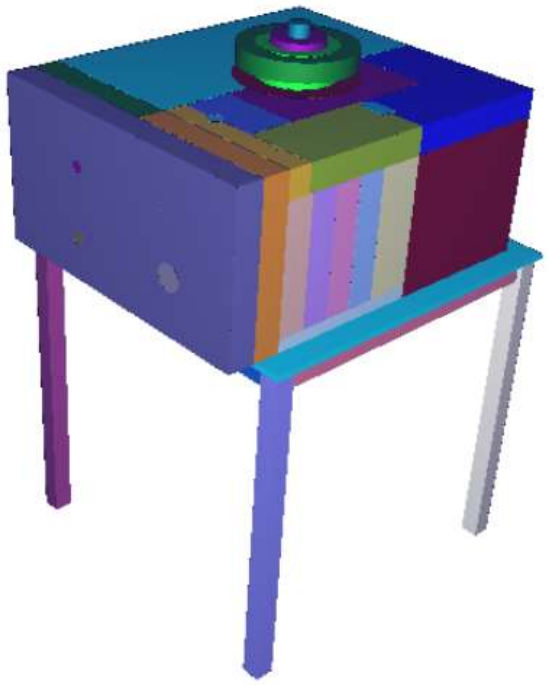

Figure 2.3 – MCNP simulation of DD-108M moderator

Ultimately, a second table-top neutron generator was brought into our laboratory. MCNP work that was initially developed on the DD-108M input was transferred to the new generator. Further development of the MCNP input was continued on that system as well.

2.2.2 DD-109M Neutron Generator System

A second neutron generator was brought into the laboratory and subsequent work on the project was carried out on it. The generator was an Adelphi Technology Inc. (Redwood City, CA) DD-109M neutron generator. The generator also utilizes the DD reaction to generate neutrons with 2.45 MeV of kinetic energy in the zero-degree direction. A neutron yield up to approximately 5 x 10^9 neutrons/second can be produced by the system. It has an integrated, non-removable polyethylene moderator built into the face of the system, to thermalize generated neutrons [79].

A confidential and not reproduced in this dissertation set of diagrams of the generator and target detail was received from the manufacturer. The diagrams allowed for the determination of

the sizes and relative positions of components within the generator, including the integrated moderator. The DD-109M generator was modelled in MCNP6, an updated general-purpose Monte Carlo code for radiation transport developed and maintained by Los Alamos National Laboratory [49]. A complete description of the input created for the DD-109M generator is given in Appendix B. Significant differences in design exist between the DD-108M and DD-109M generators. Instead of a copper-backed titanium wedge that deuterons are accelerated into, the DD-109M target is a disk of titanium backed by copper and water. The target, as modelled in MCNP6 is shown in figure 2.4.

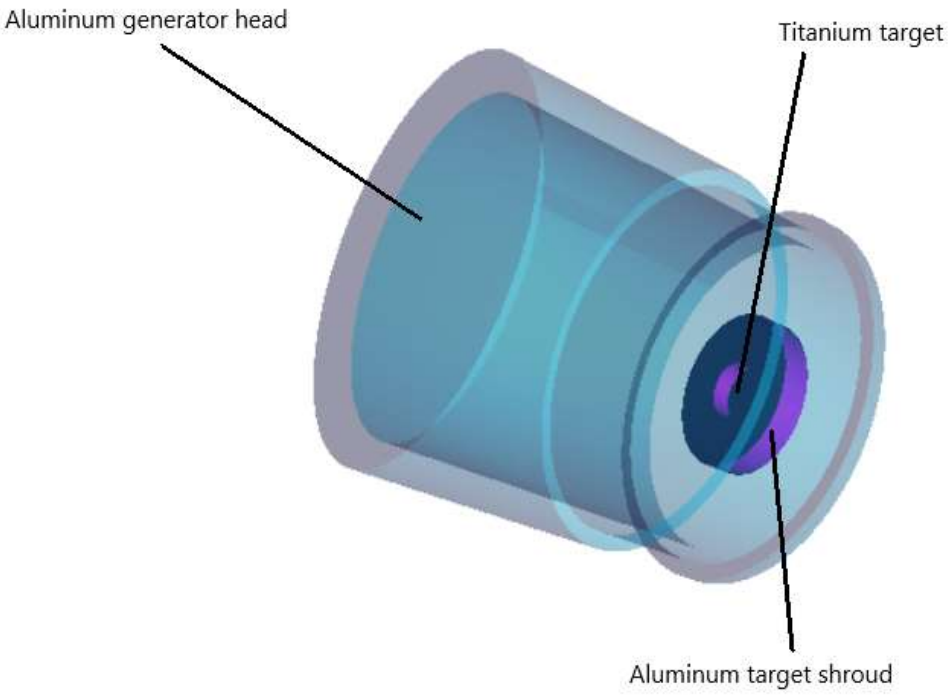

Figure 2.4 – MCNP simulation of DD-109M target

The complete DD-109M generator head and integrated moderator, as modelled in MNCP6 is demonstrated in Figure 2.5.

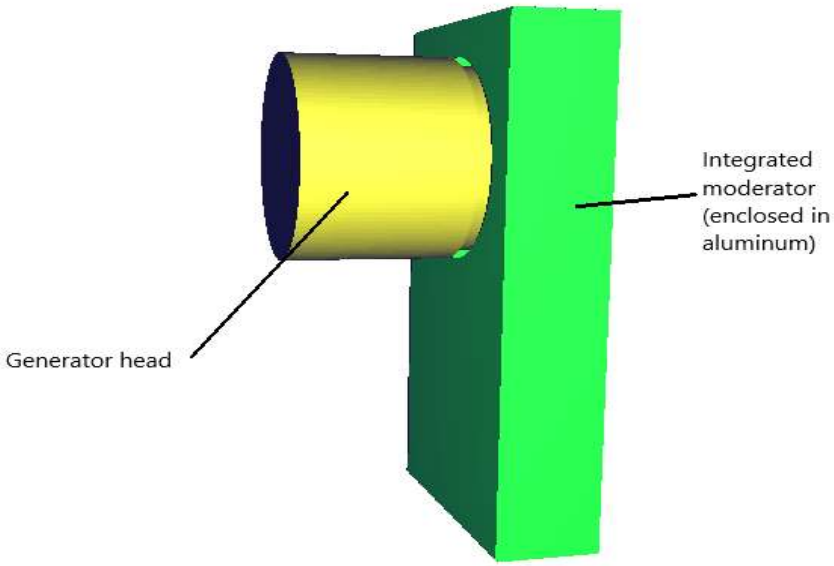

Figure 2.5 – MCNP simulation of DD-109M generator head and moderator

Figure 2.6 shows the generator, moderator/reflector supporting structure, and a portion of the moderator/reflector, in situ, in the laboratory. For clarity of demonstration, much of the surrounding moderator/reflector has been removed.

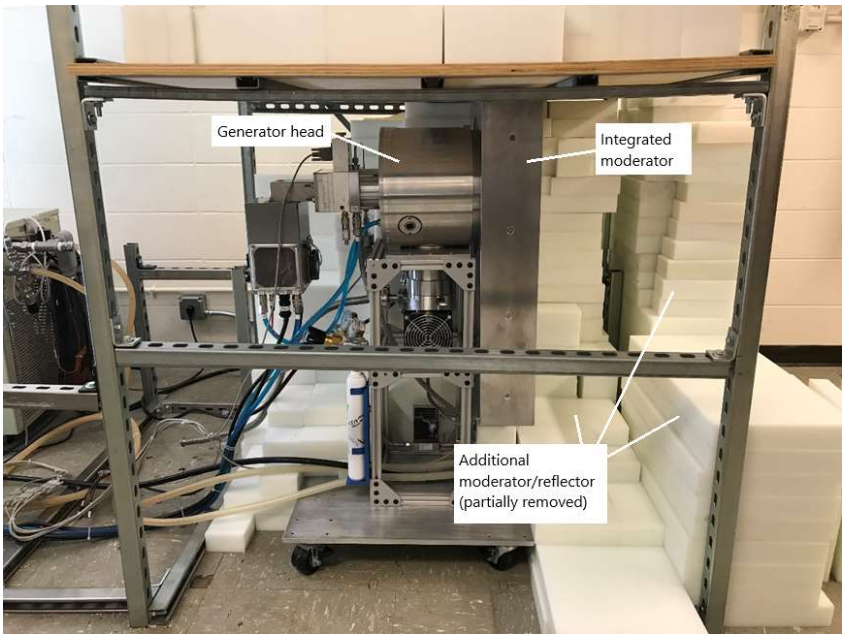

Figure 2.6 – DD-109M generator in the laboratory

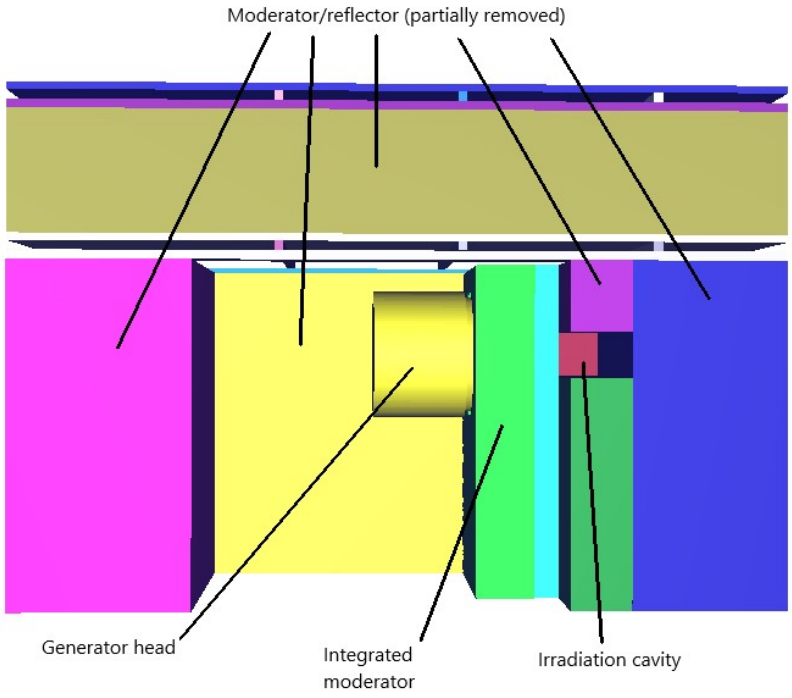

Figure 2.7 – MCNP simulation of complete DD-109M system

Figure 2.7 shows the generator, moderator/reflector supporting structure, and a portion of the moderator/reflector, as modelled in MCNP6. A portion of the moderator/reflector has been removed from the image to improve visualization of the generator system.

A significant improvement in MNCP modelling was provided by accounting for the kinematics of the DD reaction and the effect that would have on energy and angular distribution at the point of neutron emission. The DD reaction has a Q-value of 3.2688630 MeV and sources often list the kinetic energy of generated neutrons as having 2.45 MeV [49]. At zero degrees in the laboratory reference frame, the neutrons possess 2.87434 MeV, when produced by deuterons with 0.110 MeV of kinetic energy. As one deviates from zero degrees, the kinetic energy of the neutrons emitted at a particular angle changes. Additionally, the probability of a neutron being generated at a given angle is not constant. Accurate modeling of neutron interactions within MCNP must take these factors into account, especially since neutron interactions such as scattering and absorption (activation) are highly energy dependent.

MCNP6 can simulate light ion interactions directly, as it includes the CP2011 library, which has reaction cross sections for deuterons interacting with deuterons, for energies between 0.0001 and 10 MeV [80]. Simple simulations were performed to study direct neutron production via deuterons interacting with deuterium. A sphere of deuterium was modelled, with a source of deuterons being created in its middle. A total of 1×10^8 deuteron histories were simulated and the reaction results analyzed. Direct creation of neutrons was observed, but at very low energies, the probability is very low. As deuteron kinetic energy is increased, the likelihood of neutron production increases as well, as shown in table 2.3. Unfortunately, for this project, the neutron generator is typically operated at a potential of 0.11 MV, meaning the deuterons will have a kinetic energy of 0.11 MeV. The lower the probability of neutron creation per interaction, the greater the amount of computer time necessary to accumulate a significant number of neutrons. At 0.11 MeV and with this simplified geometry, it took 244.2 minutes of computer time to complete the simulation, which only produced 26 neutrons. This means that at energies the DD-109M generator is operated at, direct simulation of the DD reaction is not feasible.

Table 2.3 – Neutron production at various deuteron kinetic energies

Deuteron Kinetic Energy (MeV)	Neutrons Produced
0.11	26
0.18	46
0.25	131
0.5	543
4.5	44,229
9.5	152,015

A second approach to incorporating neutron kinematics into the MCNP input was developed. First, the probability of emission and energy per angle of the emitted neutrons created from the reaction of 0.11 MeV deuterons reacting with deuterium needed to be determined. This information can be generated using the DROSG-2000 program, which is a freeware program available through the International Atomic Energy Agency (http://www-nds.iaea.org). The program contains reaction data for 60 different accelerator reactions that produce neutrons. The program contains three different codes that allow for the generation of produced neutron energies, differential cross sections, yields, and spectra [81]. The code neuyie was utilized to generate the neutron energies and cross sections produced at various energies. Running the neuyie code involves selecting the type of nuclear reaction for which data is desired, entering the kinetic energy of the interacting particle, and specifying the number of angles that data is desired over. In the case of the DD-109M generator, operating at a potential of 0.11 MV, the $^{2}H(d, n)^{3}He$ reaction was selected and the energy of interacting particle was specified as 0.11 MeV. The neuyie code then displays the cross section and energy of the neutrons generated from the reaction in both the laboratory and center-of-mass reference frames. A portion of the 0.11 MeV deuteron-deuterium reaction data is displayed in figure 2.8.

1NEUTRONS FROM THE REACTION 2H(d,n)3He

INCIDENT LAB ENERGY 0.110000 INT. CROSS SECT.= 1.86856E+01 mb
Total energy= 3751.28086 MeV,Momentum of projectile= 10.1567,Q= 3.2688630

LABORATORY SYSTEM			CENTER-OF-MASS	
ANGLE	CROSS SECTION	ENERGY	ANGLE	CROSS
0.00	2.569	2.87434	0.00	2.225
3.05	2.564	2.87373	3.28	2.221
6.10	2.550	2.87192	6.56	2.210
9.15	2.526	2.86890	9.83	2.191
12.20	2.492	2.86469	13.11	2.166
15.25	2.451	2.85930	16.38	2.133
18.31	2.401	2.85276	19.65	2.095
21.36	2.345	2.84510	22.91	2.051
24.41	2.282	2.83634	26.17	2.002
27.46	2.214	2.82652	29.43	1.949
30.51	2.142	2.81568	32.68	1.893
33.56	2.067	2.80385	35.92	1.834
36.61	1.990	2.79110	39.16	1.773
39.66	1.912	2.77745	42.39	1.712
42.71	1.834	2.76297	45.61	1.650
45.76	1.757	2.74772	48.82	1.589
48.81	1.681	2.73174	52.03	1.530
51.86	1.609	2.71509	55.23	1.473
54.92	1.540	2.69784	58.41	1.418
57.97	1.475	2.68004	61.59	1.367
61.02	1.414	2.66177	64.76	1.320
64.07	1.359	2.64307	67.91	1.278
67.12	1.310	2.62402	71.06	1.240
70.17	1.266	2.60467	74.19	1.208
73.22	1.229	2.58510	77.31	1.181
76.27	1.198	2.56536	80.42	1.159
79.32	1.173	2.54551	83.52	1.144
82.37	1.154	2.52561	86.61	1.134
85.42	1.141	2.50573	89.68	1.131
88.47	1.135	2.48592	92.75	1.133
91.53	1.134	2.46625	95.80	1.141
94.58	1.138	2.44675	98.84	1.155
97.63	1.148	2.42749	101.86	1.174
100.68	1.163	2.40852	104.88	1.199
103.73	1.182	2.38989	107.88	1.228
106.78	1.206	2.37164	110.87	1.263
109.83	1.233	2.35382	113.85	1.301

Figure 2.8 – Portion of DROSG-2000 reaction output

From DROSG-2000, we directly get the neutron energy per angle and the energy distribution for 0.11 MeV deuterons interacting with deuterium, as shown in figure 2.9.

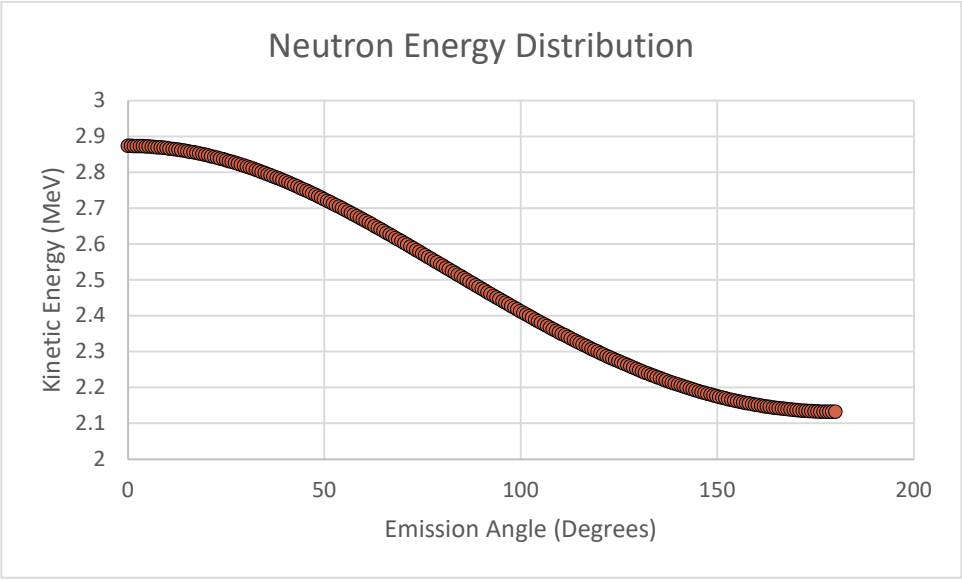

Figure 2.9 – Neutron energy distribution per angle

DROSG-2000 also generates cross-sections per angle, in units of millibarns, in both laboratory and center-of-mass reference frames. By dividing the cross section at a particular angle by the greatest cross section, you can generate the relative neutron intensity per angle. Figure 2.10 demonstrates the relative neutron intensity per angle for neutrons arising from the reaction of 0.2 MeV deuterons on deuterium. This was generated for comparison purposes to published data (displayed in figure 2.11), to verify that the use of the neuyie code produced valid results.

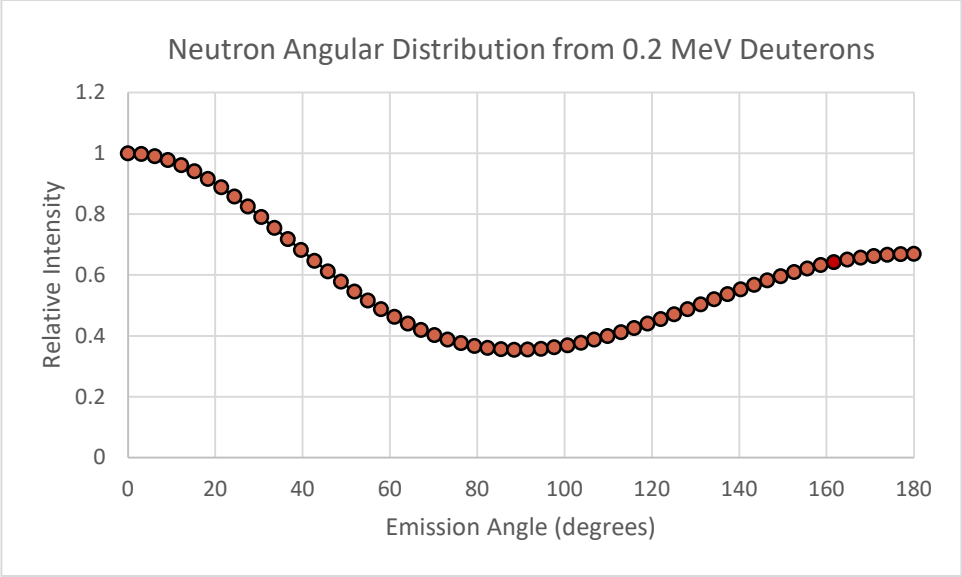

Figure 2.10 – Neutron angular intensity produced by 0.2 MeV deuterons using data generated by the DROSG-2000 code

FIG. 3. The angular distribution of the neutrons emitted in the $D(d,n)He^3$ reaction for an incident deuteron energy of 200 kev.

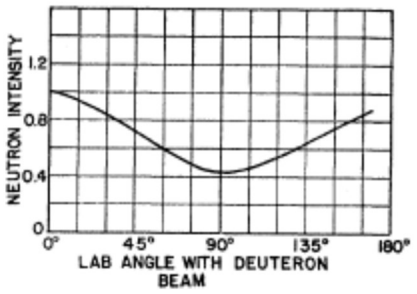

Figure 2.11 – Published neutron angular intensity produced by 0.2 MeV deuterons [82]

Figure 2.12 demonstrates the relative neutron intensity per angle produced from the reaction of 0.11 MeV deuterons with deuterium.

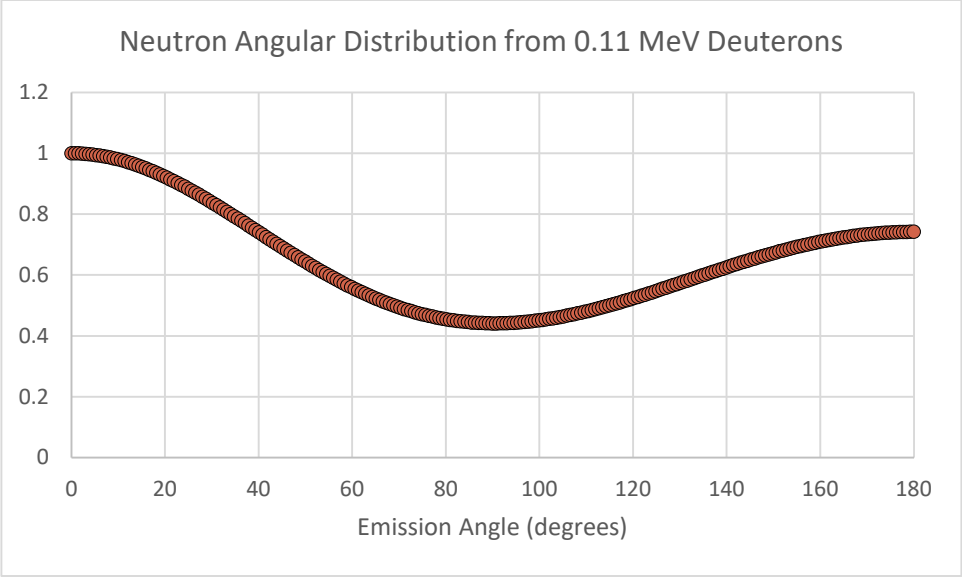

Figure 2.12 - Neutron angular intensity produced by 0.11 MeV deuterons using data generated by the DROSG-2000 code

The neutron energies and emission probabilities were coded directly into the MNCP6 input source definition (sdef) card by employing an energy distribution and a probability of angular emission distribution. The neutrons were generated at the surface of the titanium in the target material. The energy of the neutrons was specified as:

$$\text{erg} = \text{fdir} = \text{d3}$$

where fdir sets up a distribution of energies based on values specified in d3. D3 directs to the ds3 card, which is the dependent source distribution. By utilizing the L keyword with ds3, the values listed in the distribution are discrete source values. It is in ds3 that the kinetic energy values for the neutrons emitted at various angles are listed. The listed values were taken directly as computed by DROSG-2000. The range of angle emission (180 degrees) was divided up over 239 values, with an interval of approximately 0.76 degrees per step.

The probability of an emission of a neutron at a particular angle was specified as a distribution of the neutron direction (dir) in the source definition. Describing a distribution of source particles necessitates uses of a source information (si) card as well as a source probability (sp) card. The source information card incorporated the L keyword, which signifies that its

values are discrete source variables. On the source information card, each possible angle of emission was listed, specified from cosine (-1) to cosine (1). The source probability card contained the probabilities for each bin defined on the source information card. For each possible angle of emission, it was necessary to list the likelihood a neutron would be emitted at that angle. These values were calculated using the cross section information produced by DROSG-2000. An individual cross section represents a probability and by dividing a particular angle's probability by the sum of all the cross sections, you find the relative probability of emission at a particular angle. These values were specified on the sp card.

Using this source definition, MNCP6 would create neutrons at the surface of the titanium target, near to where they would actually be created in the generator. Neutrons created in MCNP would be biased according to angle, with the probability of angular emission taken into account. Additionally, dependent on the angle of emission, the neutron would be created with a kinetic energy governed by kinematic requirements.

A simple activation experiment was conducted with the DD-109M neutron generator to verify if the anisotropic source specification was valid. Six gold foils were irradiated at three locations within the irradiation cavity. Each location had two foils separately irradiated at it and each provided a marked difference in geometry. A polyethylene block was placed in the irradiation cavity, with a lead sheet on one side and a second lead sheet below it. Two foil locations were in the cavity facing the generator, with the lead sheet and polyethylene block in between the generator and foils. One of the facing locations had the foils in contact with the lead sheet and on the centerline of the generator (location C). The second facing location was off the centerline by 4.5 centimeters and with the foils placed 3.2 centimeters further away from the generator (location B). The third foil location was 19.0 centimeters off the centerline, 2.5 centimeters closer to the face of the generator compared to the foil location on the centerline, and with the foils turned so that the thin edge faced the generator (location A). Figures 2.13 and 2.14 show Visual Editor images of the foils relative to each other, the polyethylene block, and the two lead sheets.

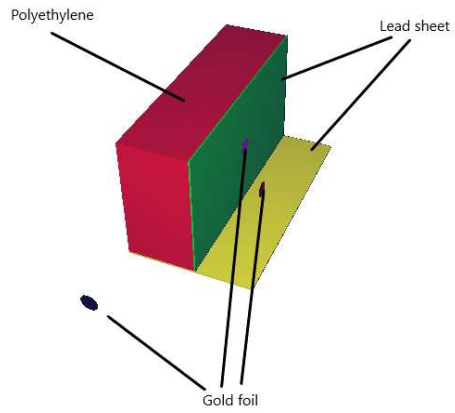

Figure 2.13 – Visual Editor image of three gold activation foils in the irradiation cavity

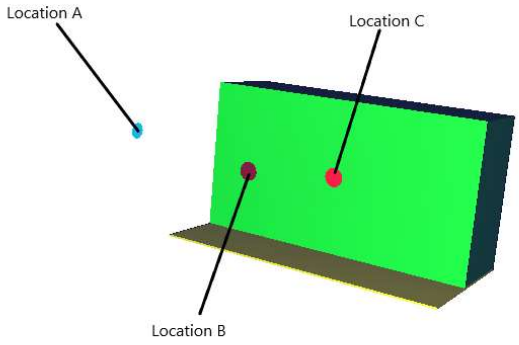

Figure 2.14 – Visual Editor image of three gold activation foils in the irradiation cavity as displayed at another angle

Two simulations were carried out with this geometry: one with an isotropic source specification of 2.45 MeV neutrons and a second with an anisotropic source specification determined with the data from DROSG-2000. Gold foils at the three described locations were

included in both simulations. The foils were 1.27 centimeters in diameter, 5.08×10^{-3} centimeters thick, and possessed a density of 19.3 grams/cm^3. An F4 tally was set up for each of the foils to calculate the number of ^{198}Au atoms created by the activation of ^{197}Au. The isotropic source specification was executed with 1×10^7 neutrons simulated and the anisotropic simulation was executed with 4×10^7 neutrons simulated. It was necessary to increase the number of simulated neutrons with the anisotropic specification to maintain the tally variance below 0.05, a value considered reliable. The results of the two simulations are presented in table 2.4.

Table 2.4 – MCNP simulated amounts of activation of gold foils

Location	Anisotropic simulation (atoms/source particle)	Isotropic simulation (atoms/source particle)	Simulation result percent difference
A	2.417×10^{-6}	1.248×10^{-5}	-416.44%
B	1.235×10^{-5}	7.386×10^{-6}	40.20%
C	1.381×10^{-5}	8.466×10^{-6}	61.29%

Six foils were irradiated in the irradiation cavity, in the exact geometries simulated in MCNP6. Two foils each were irradiated at locations A, B, and C. The weight of each foil was measured prior to irradiation. Each foil was irradiated in its respective location for a period of three minutes with the generator operated at 110 keV. Once an irradiation was complete, the foil was transferred to a high purity germanium (HPGe) detector and a spectrum was acquired for a period of five minutes. A standard transfer time of two minutes from the end of the irradiation to the start of the spectrum acquisition was allotted. The spectra were analyzed and the number of counts falling within the 411.8 keV photopeak were counted. Each count was considered as evidence of the formation of an atom of ^{198}Au, which emits a 411.8 keV gamma ray in 95.62% of decays. The results of the irradiation are presented in table 2.5.

Table 2.5 – Gold foil activation results

Location	Counts	Foil weight (g)	Counts per gram	Location average (counts per gram)
A	173	0.1269	1.363×10^3 +/- 1.04×10^2	1.378×10^3 +/- 1.05×10^2
A	173	0.1243	1.392×10^3 +/- 1.06×10^2	
B	686	0.1243	5.519×10^3 +/- 2.12×10^2	5.753×10^3 +/- 2.16×10^2
B	749	0.1251	5.987×10^3 +/- 2.21×10^2	
C	855	0.1294	6.607×10^3 +/- 2.27×10^2	6.277×10^3 +/- 2.22×10^2
C	770	0.1295	5.946×10^3 +/- 2.16×10^2	

The greatest amount of neutron activation occurred at location C, which was on the midline of the generator with the foils facing it. Slightly less activation was realized at location B, which was off the midline but still with the foils facing the generator. Location A, which was the greatest distance from the midline and had the foils turned so that their edges were facing the generator saw the least amount of activation.

The results of the foil activation experiment were compared to the simulations that were carried out with the two different source specifications. The isotropic simulation predicted that the greatest amount of activation would occur at Location A, which in the experiment demonstrated the least amount of activation. Following A, the isotropic simulation predicted C would have the second most activation, followed closely behind by Location B. The anisotropic simulation correctly predicted that Location C would have the greatest amount of activation, followed by Location B, and then followed by a significantly reduced amount of activation at Location A. Relative comparisons of the amounts of activation at the three locations are displayed in table 2.6. From the relative comparisons, we find that the anisotropic simulation was able to accurately simulate the amounts of activation that were produced by the neutron generator. Conversely, the isotropic simulation failed to accurately determine the relative activation at locations around the irradiation cavity. These results verify that utilizing the anisotropic source specification is an appropriate method for incorporating neutron kinematics into the MCNP6 simulation. Additionally, for situations that involve irradiating large volume

sources or that include the influence of surrounding materials such as moderator/reflector optimization, it is imperative to incorporate neutron kinetic energy and angular emission probabilities into the source specification to maintain accuracy.

Table 2.6 – Relative amounts of simulated activation at the three foil locations

Location	Measured data	Anisotropic simulation	Isotropic simulation
A/B	0.24 +/- 0.02	0.20 +/- 0.01	1.69 +/- 0.07
A/C	0.22 +/- 0.02	0.18 +/- 0.01	1.47 +/- 0.06
B/C	0.92 +/- 0.05	0.89 +/- 0.02	0.87 +/- 0.04

2.2.3 Addition of Aluminum Phantoms to Generator Inputs

The DD-109M input was altered to include the simulation of a phantom that was to be irradiated. Cylindrical, plastic containers, to which known amounts of water and aluminum could be added, were chosen as the phantoms. It was determined that three quantities of aluminum would be simulated: 1 milligram, 3 milligrams, and 5 milligrams. The aluminum was to be added to deionized water so that the total volume of the fluid in the plastic phantom would be 5 cm^3. In addition to the known amounts of aluminum, a phantom containing 5 cm^3 of water without any added aluminum, would be irradiated as a blank. The phantoms contained a radius of 0.75 centimeters. Knowing that 5 cm^3 of total fluid was to be added to the cylinder, the height was determined as:

$$height = \frac{5\ cm^3}{(\pi)(0.75\ cm)^2} = 2.82942121\ cm \qquad \text{(Equation 27)}$$

The phantom was specified as a cell having a density equal of 1 gram/cm^3 which was equal to water. It was a cylinder with a height of 2.82942121 centimeters and a radius of 0.75 centimeters, placed at the midline of the irradiation cavity.

For each quantity of aluminum to be simulated, it was necessary to modify the material contained in the phantom cell. The material number of the phantom cell was specified as m208 and contained water and aluminum. Water was broken down into its elemental components of hydrogen and oxygen. Each of the three elemental contents of the phantom material were

described as their weight fraction of the cell, making it necessary to compute each separately for listing in the input. The aluminum was added to 5 milliliters of water, which had a weight of 5 grams. Computation of the weight fractions for the addition of 1 milligram of aluminum to 5 grams of water was as follows:

$$Al: \frac{0.001\ g\ Al}{5.001\ g\ phant} = 0.00019996 \qquad \text{(Equation 28)}$$

$$H_2O: \frac{5.0\ g\ H_2O}{5.001\ g\ phantom} = 0.99980004 \qquad \text{(Equation 29)}$$

Due to water being composed of two elements, it was necessary to determine the weight fraction of each component. This was performed as:

$$H: \frac{2.016}{18.015} = 0.111906744\ x\ 0.99980004 = 0.11188436712747 \qquad \text{(Equation 30)}$$

$$O: \frac{15.999}{18.015} = 0.888093256\ x\ 0.99980004 = 0.88791567287253 \qquad \text{(Equation 31)}$$

The weight fractions for the 3 milligrams and 5 milligrams aluminum phantoms were similarly computed and are given in table 2.7.

Table 2.7 – Phantom compositions

Aluminum mass (g)	Aluminum weight fraction	Hydrogen weight fraction	Oxygen weight fraction
0.001	0.00019996	0.11188436712747	0.88791567287253
0.003	0.00059964	0.11183964024003	0.88756071975997
0.005	0.000999001	0.11179494905084	0.88720604994916

A second modification to the DD-109M MNCP6 input necessary for the simulation of the phantoms was revision of the activation tally. An F4 tally was employed to determine the amount of created Al-28. As previously described, F4 tallies give flux averaged over a cell in units of neutrons/cm^2. The tally can be modified to yield the number of activated atoms using

the tally multiplier, FM, and segment divisor, SD, cards. The tally multiplier card takes the form:

FM# c m i

where # specifies the tally number, c is a multiplicative constant, m is the material number of the sample under consideration, and i is the evaluated nuclear data file (ENDF) number for the reaction of interest. The determination of the multiplicative constant requires the inclusion of the mass and density of the material under analysis. As an example, for the 0.001 gram of aluminum phantom, the multiplicative constant was calculated to be:

$$c = \frac{6.0220434469282x10^{23} atoms}{mol} * \frac{mol}{26.981538\ g} * \frac{1x10^{-2}\ cm^2}{barn} *\ 0.001\ g \quad \text{(Equation 32)}$$

$$= 0.000022319126$$

where 6.0220434469282x10^{23} atoms/mol is Avogadro's constant and 26.981538 g/mol is the molar mass of aluminum. The multipliers for 0.003 grams and 0.005 grams phantoms were similarly computed and are summarized in table 2.8.

Table 2.8 – Calculated multiplicative constant versus aluminum mass

Mass of aluminum (g)	Multiplicative constant
0.001	0.000022319
0.003	0.000066958
0.005	0.000111597

The material number is specified as the same as what is listed in the input for aluminum, 208 in the case of the DD-109M MCNP simulation. The specification of the reaction number, i, is taken from the standard list of ENDF reactions. As we are interested in neutron capture, the reaction 102, denoting the (n, γ), was chosen. To have the tally measure all the aluminum-28 atoms activated in the cell containing the phantom, it is necessary to also specify a segment divisor card. The segment divisor card takes the form:

where # is the tally number and the number 1 directs the tally to integrate over the complete cell.

2.2.4 Production of Aluminum Phantoms

Thin-walled, plastic cylinders having a radius of 0.75 centimeters and a height of 7.5 centimeters were acquired. A series of 12 phantoms were produced using the plastic cylinders, pictured in figure 2.15. The phantoms were made as follows: three containing 5 milliliters of deionized water only, three containing 0.001 gram of aluminum in deionized water, three containing 0.003 gram of aluminum in deionized water, and three containing 0.005 gram of aluminum in deionized water.

Figure 2.15 – Image of plastic phantom container

The added aluminum was in the form of an atomic absorption spectroscopy aluminum standard produced by Acros Organics (Fair Lawn, NJ). The standard was composed of 1 milligram of aluminum per milliliter in 2-5% nitric acid. The standard was pipetted into the plastic cylinders and then deionized water was added to bring the volume up to five milliliters. The phantoms were made according to the specifications listed in table 2.9.

Table 2.9 – Phantom fluid volumes

Mass of aluminum (g)	Volume of aluminum standard (mL)	Volume of deionized water (mL)
0.001	1	4
0.003	3	2
0.005	5	0

2.3 Results

The results of the simulation of the virtual phantoms are displayed in table 2.10. The tally variances of all simulations were acceptable and the results should be considered valid. The tally results can be used to determine the amount of aluminum-28 that would be produced via neutron activation. This estimation can be compared to an actual irradiation experiment to determine simulation accuracy.

Table 2.10 – Phantom simulation activation results

Aluminum in virtual phantom	Tally result (Al-28 produced per source particle)	Tally variance
1 milligram	9.18230×10^{-9}	0.0034
3 milligrams	2.75469×10^{-8}	0.0034
5 milligrams	4.59093×10^{-8}	0.0034

The 5-milligram simulated phantom resulted in a tally of 4.59093×10^{-8} atoms of Al-28 per source particle. The DD-109M generator has a yield of approximately 1×10^{9} neutrons per second. For an irradiation of 360 seconds, the resulting number of Al-28 atoms at the end of the irradiation will be:

$$Al - 28\ atoms = \frac{4.59093x10^{-8}\ atoms}{neutron} * \frac{1x10^{9} neutrons}{second} *\ \tau * \left[1 - e^{-(360\ s)(0.005145\ s^{-1}}\right]$$

$$= 7.523x10^{3}$$

(Equation 33)

where τ is the inverse of the decay constant and is equal to 193.46 seconds for aluminum-28. The factor [1-$e^{-\lambda t}$] accounts for radioactive decay during the irradiation period.

Following the irradiation, there was a 90 second transfer period from the irradiation cavity to the HPGe detector, during which some of the Al-28 decayed. The number of Al-28 atoms remaining at the end of the transfer period would be:

$$Al - 28\ atoms = (7.523x10^{3})e^{-(90\ s)(0.00514\ \ \ ^{-1})} = 4.735x10^{3} \quad \text{(Equation 34)}$$

Following the transfer period, the sample was counted on a HPGe detector for 600 seconds. The number of atoms remaining at the end of the 600 second detection period was:

$$N_t = (4.735x10^{3})e^{-(600\ s)(0.005145 s^{-1})} = 2.161x10^{2} \qquad \text{(Equation 35)}$$

During the count period, the total number of atoms that decayed and were therefore able to be counted was:

$$7.523x10^{3} - 2.161x10^{2} = 7.307x10^{3} \qquad \text{(Equation 36)}$$

In a similar manner, the results for the 1-milligram Al and 3-milligram Al phantoms were computed. All are summarized in table 2.11.

Table 2.11 – Al-28 atoms at different experimental time points

Al Phantom	Total Number of Activated Atoms at End of Irradiation	Remaining Al-28 Atoms at End of Transfer Period	Remaining Al-28 Atoms at End of Detection Period	Total Number of Decays During Detection Period
1-mg	$1.505x10^3$	$9.470x10^2$	$3.409x10^1$	$1.471x10^3$
3-mg	$4.514x10^3$	$2.841x10^3$	$1.297x10^2$	$4.384x10^3$
5-mg	$7.523x10^3$	$4.735x10^3$	$2.161x10^2$	$7.307x10^3$

2.3.3 Quantification of Neutron Activation

The nine aluminum containing phantoms and three deionized water blank phantoms were irradiated with the DD-109M neutron generator. Each phantom was irradiated for a period of 360 seconds. Upon completion of the irradiation, a standardized period of 90 seconds was observed, allowing time to transfer a phantom from the DD-109M irradiation chamber to the GEM100P4-95 HPGe detector. At the end of the 90 second transfer period, a spectrum from each phantom was accumulated over a period of 600 seconds. Spectrum counts in the energy range of 1,776.08 keV to 1.780.85 keV were considered to arise from the decay of aluminum-28.

The results of the phantom irradiations and spectra acquisitions are given in table 2.12.

Table 2.12 – Amounts of counts detected from each phantom

Phantom Identification	Total Al-28 Counts	Phantom Series Average
Water Blank 1	15	19.67
Water Blank 2	16	
Water Blank 3	28	
1 mg Aluminum Added 1	38	50.33
1 mg Aluminum Added 2	53	
1 mg Aluminum Added 3	60	
3 mg Aluminum Added 1	101	105.33
3 mg Aluminum Added 2	113	
3 mg Aluminum Added 3	102	
5 mg Aluminum Added 1	187	183.33
5 mg Aluminum Added 2	184	
5 mg Aluminum Added 3	179	

The results of subtracting the water blank average of 19.67 counts from each of the aluminum added phantoms are given in table 2.13.

Table 2.13 – Net counts detected from each aluminum mass

Phantom	Raw Series Average Counts	Net Series Average Counts
1 mg Aluminum Added	50.33	30.67
3 mg Aluminum Added	105.33	85.67
5 mg Aluminum Added	183.33	163.67

Plotting the raw series average counts versus the amount of aluminum added, resulted in figure 2.16. The equation of the trendline is displayed on the graph and has been set to a y-intercept equal to zero. Assuming a background of approximately 20 counts arising from the container and deionized water and using the value given by Alvarez in section 1.3.2.2 of a detection limit of 26.9 counts based on a measured background of 20, the absolute minimum amount of aluminum that can be confidently detected with these experimental parameters is:

$$26.9 = 36.656\,x \rightarrow x = \frac{26.9}{36.656} = 0.73\,milligrams\ of\ Al \quad \text{(Equation 37)}$$

This represents the minimal amount of aluminum that can be measured at the detection limit of the system in the presence of 20 background counts. In practice, due to prevalence of aluminum in the environment, the background signal of aluminum can vary greatly. Changes in the background level can significantly affect the detection limit. At a background of 1, the detection limit of this system would be 0.34 milligrams of aluminum.

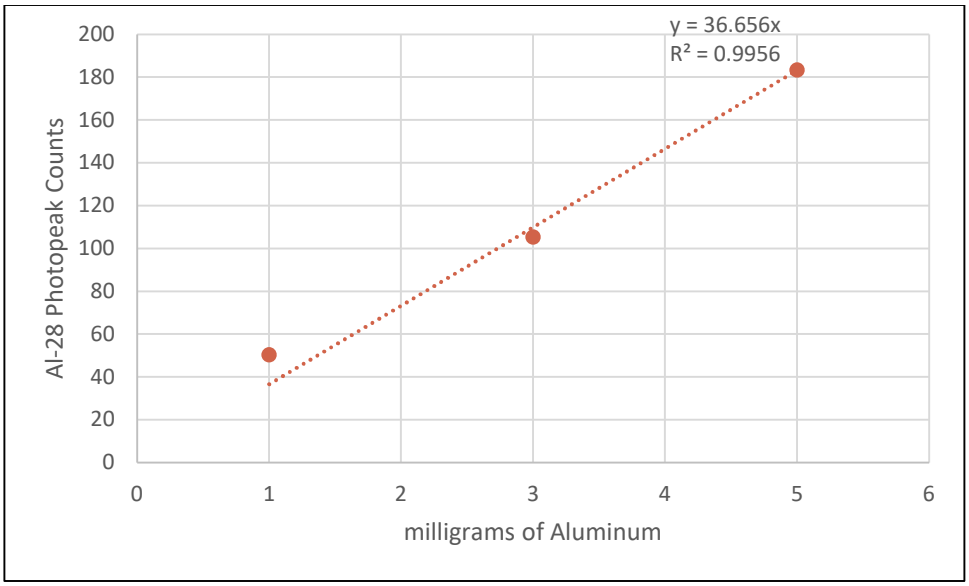

Figure 2.16 – Al-28 photopeak counts as a function of aluminum mass

2.3.4 Comparison of Simulated and Measured Neutron Activation

A comparison can be made between the amount of simulated Al-28 activation generated and the actual measured Al-28 activation, in the 1-milligram, 3-milligram, and 5-milligram phantoms. To make the comparison, it was necessary to estimate the radiation detection efficiency of the HPGe detector that was used to measure the Al-28 activation and apply that efficiency factor to the amount of Al-28 activated in the DD-109M, as simulated in MCNP6. This was necessary to determine what fraction of the simulated activity would be detected by the actual HPGe system.

The measurement of HPGe efficiency could not be carried out directly by measuring Al-28, due to its short half-life. A surrogate radioisotope would be necessary, and it would have to have a photon energy close to that of the 1.779 MeV gamma ray from Al-28 to ensure accuracy. The radioisotope selected was Y-88, which has a half-life of 106.63 days and emits a 1.836 MeV gamma ray in 99.4% of decays.

A multi-nuclide calibration source containing Y-88 was obtained and a measurement of was taken on the GEM100P4-95 HPGe detector for a period of 900 seconds of live time. Due to the presence of other nuclides in the calibration source, the dead time was 15.4%, resulting in a detector live time of only 761.8 seconds. The size of the calibration source was relatively similar

that of the aluminum phantoms, ensuring that geometry differences should not negatively impact the efficiency measurement in a negative manner.

Analyzing the spectrum acquired on the multi-nuclide source, the 1.836 MeV gamma ray yielded 12,312 net peak counts in 761.8 seconds, for a photopeak count rate of 16.175 counts per second. The Y-88 activity at the time of the count was 660.3770345 becquerels. The 1.836 MeV gamma ray occurs in 99.4% of decays, meaning the gamma ray activity of this source would be 656.408 gamma rays per second. The resulting efficiency of the GEM100P4-95 HPGe detector at 1.836 MeV was:

$$\frac{16.175\ counts\ per\ second}{656.408\ gamma\ rays\ per\ second} = 0.024641686 \text{ (Equation 38)}$$

Applying the measured efficiency factor to the simulated Al-28 phantoms results in an estimate of the recovered counts. For the simulation of 5-milligram Al phantom counted for 600 seconds, the recovered counts would be:

$$Al - 28\ Counts\text{:}\ (7.307\ x10^3)x(0.024641686) = 180.06 \text{ (Equation 39)}$$

Compare 180.06 counts in 600 seconds to the actual measurement value of 163.67 net counts in 600 seconds from the 5-milligram Al phantom. The percent difference between the simulated and measured values can be computed as:

$$Percent\ Difference = \frac{|x_1 - x_2|}{\frac{(x_1 + x_2)}{2}} x100 \text{ (Equation 40)}$$

A summary of the results comparing the simulation to the actual measurements is given in table 2.14.

Table 2.14 – Comparison of measured and simulated counts for each aluminum phantom

Aluminum Quantity	Net Measured Counts	Simulated Counts	Percent Difference
1-mg	30.67	36.24	16.65%
3-mg	85.67	108.04	23.10%
5-mg	163.67	180.06	9.54%

2.3.5 Quantification of Radiation Dose

The performance of in vivo measurements of aluminum in humans will most likely be performed by irradiating a person's hand placed in the irradiation cavity. The DD-109M MCNP6 input was modified to include a simulated human hand in the irradiation chamber and dose tallies were developed to estimate received absorbed and equivalent doses from a simulated activation experiment.

The simulated hand was modelled as a rectangular slab of bone with two rectangular slabs of soft tissue on either side. The bone slab was 1 centimeter x 7 centimeters x 9.324 centimeters for a total volume of 65.27 cm^3, a physical density of 1.85 $gram/cm^3$, and a total weight of 120.75 grams. This was in agreement of the estimated fresh bone mass of a human hand of 120.75 grams, as specified by the ICRP [83]. The elemental and isotopic composition was in accordance with ICRP specification and is summarized in table 2.15 [84]. The two soft tissue slabs were modelled as rectangular slabs having dimensions of 0.2 centimeter x 7 centimeters x 9.324 centimeters. The 0.2 centimeter thickness was in accordance with the skin thickness specified by the ICRP [84]. The physical density of the soft tissue was 1.0 $gram/cm^3$, resulting in a total mass of 13.0536 grams. The elemental and isotopic composition of the soft tissue was in accordance with the specifications of the ICRU and is summarized in table 2.16 [85].

Table 2.15 – ICRP cortical bone specification

Isotope	Weight Fraction	Isotopic Fraction	Isotopic Weight Fraction
Hydrogen-1	0.047234	0.999885	0.04722856809
Hydrogen-2	0.047234	0.000115	0.00000543191
Carbon-12	0.14433	0.9893	0.14278566900
Carbon-13	0.14433	0.0107	0.00154433100
Nitrogen-14	0.04199	0.99636	0.04183715640
Nitrogen-15	0.04199	0.00364	0.00015284360
Oxygen-16	0.446096	0.99757	0.44501198672
Oxygen-17	0.446096	0.00243	0.00108401328
Magnesium-24	0.0022	0.7899	0.00173778000
Magnesium-25	0.0022	0.1	0.00022000000
Magnesium-26	0.0022	0.1101	0.00024222000
Phosphorus-31	0.10497	1	0.10497000000
Sulfur-32	0.00315	0.9499	0.00299218500
Sulfur-33	0.00315	0.0075	0.00002362500
Sulfur-34	0.00315	0.0425	0.00013387500
Sulfur-36	0.00315	0.0001	0.00000031500
Calcium-40	0.20993	0.96941	0.20350824130
Calcium-42	0.20993	0.00647	0.00135824710
Calcium-43	0.20993	0.00135	0.00028340550
Calcium-44	0.20993	0.02086	0.00437913980
Calcium-46	0.20993	0.00004	0.00000839720
Calcium-48	0.20993	0.00187	0.00039256910
Zinc	0.0001	1	0.00010000000

Table 2.16 – ICRU soft tissue specification

Isotope	Weight Fraction	Isotopic Fraction	Isotopic Weight Fraction
Hydrogen-1	0.101172	0.999885	0.10116036522
Hydrogen-2	0.101172	0.000115	0.00001163478
Carbon-12	0.111	0.9893	0.10981230000
Carbon-13	0.111	0.0107	0.00118770000
Nitrogen-14	0.026	0.99636	0.02590536000
Nitrogen-15	0.026	0.00364	0.00009464000
Oxygen-16	0.761828	0.99757	0.75997675796
Oxygen-17	0.761828	0.00243	0.00185124204

Three different tallies were setup to determine radiation doses in the different sections of the hand phantom. A tally of type 8 was created to calculate the neutron equivalent dose in the bone section. A tally of type 6 was created to calculate the neutron equivalent dose in the bone as well as the skin sections. Finally, a tally of type 6 was created to calculate the absorbed doses due to neutrons, photons, and electrons in the skin and bone sections of the phantom.

The tally of type 8 used to determine the neutron equivalent dose in the bone section was of the form:

```
*f8:n 51
e8 0.01 0.1 2 20 T
em8 6.6342745e-12 1.32685e-11 2.6537098e-11 1.32685e-11
```

Designating the tally with an asterisk causes MCNP6 to compute the tally in the energy unit MeV per source particle. The tally result is divided by the tally energy card e8 into four energy bins: 0 to 0.01 MeV, 0.01 to 0.1 MeV, 0.1 to 2 MeV, and 2 to 20 MeV. The energy bins correspond to the energy ranges of the various radiation weighting factors assigned to neutrons by ICRP 60 [86], which are dependent on kinetic energy and are given in table 2.17. This allows separate radiation weighting factors to be applied to each energy bin and therefore calculate the total neutron equivalent dose. The application of the radiation weighting factor to each bin was performed using the energy multiplier card. The energy multiplier card multiplier constant not only applied the respective radiation weighting factor but it also converted the output of the tally from MeV per source particle to sievert per source particle. To make the conversion from energy to dose equivalent, the tally result is divided by the mass of the cell, the units are converted from MeV to joules, and the radiation weighting factor applied. For example, the first energy multiplier was calculated by:

$$\frac{MeV}{120.75\ g} * \frac{1000\ g}{kg} * \frac{1.6021773x10^{-13}J}{MeV} * 5 = \frac{6.6342745x10^{-12}sievert}{sour\quad particle} \qquad \text{(Equation 41)}$$

Table 2.17 – ICRP 60 neutron radiation weighting factors

Neutron Kinetic Energy (MeV)	Radiation Weighting Factor W_r
< 0.01	5
0.01 – 0.1	10
0.1 – 2	20
2 – 20	10
> 20	5

A tally of type 6 was developed to calculate the equivalent doses in both the skin and bone sections of the phantom from neutrons. Three separate tallies of type 6 had to be specified so that the equivalent doses could be determined in each of the two sections of skin and the section of bone. Tally 6 computes in units of MeV/g per source particle. The tally was divided up into four energy bins using the tally energy card e6. The bins ranged from 0 to 0.01 MeV, 0.01 to 0.1 MeV, 0.1 to 2 MeV, and 2 to 20 MeV. These bins corresponded to the energy bins specified by ICRP for the neutron radiation weighting factors. The energy multiplier card was utilized to modify the result of each bin from MeV/g per source particle to sievert per source particle. The form of the tally 6 specification was as follows:

```
f56:n 50
e56 0.01 0.1 2 20 T
em56 8.0108865e-10 1.6021773e-9 3.2043546e-9 1.6021773e-9
```

The computation of the energy multiplier constants converted the MeV/g per source particle to sievert per source particle. The tally automatically divides the result by the mass of the cell being tallied, so this did not factor into the multiplier calculation as in the tally 8 specification. For example, the computation of the first multiplier was as follows:

$$\frac{MeV}{g} * \frac{1000\,g}{kg} * \frac{1.6021773x1^{\ -13}J}{MeV} * 5 = \frac{8.0108865x10^{-10}sievert}{source\ particle} \quad \text{(Equation 42)}$$

The third tally developed was also of type 6 but it was utilized to compute the absorbed doses in the skin and bone sections from neutrons, photons, and electrons. Tally 6 computes directly in absorbed dose in units of MeV/g per source particle. That computation result can easily be converted to traditional or S.I. units of absorbed dose. The tally was employed as nine separate tallies, three for each of the two sections of skin and one section of bone. Three of the

tallies computed the absorbed dose from neutrons, three the absorbed dose from electrons, and three the absorbed dose from photons. The tally specification was as follows:

f116:n 50
f126:n 51
f136:n 52
f146:p 50
f156:p 51
f166:p 52
f176:e 50
f186:e 51
f196:e 52

where the letters n, p, and e designate neutrons, photons, and electrons, respectively and the values 50, 51, and 52 designate the cells containing skin, bone, and skin, respectively. The tally results were computed as MeV/g per source particle, which could be converted to gray (Gy) per source particle by multiplying by a factor of $1.6020506 \times 10^{-10}$, which converts MeV to joule.

The DD-109M MNCP6 input, with the specified hand phantom, was simulated with 1×10^{8} neutrons. All tally results had variances less than 0.05, a level of which is considered reliable. The results are given in table 2.18.

Table 2.18 – Radiation dose simulation results

Tally Type	Result	Particle	Cell	Units
8	3.29489×10^{-14}	Neutron	Bone (51)	Sievert/s.p.
6	6.64778×10^{-14}	Neutron	Skin (50)	Sievert/s.p.
6	2.85020×10^{-14}	Neutron	Bone (51)	Sievert/s.p.
6	4.56827×10^{-14}	Neutron	Skin (52)	Sievert/s.p.
6	$4.5725087 \times 10^{-15}$	Neutron	Skin (50)	Gray/s.p.
6	$2.0389618 \times 10^{-15}$	Neutron	Bone (51)	Gray/s.p.
6	$3.1902595 \times 10^{-15}$	Neutron	Skin (52)	Gray/s.p.
6	$1.9589074 \times 10^{-15}$	Photon	Skin (50)	Gray/s.p.
6	$1.7365908 \times 10^{-15}$	Photon	Bone (51)	Gray/s.p.
6	$1.6017398 \times 10^{-15}$	Photon	Skin (52)	Gray/s.p.
6	$1.8894425 \times 10^{-15}$	Electron	Skin (50)	Gray/s.p.
6	$1.7348926 \times 10^{-15}$	Electron	Bone (51)	Gray/s.p.
6	$1.5443880 \times 10^{-15}$	Electron	Skin (52)	Gray/s.p.

The irradiations used in this work had a duration of 360 seconds at a flux of approximately of 1 x 10^{9} neutrons per second for a total of 3.6 x 10^{11} source particles. At this irradiation level, the resulting total radiation doses to the hand are summarized in table 2.19.

Table 2.19 – Total simulated radiation doses

Dose Type	Particle	Cell	Total Dose	Units
Equivalent Dose	Neutron	Bone (51)	1.19 x 10^{-2}	Sieverts
Equivalent Dose	Neutron	Skin (50)	2.39 x 10^{-2}	Sieverts
Equivalent Dose	Neutron	Bone (51)	1.02 x 10^{-2}	Sieverts
Equivalent Dose	Neutron	Skin (52)	1.64 x 10^{-2}	Sieverts
Absorbed Dose	Neutron	Skin (50)	1.65 x 10^{-3}	Gray
Absorbed Dose	Neutron	Bone (51)	7.34 x 10^{-4}	Gray
Absorbed Dose	Neutron	Skin (52)	1.15 x 10^{-3}	Gray
Absorbed Dose	Photon	Skin (50)	7.05 x 10^{-4}	Gray
Absorbed Dose	Photon	Bone (51)	6.25 x 10^{-4}	Gray
Absorbed Dose	Photon	Skin (52)	5.77 x 10^{-4}	Gray
Absorbed Dose	Electron	Skin (50)	6.80 x 10^{-4}	Gray
Absorbed Dose	Electron	Bone (51)	6.25 x 10^{-4}	Gray
Absorbed Dose	Electron	Skin (52)	5.56 x 10^{-4}	Gray

The resulting total absorbed dose in each section of the hand phantom as well as the sum is given in table 2.20.

Table 2.20 – Total simulated absorbed doses

Cell	Absorbed Dose (mGy)
Skin (50)	3.03
Bone (51)	1.98
Skin (52)	2.28
Total Phantom	7.30

2.4 Discussion and Conclusions

MCNP6 was utilized to accurately model the complete NAA process, from the irradiation of an aluminum bearing sample to the detection of the resulting gamma rays produced by the activated aluminum-28. In the modeling of the neutron generation process, a more involved process was undertaken to build the anisotropy of the neutron emission into the MCNP input.

The anisotropy accounted for differences in both neutron energy as well as emission probability at different angles. The anisotropy method was compared to a simplified isotropic emission method in an experiment conducted in our laboratory that involved the irradiation of gold foils at three different locations and orientations. A comparison of the two methods found that the anisotropic simulation closely matched the relative amounts of activation determined from the actual experiment. The isotropic simulation was not able to match the relative activation measured experimentally. An isotropic simulation would be acceptable to use when irradiating relatively small samples, close to the zero-degree direction of neutron emission, or when performing NAA for identification purposes. For situations involving relatively large samples or when attempting accurate quantification of the material under analysis, accuracy demands the incorporation of an anisotropic neutron source in the simulation. Additionally, for tasks such as optimizing moderator and reflector materials via simulation, an anisotropic source should be specified as these tasks are highly dependent on neutron energy and angle of emission.

Utilizing the anisotropic source specification, the neutron irradiation of three quantities of aluminum were simulated. These quantities were matched by physical phantoms that were produced, irradiated, and analyzed by the system. Results demonstrated that the differences in acquired counts from the experimentally determined measurements and the simulated counts varied between 9.54% and 23.10%. Both simulation and physical measurement demonstrated linear responses with increases in analyte mass. This showed the relative accuracy of the developed simulation for absolute quantification of aluminum with the system. One would not have expected the simulation to match experiment exactly as a couple of factors were not accurately accounted for. To be as near to actual values as the results were speaks to the power of this simulation technique, especially if utilized for tasks such as experimental design and making estimates of conditions and capabilities. To move the simulation towards being more completely quantitative, a couple of additional steps need to be taken. First, a better understanding of where on the target neutrons are generated should be incorporated into the simulation input. The titanium target has radius of approximately 2.22 centimeters and deuterons probably interact with a relatively large portion of its area to produce neutrons. In the simulation, while the neutrons were produced anisotropically, they were done so from a point in the middle of the target. Determining the portion of the target involved in neutron production and revising the source definition to take that into account should improve accuracy. A far

greater improvement in absolute quantification would result from a better estimate of the total neutron flux during the irradiation. For these calculations, a constant neutron production was assumed during the irradiation period. In reality, there are variations in neutron production during an irradiation. The assumed neutron production was applied to the simulated results and differences between it and the actual neutron production during the experiment would result in differences between the two results. This is most likely the source of most of the error between simulation and experiment as all other variables such as source mass, geometry, and composition were carefully controlled. Improvement in the estimation of neutron production could be made by irradiating an activation foil along with the analyte sample. Assessment of the amount of activation in the foil could be used to estimate the total flux the analyte was exposed to. The estimated actual flux could be applied to the simulation results rather than simply assuming a constant flux during the irradiation.

A physical measurement of a calibration curve for the system was developed by irradiating and measuring a series of aluminum containing water phantoms. The phantoms contained three different quantities of aluminum and a set of water blanks were irradiated and analyzed as well. The calibration curve that was generated demonstrated an excellent linear response with an R-squared value of 0.9956. The background aluminum level of the water blanks averaged 19.67 counts. The background level was used to set the detection level of 26.9 counts, using the Poisson-based detection level described by Alvarez. Applying the detection level of 26.9 counts to the calibration curve determined for the system resulted in a value of 0.73 milligrams of aluminum. This represents the minimum amount of aluminum that can confidently quantified by the system.

The DD-109M MNCP6 input can and was utilized to estimate radiation doses received by exposure to the neutron generator. This is an extremely powerful and useful application as radiation doses must be understood when setting up irradiations involving human subjects. Doses must be maintained to levels acceptable to regulators and entities sanctioning research. Direct measurements of neutron radiation doses are difficult as the various interactions that mediate measurement are highly energy dependent. In an environment with significant amounts of moderating and reflecting material, the neutrons present will have a wide spectrum of energies, thereby highly altering the interaction probabilities. Accurate simulation of radiation doses provides a method for both estimating doses and providing a comparison mechanism for

any direct measurements performed. Additionally, simulation allows the individual performing it to select the units to be evaluated. Simulated doses can be performed to analyze the absorbed dose, equivalent dose, or the effective dose, as desired. This allows comparison with any limits or constraints that may be placed upon an experiment. It also allows evaluation of doses should the benchmark be changed, such as computing effective dose with the tissue weighting factors specified in ICRP 60 or the revised tissue weighting factors specified in ICRP 103.

The total neutron equivalent dose to the hand phantom for a typical activation experiment involving 360 seconds of irradiation time at a yield of 1×10^{9} neutrons per second was found to be 5.06×10^{-2} sievert. The effective dose can be calculated from the equivalent dose through the application of tissue weighting factors. For a situation involving the irradiation of a hand, the applicable tissue weighting factors would be the bone surfaces and the skin. The bone surfaces would be appropriate as opposed to using the tissue weighting factor for the bone marrow as the hand does not contain significant amounts of bone marrow. The concepts of effective dose equivalent and tissue weighting factors were initially introduced with ICRP Report 26 in 1977. The U.S. Nuclear Regulatory Commission adopted ICRP Report 26 into its regulations and title 10 of the Code of Federal Regulations still retains effective dose equivalent and the tissue weighting factors from ICRP 26. In Report 60, the ICRP revised their radiation protection scheme and dose equivalent was renamed equivalent dose. The change resulted in effective dose equivalent being renamed as effective dose. In addition, the tissue weighting factors were given for an increased number of organs and the numerical values were changed for most organs. Subsequently, in Report 103, the ICRP added tissue weighting factors for several previously unspecified organs and further revised the numerical values as more information had become available concerning radiation detriment. The tissue weighting factors given for skin and bone surfaces by Report 103 are 0.01 and 0.01, respectively. Multiplying the tissue weighting factors by the neutron dose equivalents tallied for each section of the phantom, an effective dose of 5.0603×10^{-4} sievert is arrived at. This effective dose can be compared to the whole body dose limit of 3 rems specified by the Food and Drug Administration (FDA) for research subjects undergoing radioactive drug research [87]. While technically not a process involving radioactive drug research, most research institutions use this as a limit for any research involving the exposure of subjects to radiation. Three rem is equivalent to 3×10^{-2} sievert, meaning this irradiation would result in less than 2% of the annual dose limit from neutron exposure.

The simulation of radiation dose provides a flexible method for computing whichever dose metric is desired. As noted, the tissue weighting factors have changed over time and it should be expected that they will change more in the future as data concerning radiation detriment continues to evolve. Additionally, the radiation weighting factors used to convert absorbed dose to equivalent dose are given different numerical values by different technical bodies and regulatory authorities. Originally, the ICRP in Publication 21 named radiation weighting factors as quality factors and their values were computed by a description given by the ICRU in Report 19. The NCRP also specified numerical values of the quality factors as a function of neutron energy in Report 38. The NCRP 38 quality factor values differed slightly from those given by the ICRP. The U.S. Nuclear Regulatory Commission adopted the quality factors from Report 38 and they are still codified as such in Title 10 of the Code of Federal Regulations, Part 20. With ICRP 60, the term quality factor was renamed to radiation weighting factor. Additionally, the number of neutron radiation weighting factors was reduced to five energy ranges. Those five energy ranges and their respective radiation weighting factors were utilized in this work in the computation of equivalent dose. It is worth pointing out that the radiation weighting factors specified in ICRP 60 are greater in value than those specified in NCRP 38. For example, in the energy range of 0.1 MeV to 2 MeV, the radiation weighting factor is 20 while in the same range, the quality factor never exceeds 11. This results in the equivalent dose computed by this work being higher than what would be computed using the USNRC quality factors. The power of this simulation technique though is that the tallies previously described could easily be rebinned and the tally multipliers adjusted to compute for whichever dose metric is desired. This technique results in a very robust way to estimate radiation doses, no matter the task or the goal.

CHAPTER 3. MCNP SIMULATION OF HPGE SYSTEM

3.1 Introduction

A wide variety of materials have been developed and employed over the past 120 years to detect photon radiations, including gases, scintillators, and semiconductors. Historically, much NAA has utilized scintillation detectors, usually sodium iodide activated with thallium, to detect and perform spectroscopy of the radiations emitted from activated atoms. A smaller amount of NAA projects have utilized semiconductor detectors for those purposes. This NAA project paired a transportable tabletop neutron generator as a neutron source with a semiconductor detector for the analysis portion. The semiconductor detector utilized was high purity germanium (HPGe).

HPGe detectors are a type of semiconductor radiation detector. Solid-state materials can be classified by the separation distance between the energy bands of their atomic electrons. The energy bands represent electrons that are bound in the material and those that can move through the material. The low energy, bound band is known as the valence band. The higher energy band, representing electrons that may move through the material is the conduction band. Separating the valence and conduction bands is the bandgap, which represents energy levels that electrons will not be found in a pure crystal. The classification of solid-state materials is according to the magnitude of the bandgap between the valence and conduction bands. Materials classified as conductors have very little separation or energy difference between the valence and conduction bands. This means it takes the addition of very little energy to promote electrons to the conduction band, where they may move through the material. Materials classified as insulators have a large separation or energy difference between the valence and conduction bands. This means that it would take the addition of a significant amount of energy to promote electrons to the valence band where they would be able to move through the material. Semiconductor materials have a separation between the valence and conduction bands that is greater than that of a conductor but less than that of an insulator.

Two semiconducting materials are typically utilized for radiation detectors: germanium and silicon. Germanium has a separation of 0.665 eV between its conduction and valence bands at 300 kelvin. It is not possible to have a crystalline material completely composed of a single

element as impurities will always be incorporated. Impurity atoms will necessarily alter the energy and electrical properties of the semiconducting material as they introduce additional energy states that fall between the valence and conduction bands. To restrict the effect of unwanted impurities, techniques have been developed to limit their levels far below those in natural germanium crystalline material. If such techniques have been employed, the impurities may be maintained to a level below 1 part in 1 x 10^{12}, and for a germanium crystal produced in this manner is referred to as high purity germanium (HPGe) [57].

To purposely alter the electrical properties of a semiconductor, a particular impurity will be added to the crystal, either during the growing process to the whole crystal, or afterwards to a specific region of the crystal. Germanium is tetravalent, so it forms covalent bonds with four adjacent germanium atoms. The impurity will alter the lattice structure of the crystal depending on the number of valence electrons it has. If the impurity is trivalent, it has three valence electrons and will form covalent bonds with three neighboring germanium atoms, leaving one of the germanium atoms unpaired. This creates a vacancy in the bonding pattern. The impurity can form a bond with an electron but since the bond is not part of the regular tetravalent bonding pattern, it will not be as strong. This binding site therefore represents an energy level just above the valence band, at a point inside the bandgap, and is known as an acceptor. Typical trivalent elements that are used as semiconductor impurities are boron, aluminum, gallium, and indium. Many of the acceptors will be bonded with electrons since the energy is very close to that of the valence band. The bonding of the electrons will result in a net excess of positive holes in the crystal and they become the majority of charge carriers. Such a semiconductor, with trivalent impurities is known as p-type. On the other hand a pentavalent impurity could be introduced to the semiconductor. The pentavalent atoms phosphorus, arsenic, and antimony are most typically utilized. Pentavalent atoms will covalently bond with the nearest four germanium atoms and still have an additional electron available. The addition of energy can easily promote the unpaired electron to the conduction band. These electrons are known as donor impurities and they represent energy levels in the bandgap as energies just below the conduction band. The electrons are the majority charge carriers in the crystal. Such a semiconductor, with pentavalent impurities is known as n-type [88, 89].

When radiation interacts with a semiconductor detector, its energy is transferred to the crystal. A portion of the energy deposited will create ionizations, where electrons are removed

from atoms in the crystal lattice. An ionization event that results in the ionization of an electron also leaves behind a positively charged hole. In germanium, an electron and positive hole pair is created for approximately every three electron-Volts of energy deposited. By applying an electrical field across the germanium, the electron-hole pairs created by the energy deposited by the radiation can be collected as they are both charged entities. The flow of charge per time is current and that is what is collected by the detector. Ultimately, the amount of current collected per radiation event is proportional to the amount of energy transferred to the germanium by the radiation.

The plotting of the energy of a detected event by the number of events having a particular energy, allows the creation of an energy spectrum. Relative to many other radiation detectors, such as gas-filled or scintillation, germanium takes very little deposited energy to create an information carrier (the electron-hole pair for a semiconductor detector). The creation of relatively large amounts of information carriers results in a limiting of the statistical fluctuations of the detection process. This in turn ensures germanium detectors have relatively good energy resolution. Energy resolution can be defined as the full width at half the maximum value (FWHM) of a photopeak, divided by the energy of the photopeak, usually expressed as a percentage:

$$Energy\ Resolution = \frac{FWHM}{Photopeak\ Energy} * 100\% \qquad \text{(Equation 43)}$$

3.2 Materials and Methods

An Ortec GEM100P4-95 (Oak Ridge, TN) high purity germanium (HPGe) detector was utilized. It is a p-type coaxial HPGe with an efficiency of 100% relative to a point source of Co-60 at 25 centimeters from the face of a standard three inch by three-inch sodium iodide detector. The manufacturer quoted FWHM of the detector at 1.33 MeV is 2.1 keV [90].

The HPGe was connected to an Ortec DSPEC-50 (Oak Ridge, TN) digital signal processing gamma spectrometer. The spectrometer was controlled using Ortec MAESTRO (Oak Ridge, TN) multichannel analyzer software, version 7.01.

3.2.1 MCNP6 Input Specification

The Ortec coaxial HPGe detector utilized in our laboratory was originally modelled in MCNP6 by Colby Neumann and is described in his M.S. Thesis [91]. The modelling was according to the dimensional specifications provided by Ortec. Colby modelled an Ortec GMX-100P4-95-A coaxial HPGe detector. It is dimensionally and materially identical to the GEM100P4-95 coaxially HPGe detector utilized in the following measurements, with the exception that it is an N-type detector with the diffused lithium on the inside of the coaxial germanium rather than the outside. Its efficiency specification is also 100% relative to a point source of Co-60 located 25 centimeters from the face of a standard three-inch by three-inch sodium iodide detector [90].

The original input was revised slightly to simplify the geometry specification of the detector and surrounding lead shielding. As part of his work, Colby adjusted the lithium dead layer of the detector to reduce the discrepancy between simulation and experimental results. While the dead layer will vary from detector to detector, no adjustment was made for this project as dead layer thickness is a more significant factor when performing spectroscopy on lower energy photons [92]. As this project was analyzing relatively high energy photons, the dead layer thickness influence is minimal. Visual Editor generated images of the HPGe detectors are displayed in figures 3.1 and 3.2. Figure 3.1 shows the exterior of the detector with some of the surrounding lead shielding and figure 3.2 demonstrates the interior detail of the detector, as specified in MNCP6.

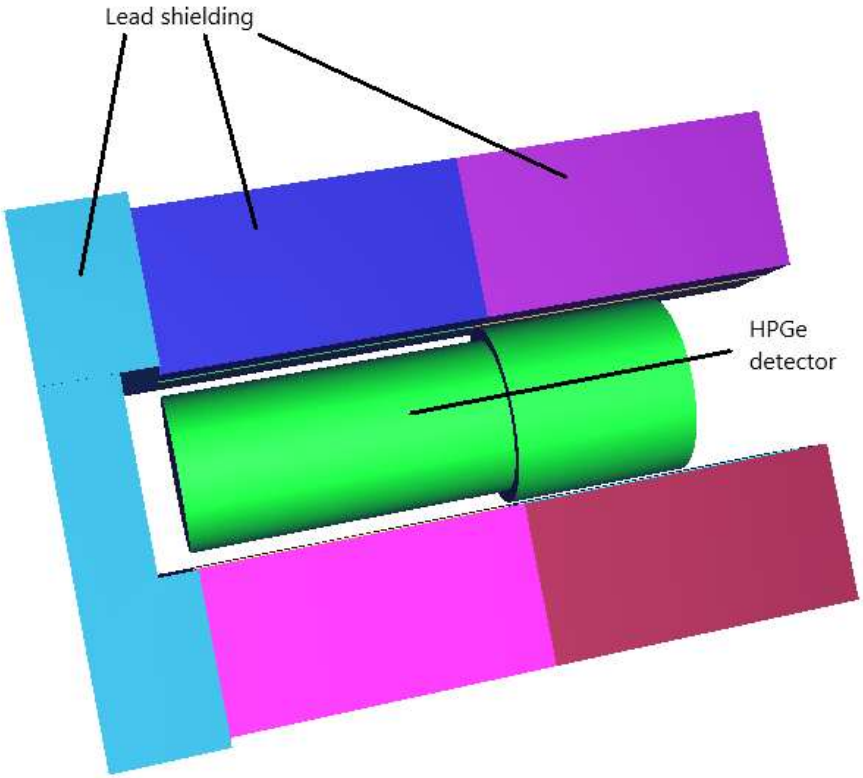

Figure 3.1 – Visual Editor image of HPGe detector and lead shielding

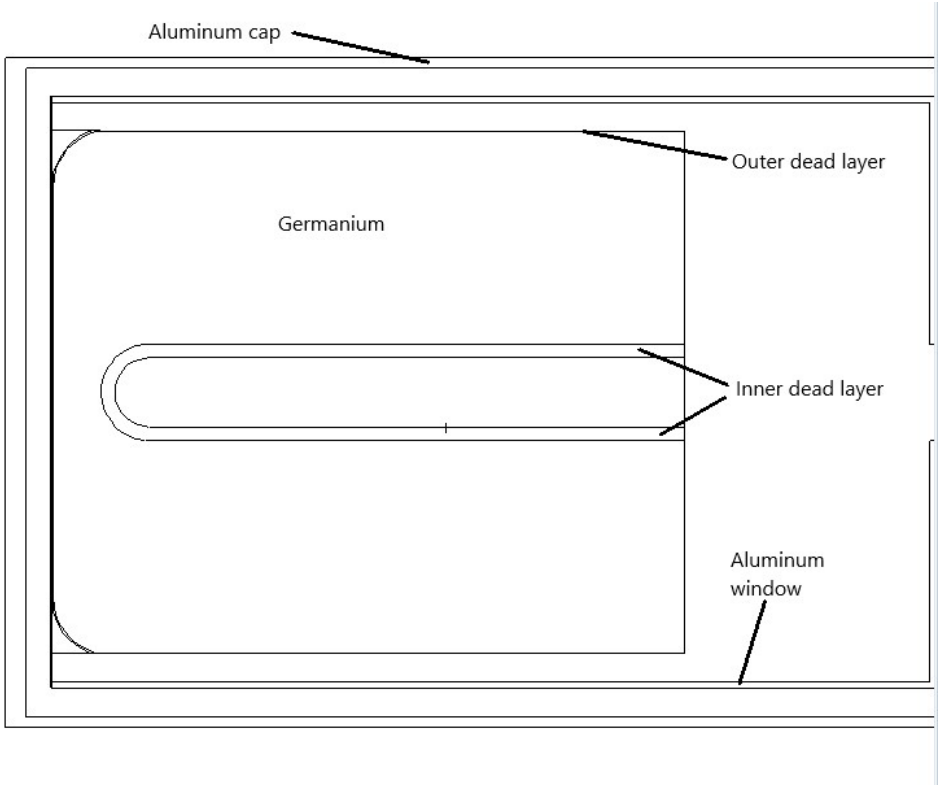

Figure 3.2 – MCNP simulation of HPGe detector

To simulate photon interactions in the germanium, an F8 tally was setup. The F8 tally records the energy distribution of pulses created by radiation in a detector and has the units of the number of pulses if the tally is simply specified "F8" [74]. The F8 tally included the energy tally card, which set up the energy bins that the tally pulses would fall into. The energy tally card had the form:

E8 0 16384i 3.26362

which divided the tally into 16,384 energy bins ranging from 0 MeV to 3.26362 MeV. Setting the tally up with that number of energy bins and over that energy meant that the output exactly matched the setup of the Maestro software controlling the HPGe detector.

Simulated photon tallies must be modified by the Gaussian Energy Broadening (GEB) special treatment, specified with the FT card, in order to approach the appearance of the actual acquired spectrum. Without this modification, simulated spectra will have photopeaks that fall

within a single energy bin, while acquired actual photopeaks demonstrate a broadening over a number of energy bins due to the statistical nature of photon detection and processing. The GEB card is specified by three parameters a, b, and c that are used to determine the full width at half-maximum of the photopeak as a function of the photon energy. The parameters a, b, and c have units of MeV, MeV^1/2, and 1/MeV, respectively. The FWHM is calculated as:

$$FWHM = a + b(E + cE^2)^{1/2} \quad \text{(Equation 44)}$$

where E is the photon energy, specified in MeV [74]. The amount of broadening is specific to a particular radiation detector and must be measured so that the parameters a, b, and c can be determined. To measure the amount of broadening, a spectrum from a radioactive source containing multiple isotopes was acquired on the GEM100P4-95 HPGe detector. The source contained cobalt-60 and yttrium-88. Cobalt-60 emits a 1,173.2 keV gamma ray in 99.85% of decays and a 1,332.5 keV in 99.98% of decays [93]. Yttrium-88 emits a gamma ray of 1,836.1 keV in 99.2% of decays [94]. Cobalt-60 and yttrium-88 were chosen because their gamma rays are close in energy to that of the 1,779.0 keV gamma ray from aluminum-28 that is to be analyzed by this system. Restricting the energy range under consideration was performed to improve the accuracy of the determined broadening parameters.

A spectrum was acquired that included the cobalt-60 and yttrium-88 photopeaks. The FWHM of the three gamma ray photopeaks was determined. This was done by first fitting a Gaussian curve to the data acquired for each photopeak using Microsoft Excel for Microsoft 365. The energy bin was plotted on the x-axis and acquired counts on the y-axis. The data was fit using the Gaussian function:

$$Y = ae^{-\frac{(x-b)^2}{2c^2}} \quad \text{(Equation 45)}$$

where x was the count data and y were the energy bins. Parameters a, b, and c represent the height, location, and FWHM of the Gaussian curve. The fit data was subtracted from the count data and squared. The squared data was then summed and the Excel solver function was used to iteratively perform a Gaussian fit of the photopeak data. This was done by providing

initial guesses to a, b, and c and using the GRG Nonlinear solving method to minimize the sum of the squared data.

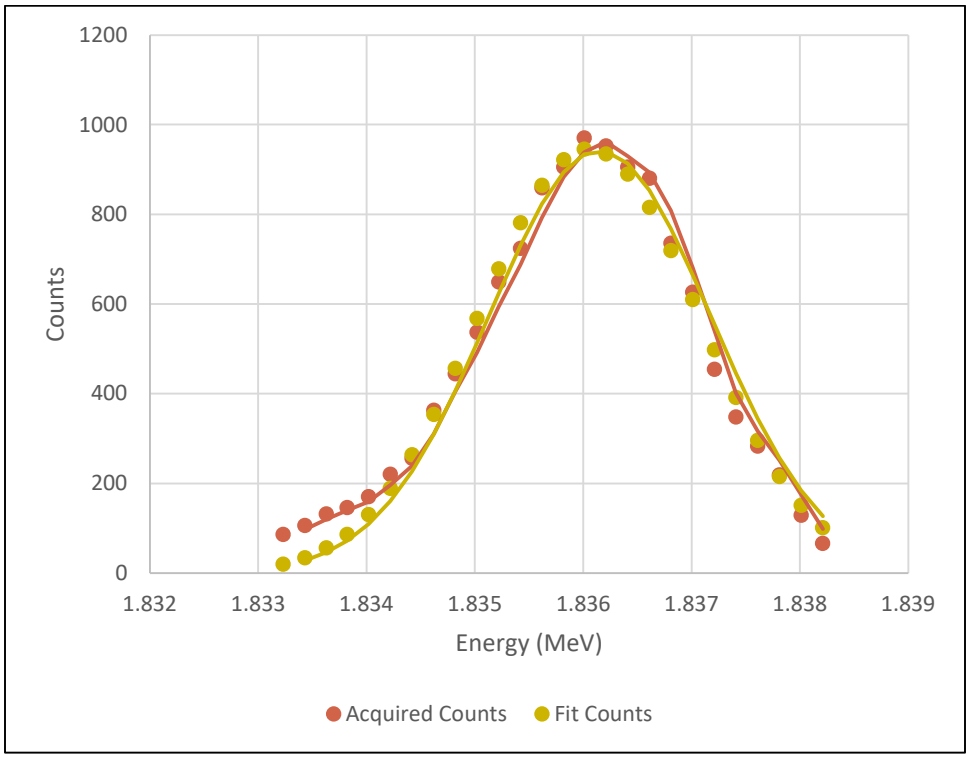

Figure 3.3 – Comparison of acquired photopeak to Gaussian fit photopeak

Following completion of the data fitting, the FWHM was calculated for the curve as:

$$\text{FWHM} = 2(2 \ln 2)^{1/2} c \qquad \text{(Equation 46)}$$

where c was taken from the fitted curve. Curve fitting and FWHM determination were made on both cobalt-60 gamma rays and the yttrium-88 gamma ray.

The gamma ray energy was plotted versus the determined FWHMs and a second order polynomial trendline was added. The equation of the trendline was displayed and it is from the trendline that the GEB coefficients taken.

Table 3.1 – Determined gamma ray FWHMs

Photon Energy (MeV)	FWHM (MeV)
1.173	0.001928
1.332	0.002021
1.836	0.002408

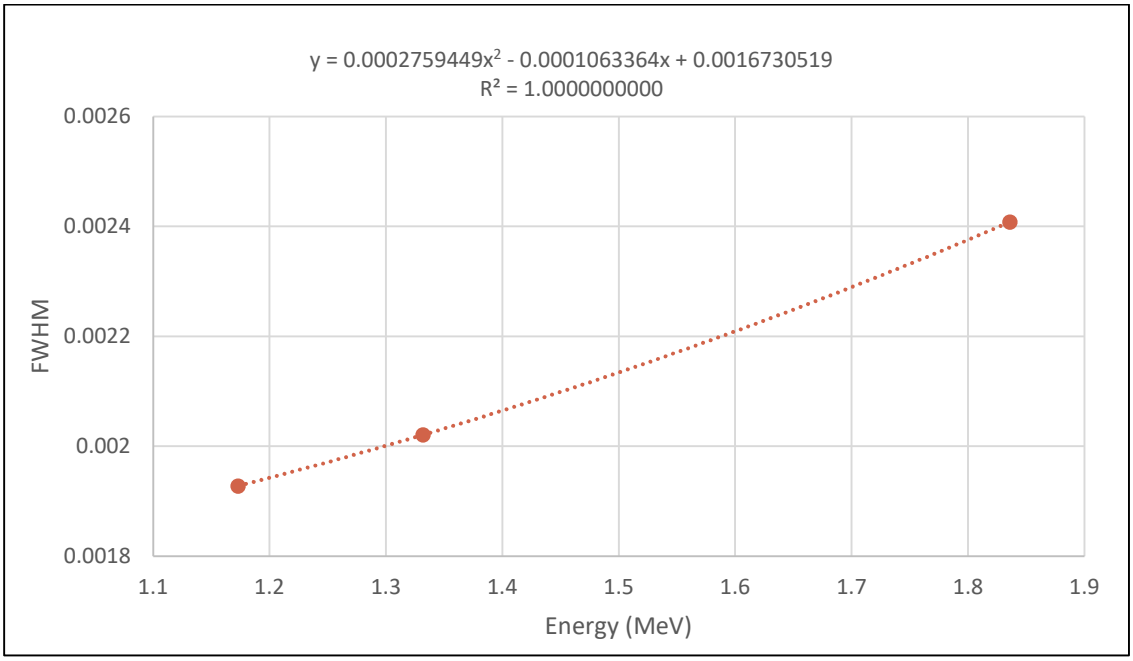

Figure 3.4 – Relationship between FWHM and photon energy

From the trendline equation, the first coefficient is equal to b, the second coefficient equal to c, and the third coefficient equal to a on the GEB card. These were programmed in to the MCNP input and resulted in a proper amount of broadening of acquired spectra. A comparison of the acquired 1,332.5 keV photopeak to the broadened simulated photopeak is displayed in Figure 3.5. Note that for the sake of comparison, the simulated data has been shifted two energy bins higher so that the peak centroids match up more evenly. It is clear from the figure that the amount of simulated broadening is similar to the actual amount of broadening detected in the system.

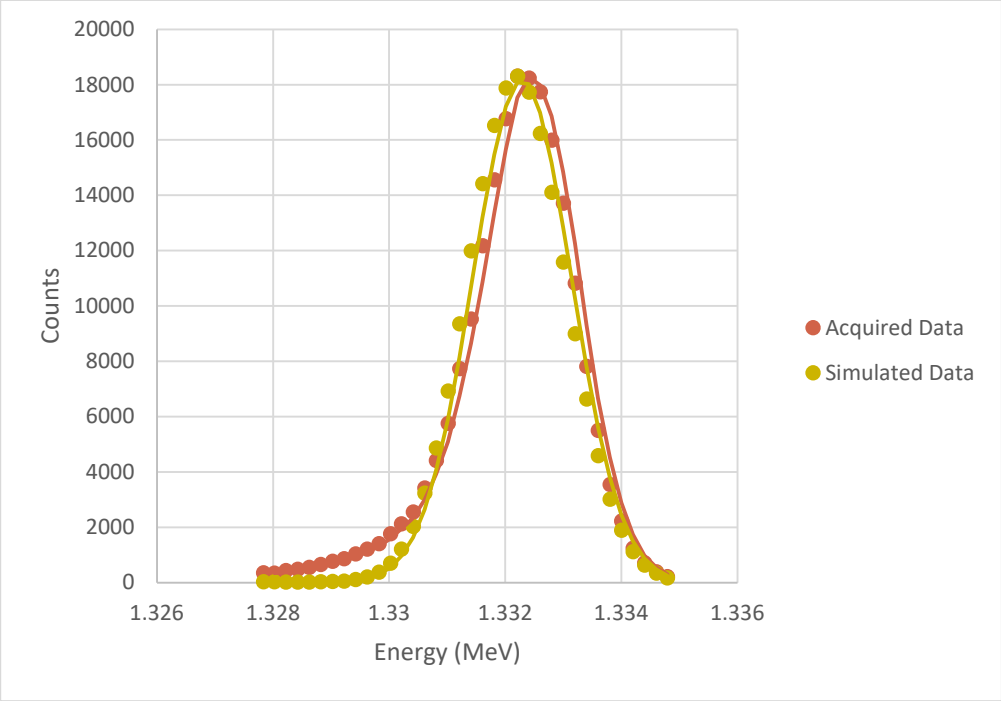

Figure 3.5 – Comparison of acquired and simulated photopeaks

3.2.2 Phantom Simulation

The cylindrical phantom previously described in section 2.2.3 was utilized in simulation of the HPGe detector response. The material in the phantom was specified as aluminum-28 at a density equal to that of the 5 milligrams activation simulation. The 5 milligrams simulation found the formation of 4.59093 x 10^{-8} atoms of Al-28 per source particle. An irradiation of 360 seconds at a yield of 1 x 10^{9} neutrons per second results in the formation of 7.523 x 10^{3} atoms of Al-28. After a transfer period of 90 seconds, 4.735 x 10^{3} atoms of Al-28 remain. This is equal to a mass of:

$$4.735x10^{3}atoms * \frac{mol}{6.022x\ \ ^{23}atoms} * \frac{28\ g}{mol} = 2.2016x10^{-1}\ \ g \qquad \text{(Equation 47)}$$

This mass value was divided by the phantom volume of 5 cm^3 to arrive at the density of aluminum-28, which was specified in the simulation input. The phantom was simulated at the face of the HPGe detector, at the location where the actual activated phantoms were placed.

A tally of type 8 was set up for the germanium containing cell of the HPGe detector. The tally was divided up into energy bins by the tally energy card. A total of 16,384 bins, ranging from 0 to 3.26362 MeV were set up by the tally energy card. These values matched the energy range and number of energy bins of the Ortec spectrometer. The tally was also modified by a special treatment for tallies card. The special treatment for tallies was the Gaussian energy broadening modification. The Gaussian energy broadening card utilized the coefficients determined in section 3.2.1 for the HPGe detector.

The HPGe detector simulation with the aluminum-28 source phantom was executed for a total of 4 x 10^8 particles. Each particle represented the decay of an aluminum-28 atom and the resulting radioactive emissions of that decay were tallied for the response of the germanium in the HPGe detector.

3.3 Results

The F8 tally resulted in an estimate of counts per energy bin. The energy bins between 1,774.28 and 1,781.25 keV, where the aluminum-28 gamma ray photopeak was located, were evaluated. The summation of these energy bin tallies was 0.034827453. This represents 0.034827453 counts in this energy range per decay of aluminum-28 and is effectively a simulated efficiency of the detector for the 1.779 MeV gamma ray. Compared to the efficiency measured for the 1.836 MeV gamma ray from yttrium-88, there was a percent difference of:

$$\frac{|x_1-x_2|}{\frac{(x_1+x_2)}{2}} * 100 = \frac{|0.034827453- \ .024641686|}{\frac{(0.034827453+0.024641686)}{2}} * 100 = 34.3\% \qquad \text{(Equation 48)}$$

Further comparing the simulated photopeak to the actually acquired 5 milligrams aluminum sample, shows a close correlation of the two. The total counts detected in the 5 milligrams acquired phantoms averaged to 193 counts in the aluminum-28 photopeak. The background acquired phantoms averaged 0.787 counts per channel in the aluminum-28 energy photopeak range. Subtracting the background counts from the 5 milligrams aluminum phantom

average results in a total of 165.445 counts in the photopeak. Applying the measured efficiency factor of 0.024641686, means that there were 6714.435 atoms of aluminum-28 that decayed during the measurement period. Each channel of the F8 tally for the simulated spectrum represented the number of counts per decay of aluminum-28. By multiplying each channel by a value of 6714.435 decays, a total simulated spectrum for a ten-minute count of an irradiated 5 milligrams aluminum phantom was obtained. The total number of counts in the aluminum-28 gamma ray photopeak in the simulated spectrum was 234, compared to 194 counts in the real spectrum. The percent difference between the real and simulated photopeaks was 18.7%. The real and simulated photopeaks are displayed in overlay fashion in figure 3.6.

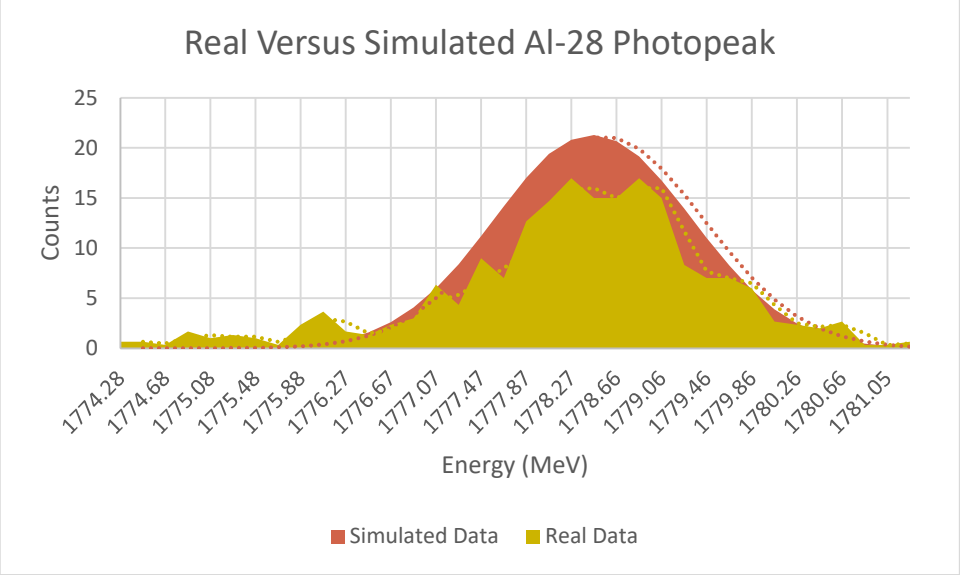

Figure 3.6 – Comparison of acquired and simulated Al-28 photopeak

3.4 Discussion and Conclusions

An HPGe detector was fully simulated in MCNP6. The dimensions and materials of the detector were included as were, importantly, an empirically determined quantification of its Gaussian Energy Broadening (GEB) response. Not including GEB in the MCNP6 input would still allow for simulation of absolute detector response, such as the number of pulses at a given energy. The response would of course have an unrealistic appearance as an individual photon energy would fall completely in a single energy bin. Including GEB allows for the simulated spectra to have appearances representative of real-world results. While this project focused on

relatively high energy gamma ray from aluminum-28 that occur in parts of the energy spectrum where there is essentially no background and limited interfering photons, the accuracy of this simulation technique was proven. In parts of the energy spectrum lower in energy or in situations where potentially interfering photons may be present, the ability to accurately simulate the photopeak, including the energy resolution could be important to determining detection abilities.

The simulation was also used to estimate the detection efficiency of the HPGe detector for the 1.779 MeV gamma ray. This was compared to the detector efficiency measured for a similar photopeak, that of the 1.836 MeV gamma ray from yttrium-88. The percent difference between the simulated and measured efficiencies was 34.3%. While the percent difference is relatively large, the actual efficiency values are quite small and thereby sensitive to subtle errors in either measurement or simulation. Additionally, the efficiency measurement included detector deadtime, while the simulation did not. Deadtime lowers the measured efficiency, meaning the measurement value would have been closer to the simulated value had deadtime not been present. With the percent difference being within an order of magnitude, the simulation technique is demonstrated to be accurate for providing estimates of detector efficiency. This would be especially useful in situations where an experiment or measurement is being planned and there is no calibrated source available to measure the efficiency. The vast majority of radionuclides have half-lives that preclude the production and availability of calibration sources for measuring detector efficiency. For them, it is possible to at least estimate detector efficiency using MCNP6, in a manner that was performed here. Perhaps more useful is the ability to estimate efficiencies for a variety of source geometries. In this work, we were able to compare a calibration source that closely resembled the activation phantom being measured. In real life, calibration sources are infrequently similar dimensionally to the object being counted. Geometry affects efficiency greatly so any deviations between calibration source geometry and the object being measured will result in measurement error. By being able to accurately simulate a source's efficiency, estimates can be made in situations where the source may have a large volume or an unusual shape. Simulation could be used to not only develop an estimate of detector efficiency but also other detection parameters such as the amount of time to count for to obtain a set level of statistical certainty. Thus, an experimenter can use a simulation to setup experiment parameters and also understand where potential errors may arise.

CHAPTER 4. ANALYSIS OF HUMAN IRRADIATION DATA

4.1 Introduction

An NAA human research study was performed in Zunyi, China to analyze the amount of skeletal manganese present in a group of 61 workers. The study was approved by the Purdue University Institutional Review Board as well as the Zunyi Medical College Ethical Review Board. A total of 61 workers were included in the study, 31 from a ferroalloy factory and 30 from a manufacturing facility. The 31 workers at the ferroalloy factory were occupationally exposed to manganese while the 30 from the manufacturing facility were considered to be a manganese control group. The goal of the study was primarily to analyze manganese exposure and the potential exposure to aluminum was not considered when dividing the workers into the two groups [95, 96].

4.2 Materials and Methods

Workers in the control and exposed groups underwent several different analyses, including NAA, assessment of metals content in drawn whole blood, and mass spectrometry of fingernail samples. The NAA portion of the assessment was performed with the Adelphi DD-108M neutron generator. Subjects had a hand irradiated for a period of ten minutes with the generator operated at 110 kV. Following the irradiation, a five-minute transfer period was observed and then the closed hand was counted with a GMX100P4-95 HPGe detector. Three count periods were acquired on most of the workers: the first five minutes after the transfer period, the first 30 minutes after the transfer period, and the first 60 minutes after the transfer period [95]. Mass spectrometry of fingernail samples was performed by having subjects wash their hands with soap and water and then clip nails from all ten digits using a titanium dioxide clipper. Nail clippings were twice cleaned in an ultrasonic water bath with 1% Triton X-100 (Sigma-Aldrich, Inc.) and rinsed with deionized water. Once clean, they were digested in ultrapure nitric acid (Sigma-Aldrich, Inc) and analyzed via inductively coupled plasma-mass spectrometry at the Campus-Wide Mass Spectrometry Center at Purdue University utilizing a Thermo Fisher ELEMENT 2 (ThermoFinnigan/FinniganMAT) [96].

The NAA parameters of the study were set to optimize the detection of manganese and not aluminum. The mass spectrometry analysis was for fingernail aluminum, providing a potential basis for correlation with the NAA results. The NAA data was reviewed to determine if positive detection was possible and if there was any correlation with the mass spectrometry data.

4.3 Results

The 61 workers studied did not all result in useful data. NAA performed on the first 17 workers was done so with the detection system too close to the generator, resulting in non-usable data. A further five workers did not have NAA performed and two additional workers did not have data saved for the first five minutes after the transfer period. This left 13 workers from the control group and 24 workers from the exposed group that had both mass spectroscopy and five-minute count NAA results. The results of the mass spectroscopy are presented in table 4.1.

Table 4.1 – Mass spectrometry determined fingernail aluminum concentrations

Worker Number (Group)	Micrograms Al per Gram of Fingernail (μg/g)
18 (Control)	11
19 (Control)	57
20 (Control)	137
21 (Control)	134
22 (Control)	26
23 (Control)	161
24 (Control)	35
25 (Control)	68
26 (Control)	66
27 (Control)	24
28 (Control)	19
29 (Control)	15
30 (Control)	9
38 (Exposed)	197
39 (Exposed)	51
40 (Exposed)	211
41 (Exposed)	144
42 (Exposed)	214
43 (Exposed)	39
44 (Exposed)	54
45 (Exposed)	35
46 (Exposed)	12
47 (Exposed)	48
48 (Exposed)	123
49 (Exposed)	52
50 (Exposed)	41
51 (Exposed)	16
52 (Exposed)	29
53 (Exposed)	30
54 (Exposed)	92
55 (Exposed)	32
56 (Exposed)	25
57 (Exposed)	159
58 (Exposed)	15
59 (Exposed)	7
60 (Exposed)	25
61 (Exposed)	16

Analysis of the gamma ray spectra was performed by summing the acquired counts in the aluminum-28 photopeak, falling between 1,777.093 MeV and 1.779.906 MeV from the first five-minute count. The photopeak was composed of a total of 15 energy bins. To subtract background from the photopeak, an area of 15 energy bins just below the photopeak, ranging from 1,772.071 MeV to 1,774.883 MeV was summed and averaged with an area of 15 energy bins just above the photopeak, ranging from 1,782.115 MeV to 1,784.928 MeV. The total acquired counts for each of the workers is presented in table 4.2.

Table 4.2 – Aluminum-28 photopeak counts

Worker Number (Group)	Gross Photopeak Counts	Background Average	Net Photopeak Counts
18 (Control)	4	7	0
19 (Control)	6	5	1
20 (Control)	5	5	0
21 (Control)	4	7	0
22 (Control)	6	5	1
23 (Control)	5	7	0
24 (Control)	2	6	0
25 (Control)	7	3	4
26 (Control)	9	9	0
27 (Control)	12	7	5
28 (Control)	4	3	1
29 (Control)	2	6	0
30 (Control)	4	5	0
38 (Exposed)	3	9	0
39 (Exposed)	3	4	0
40 (Exposed)	5	3	2
41 (Exposed)	3	8	0
42 (Exposed)	4	4	0
43 (Exposed)	3	4	0
44 (Exposed)	3	4	0
45 (Exposed)	8	5	3
46 (Exposed)	6	3	3
47 (Exposed)	3	6	0
48 (Exposed)	6	5	1
49 (Exposed)	1	6	0
50 (Exposed)	5	4	1
51 (Exposed)	6	6	0
52 (Exposed)	4	4	0
53 (Exposed)	4	4	0
54 (Exposed)	5	6	0
55 (Exposed)	4	6	0
56 (Exposed)	5	7	0
57 (Exposed)	2	7	0
58 (Exposed)	5	3	2
59 (Exposed)	5	6	0
60 (Exposed)	4	5	0
61 (Exposed)	1	4	0

As shown in table 4.2, no worker demonstrated significant photopeak counts above background. The greatest number of net counts observed was five for worker 27 and this value

fell within the fluctuation of background counts, which ranged between three and nine. No correlation could be made between the mass spectrometry determined aluminum concentrations and the number of net photopeak counts measured with NAA.

4.3.1 DD-108M Detection Limit for Suboptimal Aluminum Analysis

The NAA performed in the Zunyi research study was optimized for the analysis of manganese and not aluminum. The production of manganese-56 by neutron bombardment of manganese-55, yields a product that has a much longer half-life (2.58 hours) than that of aluminum-28. Due to the longer half-life, transfer times between irradiation and detection can be increased without loss of significant signal. In the case of aluminum-28, any time transferring between irradiation and detection will result in significant signal loss, thereby reducing detectability. As the Zunyi experiment was not optimized for aluminum detection, an evaluation of how the detection limit was affected must be conducted to determine if it were feasible to detect in vivo aluminum at levels that could be expected in humans. The detection limit can be evaluated by simulating the activation of aluminum in a human hand under the irradiation conditions of the Zunyi experiment and then simulating the expected HPGe detection efficiency of activated aluminum-28 in the hand.

4.3.1.1 DD-108M Activation of Aluminum in a Human Hand

The simulation of the activation of aluminum present in bone contained within the human hand was performed using the MCNP input of the DD-108M generator described in section 2.2.1. The human hand phantom, with a bone mass of 70 g, was simulated in the irradiation cavity of the generator. To the hand bone was added aluminum, replacing calcium, at three different quantities: 6.0375 milligrams, 12.075 milligrams, and 25.478 milligrams. An F4 tally was developed to determine the amount of production of aluminum-28 per source particle (neutron) in the bone of the phantom. The tally had the form:

```
F4:n 16
FM4 c 208 102
```

where the hand bone was contained in cell 16, c was a multiplicative constant for the amount of aluminum, 208 was the material specification for aluminum, and 102 is the ENDF number for the neutron, gamma reaction. The multiplicative constant was determined for each quantity of aluminum as follows:

$$c = \frac{6.022043446928 \quad {}^{23}atoms}{mol} * \frac{mol}{26.981538\ g} * \frac{1x10^{-24}cm^2}{barn} * \ 0.0060375\ g \qquad \text{(Equation 49)}$$

$$= 0.000134751$$

Each aluminum-bearing hand phantom was simulated in the DD-108M until the tally variance was less than 0.01, a value considered to be valid. The results of the simulations are presented in table 4.3.

Table 4.3 – MCNP simulated aluminum-28 activation

Aluminum Mass (mg)	Al-28 Produced per Source Particle
25	8.39552×10^{-8}
12.075	4.05503×10^{-8}
6.0375	2.14085×10^{-8}

The simulated production of aluminum-28 is presented in figure 4.1. From the trendline of the graph, we have a linear relationship between simulated activation and aluminum concentration in the hand bone.

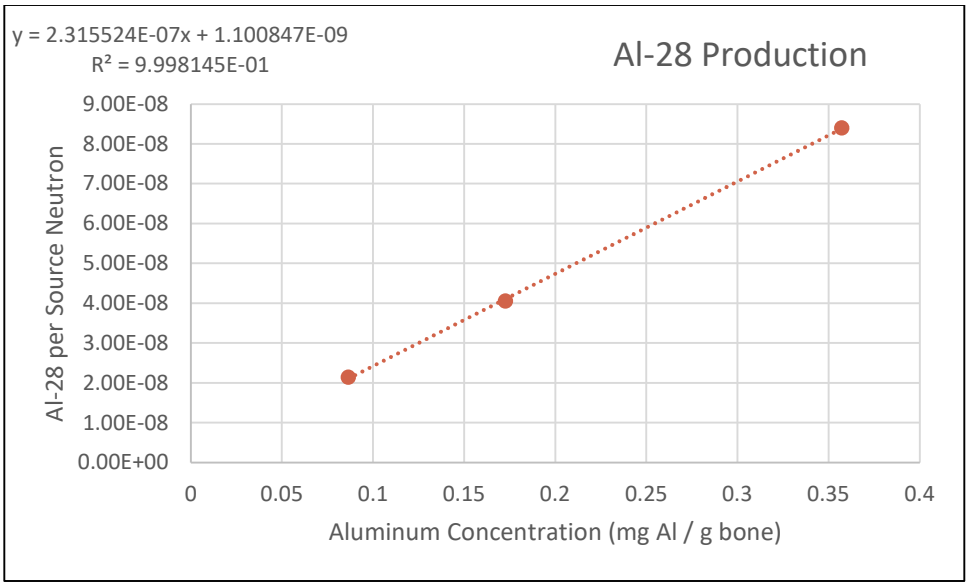

Figure 4.1 – DD-108M relationship between simulated activation and aluminum concentration

4.3.1.2 Simulation of HPGe Efficiency for Aluminum-28 in a Human Hand

The simulation of the efficiency of the HPGe detector system for aluminum-28 contained in a hand was performed using the HPGe detector input described in section 3.2.1. At the face of the detector was simulated a closed hand, in the geometry used for human subject counting. The hand specification was the same from an elemental, volume, and density standpoint as previously described. Dimensionally, the hand was altered to be 3 centimeters x 3.62612 centimeters x 6 centimeters. In the hand bone, in place of a small quantity of calcium, was inserted the equivalent of 25.478 milligrams of aluminum-28. An F8 tally, as described in section 3.2.2 was setup to simulate the 1.779 MeV photopeak arising from the decay of the aluminum-28 in the human hand. The number of counts in the photopeak per decay of aluminum-28 was integrated to yield a photopeak efficiency for the counting geometry. The determined efficiency was 0.0229605, which can be compared to the aluminum efficiency of section 3.3 of 0.034827453. A lower efficiency is expected for the hand phantom as its volume is greater and the coverage by the HPGe detector is reduced relative to a smaller 5 cm^3 phantom.

4.3.1.3 Calculated Zunyi Experiment Detection Limit

The background counts around the 1.779 MeV gamma ray photopeak from the Zunyi experiment was approximately 5, for an equal number of energy bins. For a background of this

magnitude, the Poisson-based detection limit of Alvarez, described in section 1.3.2.2 requires the accumulation of 17.1 counts for a positive detection of aluminum. Assuming a detection efficiency of 0.0229605 as determined by the MCNP simulation, there would have to be 744.75 aluminum decays during the count period. The number of aluminum-28 atoms that we must start with at the beginning of the count period to experience 744.75 decays can be calculated by:

$$A_o\left[1 - e^{-\lambda t}\right] = 744.75 \qquad \text{(Equation 50)}$$

where λ is equal to 0.005145 per second for aluminum-28 and t is equal to the count time period of 300 seconds. Solving the equation for A_o gives a result of 947.09 atoms of aluminum-28 to begin the count period. The count period began after a 300 second transfer period, post irradiation. The number of aluminum-28 atoms that must be generated at the end of the irradiation and start of the transfer period in order to begin the count period with 947.09, can be calculated by:

$$A_o e^{-\lambda t} = 947.09 \qquad \text{(Equation 51)}$$

where λ is equal to 0.005145 per second for aluminum-28 and t is equal to the length of the transfer period of 300 seconds. Solving the equation for A_o gives a result of 4,433.25 atoms of aluminum-28 at the conclusion of the irradiation.

The decay of aluminum-28 during the irradiation requires more than 4,433.25 atoms at the irradiation conclusion. We can calculate the necessary amount of aluminum-28 by:

$$Activity = N\sigma\phi\left[1 - e^{-\lambda t_i}\right] \quad \text{(Equation 52)}$$

where N is the number of atoms of a particular isotope in the sample, σ is the cross section for a neutron capture reaction involving the isotope, φ is the neutron flux, λ is the physical decay constant of aluminum-28, and t is the irradiation time of 600 seconds. In order to have 4,433.25 atoms of aluminum-28 at the end of the irradiation, we must have 4,645.26 atoms of aluminum present at the beginning.

The MCNP Al-28 activation tally returns a saturated activity value and based on the length of the irradiation period, it must be determined what fraction of the saturated activity has been produced. This can be determined with the relationships:

$$Activation\ Yield = \frac{A_t}{Saturation\ Activity} = \left[1 - e^{-\lambda}\right] \qquad \text{(Equation 53)}$$

$$Activation\ Yield = \frac{Saturation\ Activity}{\tau} \qquad \text{(Equation 54)}$$

$$Saturation\ Activity = \tau * \left[1 - e^{-\lambda t}\right] \qquad \text{(Equation 55)}$$

$$Saturation\ Activity = 194.37\ s * \left[1 - e^{-0.005145 s^{-1} * 600}\right]$$

$$= 185.39 \text{ seconds}$$

where τ is equal to the inverse of the decay constant of aluminum-28, λ is the decay constant of aluminum-28, and t is the irradiation time. The calculated saturation activity is determined in time units and is relative to the theoretical saturation time. The saturated activity is then multiplied by the generator neutron yield to give the number of number of neutrons contributing to the activation tally:

$$185.49\ s * 7.8x10^{8}\ \frac{n}{s} = 1.30x10^{11}\ n$$

The requisite number of atoms of aluminum-28 can be divided by the number of neutrons contributing to the activation tally, resulting in a value of 3.5775 x 10^{-8} atoms of Al-28 per neutron. This value can be inserted into the equation of the line of the simulation Al-28

production, figure 4.1, to determine the minimum detectable bone aluminum concentration for the Zunyi study experimental parameters:

$$y = 2.315524\ x\ 10^{-7} * x - 1.100847\ x\ 10^{-9} \qquad \text{(Equation 56)}$$

$$3.5775\ x\ 10^{-8} = 2.315524\ x\ 10^{-7} * x - 1.100847\ x\ 10^{-9}$$

$$x = 1.59\ x\ 10^{2}\ micrograms\ Al\ per\ gram\ bone$$

4.3.2 DD-108M Optimized Detection Limit for Aluminum Analysis

Based on the neutron yield of the DD-108M generator and the measured aluminum-28 photopeak background signal of 5 counts, the detection limit can be estimated for a more optimized set of experimental parameters. A confident detection of Al-28 with a background of 5 counts in the photopeak, requires the detection of 17.1 counts. Assuming a detection efficiency of 0.0229605 for the HPGe detector, it takes 755.76 Al-26 decays to obtain a positive detection. There are three variable experimental factors that effect the detection limit: 1. irradiation time, 2. transfer time, and 3. counting time. Optimization of detection limit, that is, getting the detection limit as low as possible so as to detect the smallest quantity of aluminum, is improved by utilizing the longest irradiation and count times while minimizing the transfer time. An upper limit is placed on irradiation time by the radiation dose to the subject, which is linear with time while the amount of activated aluminum plateaus as saturated is achieved. Counting time is limited by subject comfort and the need to free up equipment and is also marked by diminishing returns as the number of acquired counts exponential reduces as the count period progresses. The longest irradiation period that would be useful would be 600 seconds, which would allow the production of 95.44% of Al-28. A minimum transfer period of 15 seconds would be needed for the research subject to move from the neutron generator to the HPGe detector. The longest count period that would be useful would be 600 seconds, which would allow the recovery of 95.44% of counts. Based on these experimental parameters and utilizing the equations described in Section 4.3.1.3, the detection limit for Al-28 in a human hand for the DD-108M neutron generator operating at a neutron yield of 7 x 10^8 neutrons per second would be 3.41 x 10^1

micrograms of aluminum per gram of bone. Shortening the irradiation and/or counting times would increase the detection limit, as demonstrated in tables 4.4 and 4.5. Additionally, lengthening the transfer period would also increase the detection limit, as demonstrated in table 4.6.

Table 4.4 – Irradiation time effect on detection limit (15 s transfer, 600 s count)

Irradiation Time (seconds)	Detection Limit (mg Al / g bone)
120	1.31×10^{-1}
180	7.81×10^{-2}
240	5.80×10^{-2}
300	4.80×10^{-2}
360	4.24×10^{-2}
420	3.89×10^{-2}
480	3.67×10^{-2}
540	3.52×10^{-2}
600	3.41×10^{-2}

Table 4.5 – Count time effect on detection limit (600 s irradiation, 15 s transfer)

Count Time (seconds)	Detection Limit (mg Al / g bone)
120	6.56×10^{-2}
180	5.12×10^{-2}
240	4.43×10^{-2}
300	4.04×10^{-2}
360	3.80×10^{-2}
420	3.64×10^{-2}
480	3.54×10^{-2}
540	3.47×10^{-2}
600	3.41×10^{-2}

Table 4.6 – Transfer time effect on detection limit (600 s irradiation, 600 s count)

Transfer Time (seconds)	Detection Limit (mg Al / g bone)
15	3.41×10^{-2}
30	3.65×10^{-2}
45	3.90×10^{-2}
60	4.18×10^{-2}
75	4.48×10^{-2}
90	4.80×10^{-2}
105	5.14×10^{-2}
120	5.52×10^{-2}
135	5.92×10^{-2}
300	1.32×10^{-1}
360	1.78×10^{-1}
600	6.01×10^{-1}

4.3.3 DD-109M Optimized Detection Limit for Aluminum Analysis

Experimental parameters such as irradiation time, transfer time, and count time affect the DD-109M in a similar manner as the DD-108M. However, the generators create different neutron yields and have different moderator configurations, both of which will affect activation production. Due to activation differences, the detection limits of the DD-108M and DD-109M will not be equivalent. A comparison is made here between the two neutron generators.

The aluminum-containing human hand phantom was simulated on the DD-109M with the same quantities of aluminum as described in Section 4.3.3.1. The activation results are displayed in Table 4.7.

Table 4.7 – MCNP simulated aluminum-28 activation

Aluminum Mass (mg)	Al-28 Produced per Source Particle
25	5.09993×10^{-8}
12.075	2.46326×10^{-8}
6.0375	1.29907×10^{-8}

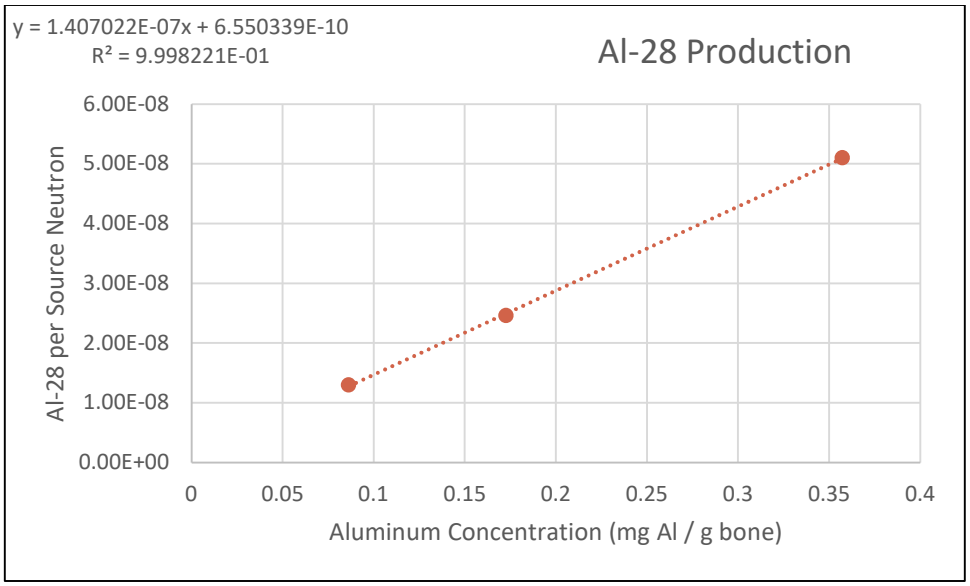

Figure 5.2 – DD-109M relationship between simulated activation and aluminum concentration

The activation relationship for the DD-109M is presented in Figure 4.2. From the equation of the trendline, we can predict the detection limit of the generator for Al-28. Assuming a neutron yield of 1 x 10^9 neutrons per second, irradiation and count times of 600 seconds, and a transfer time of 15 seconds, results in a detection limit of 3.85 x 10^1 µg Al per gram of bone.

The DD-109M can operate over a wide range of neutron yields, up to 5 x 10^9 neutrons per second. The greater the neutron yield, the greater the amount of activation, and the lower the detection limit. Detection limits of the DD-109M at difference yield values are given in Table 4.8 for a 600 second irradiation, 15 second transfer, and a 600 second count.

Table 4.8 – DD-109M detection limits according to neutron yield

Neutron Yield (neutrons per second)	Detection Limit (mg Al per g bone)
1 x 10^9	3.85 x 10^{-2}
2 x 10^9	2.16 x 10^{-2}
3 x 10^9	1.59 x 10^{-2}
4 x 10^9	1.31 x 10^{-2}
5 x 10^9	1.14 x 10^{-2}
1 x 10^{10}	8.04 x 10^{-3}

4.4 Discussion and Conclusions

An experiment assessing manganese in human subjects was performed in Zunyi China. The primary goal of the study was to study manganese, which has vastly different physical properties compared to aluminum. The study included performing NAA of subjects' hands as well as mass spectrometry on fingernail samples. The mass spectrometry evaluated a variety of elements, including aluminum and raw spectra were acquired during the NAA process. These two aspects allowed the secondary assessment of aluminum loads in the subjects.

Analyzing the HPGe spectra for the 1.779 MeV aluminum-28 photopeak did not demonstrate significant signal above background for any of the irradiated subjects. As there were no significant signals, there was no correlation with the skeletal aluminum loads quantified by mass spectrometry. Al-28 signals were not found in the neutron activation analysis because the detection limit of the system exceeded bone aluminum concentrations that have been previously measured in healthy individuals, including those working with and internalizing aluminum. The detection limit of the system was negatively affected by the experimental design being optimized for manganese. A transfer time of 300 seconds between the end of the irradiation and the beginning of the HPGe spectra acquisition meant that more than two half-lives of aluminum-28 occurred. This results in a loss of 78.64% of the potential signal.

Utilizing simulations and calculations described earlier in this work, a detection limit for the experiment, performed in the same manner as was done in the Zunyi experiment was determined. The detection limit for aluminum-28 in a human hand following 600 seconds of irradiation, 300 seconds of transfer time, and a 300 second HPGe acquisition was determined to be 1.59×10^3 micrograms of aluminum per gram of bone. This detection limit exceeded the range of control subjects' bone Al concentrations reported in [19] of 0.6 to 5 micrograms of Al per g of bone as well as the measurements of two healthy Al welders of 29 and 18 micrograms of Al per g of bone. As the workers were not primarily in Al industries, it is reasonable to conclude that their bone Al concentrations were in normal ranges and therefore too low to be detected with the experimental parameters utilized. Significant improvement in the detection limit would have been realized if the transfer period were reduced and the data acquisition begun sooner. Allowing more than two half-lives to elapse before the data began to be collected resulted in the majority of potential signal being lost. As the experiment was developed to detect manganese which has a much longer half-life, the limitation of the transfer period was not as critical in

achieving the primary goal. Optimization of the detection level by adjustment of the experimental parameters may have led to detection of aluminum levels in some of the workers.

Utilizing MCNP simulation, limits for both the DD-108M and DD-109M neutron generators were estimated for the detection of aluminum in a human hand. Detection limit is strongly dependent on irradiation time, time between irradiation and detection, the amount of time the subject is counted, and neutron yield. A variety of detection limits were calculated to demonstrate how they are affected by changing the factors. An optimized experiment to detect the smallest amount of aluminum in a human hand should rely on an irradiation time of 600 seconds, a transfer time of 15 seconds, and a count time of 600 seconds. Using these parameters, the detection limit for the DD-108M was estimated to be 3.41×10^{-2} milligrams of aluminum per gram of bone and the detection limit for the DD-109M was estimated to be 3.85×10^{-2} milligrams of aluminum per gram of bone. The differences in the detection limits between the DD-108M and DD-109M generators are due to varying amounts of activation which itself is largely due to different moderator/reflector configurations. The assumed neutron yields were similar between the two generators, but it is noted that the DD-109M has the potential to operate up to 5×10^{9} neutrons per second. The greater the neutron yield, the greater the amount of activation, and the lower the detection limit. So, while the estimated detection limits were similar, the DD-109M has the ability to result in much lower levels of detection.

The detection limits of both neutron generators were found to be well below the assumed threshold for observing deleterious effects in humans [5 milligrams of aluminum per gram of bone]. Depending on the desired detection limit, the experimental parameters can be optimized in a different manner, namely, the irradiation period could be reduced. Radiation dose to the subject is linearly dependent with irradiation time. Reducing the irradiation period by one-half will reduce the radiation dose by one-half. If it is not necessary to achieve the smallest possible detection limit, then the irradiation period can be shortened, saving dose to the subject while still being capable of detecting aluminum at a significant level.

CHAPTER 5. CONCLUSIONS AND FUTURE WORK

The goals of this project were threefold: 1. To develop a simulation of a complete NAA system, 2. To describe the detection capabilities of the system for aluminum, and 3. To determine the capability of the system to measure aluminum in vivo in humans.

In pursuit of the first goal, MCNP6 was used to completely model an NAA system, from the neutron generator source to the HPGe detector. The development of the MNCP6 description of the neutron source included work on biasing the production of neutrons, a step frequently ignored by other authors. An activation experiment was conducted to compare the use of an isotropic neutron source and an anisotropic neutron source. The experiment determined that the relative amounts of activation were closely matched by the simulation incorporating neutron anisotropy. Following confirmation of the more accurate neutron source specification, phantoms containing three different quantities of aluminum, along with blank phantoms containing no added aluminum were simulated and analyzed by the NAA system. Comparison of the amount of simulated activation to the amount actually measured resulted in percent differences ranging between 9.54% to 23.10%. The simulated estimates of activation were all higher than the actual amount measured and given the narrow range of percent differences, this informs that the result contains a systematic error. Given all the potential factors that can and do go into creating a simulation model of a complex process, results that are within an order of magnitude must be considered successful. The most likely source of systematic error is the estimate of neutron yield, which was assumed to be constant, but which can vary even during an individual irradiation run of the generator. Improvement in the accuracy between simulation and experiment could be made by making a flux estimate for each measurement, rather than an assumption of constant flux. Such an estimate could be performed by irradiating an activation foil along with the sample being analyzed.

In addition to modelling the neutron generator in MCP6, the HPGe detector was also simulated. The simulation of the detector included not only a physical description of its dimensions and composition but also its response to radiation. A multinuclide source was measured on the detector and from the photopeaks of cobalt-60 and yttrium-88, the Gaussian Energy Broadening of the detector was estimated and incorporated into MCNP. This feature allowed the HPGe simulation to make accurate estimates of the detector response to a given

photon energy. Comparisons were made between actual photopeaks from cobalt-60 and yttrium-88 and simulated ones, and they show similar amounts of broadening. The ability to simulate a photopeak accurately is very powerful as it allows one to estimate energy resolution. This can be useful in determining if a given photopeak will be resolved from background and/or interference peaks. Additionally, an estimate for the efficiency for the aluminum-28 1.779 MeV gamma ray, based on counts in the simulated photopeak, was compared to the efficiency measured for yttrium-88, which has a similar photon energy. The comparison demonstrated a percent difference between the simulated and measured efficiencies of 34.3%. Given the small values of the efficiencies, which are sensitive to a number of errors, especially that of geometry, a result within an order of magnitude should be considered very good. The ability to simulate efficiency within an order of magnitude means that the MCNP6 techniques developed and explained herein can be used to estimate efficiencies and experiment parameters for other radionuclides. This would be especially useful in situations where it is not possible to get a calibrated source of a specific radionuclide under analysis. The parameters of a counting experiment can be determined and optimized completely through simulation. Finally, a comparison was made between an actually acquired spectrum from the 1.779 MeV photopeak of aluminum-28 to a simulated 1.779 MeV photopeak. The comparisons showed excellent agreement in terms of both shape as well as total area (i.e., number of counts). The difference between simulated and acquired counts was measured as 18.7%, adding to the evidence that the simulation of photon spectra can be performed accurately in MCNP6.

The second goal of this project was to determine the detection capability of the system for aluminum. Interestingly, detection limit is a term that has had a very flexible definition over the past 50 years. Clearly, detection depends on being able to positively identify a signal above a level of noise. When analyzing the 1.779 MeV gamma ray from aluminum-28, noise (background) takes on an interesting meaning. Being such a high energy gamma ray, the background noise from other photons is close to zero. While there is very little interference from non-aluminum-28 photons, there is an issue with aluminum being omnipresent on earth. When analyzing a sample potentially containing aluminum, you must be careful with environmental aluminum so that the analyte does not become contaminated. Additionally, as the non-contaminated background is essentially zero, care must be taken in describing the detection limit of the system. The most common detection limit calculations are based on the Gaussian

distribution. At extreme low-levels of counts such as we may have in a system that is analyzing high energy gamma rays, the Gaussian based detection limits may over-estimate the ability of the system to confidently detect signal. To limit this possibility, I have adopted a modified detection limit proposed by Joseph Alvarez that is Poisson based. This detection limit is more conservative and would lead to less false positives. Measurements were made on three different quantities of aluminum in the NAA system, along a set of blanks not containing any added aluminum. From these measurements, a calibration curve of the system was generated. The average number of counts in the blanks was 19.67. Using this as a background level, the detection limit of the system as derived by Alvarez would be 26.9 counts. Applying this to the calibration curve, yielded a result that the system could confidently identify a sample of 0.73 milligrams of aluminum at a false positive error rate equal to 5%.

The third and final goal was to determine the capability of the system to evaluate aluminum in humans in vivo. The possibility of having a system that can non-invasively measure a metal that is not supposed to be present in the body is attractive. In order to be a useful analysis technique, it has to be able to do so at a level that doesn't result in an unacceptably high radiation dose to the human subject and it has to be able to measure aluminum at a level that is physiologically meaningful, that is, it has to be at a level that the results of the measurement would inform on a decision of subsequent actions to take. In regards to radiation dose, MCNP6 modelling is able to powerfully estimate any number of radiation dose metrics, including absorbed dose, equivalent dose, and effective dose. To that end, a human hand phantom was developed in the MCNP6 input and simulated under conditions exact to those that the detection limit was measured, including voltage potential of the generator and irradiation time. A description of how to setup tallies to measure radiation dose was given and it included modifications for the measurement of absorbed dose, equivalent dose, and effective dose. Estimates of all three were given based on the simulation result. The simulated effective dose to a human subject from irradiation by the DD-109M neutron generator was estimated to be 5.1×10^{-4} Sv. This level of effective dose is less than 2% of the amount of radiation dose that is allowed of human research subjects undergoing radioactive drug research. Absorbed doses were also estimated and they demonstrated that they were at levels far below which any type of tissue reaction may be expected.

The second part of the third goal was to evaluate whether the system could be utilized to determine a physiologically significant quantity of aluminum in a human. The detection limit of the DD-108M neutron generator was estimated to be 3.41 x 10^{-2} milligrams of aluminum per gram of bone. The detection limit of the DD-109M neutron generator was estimated to be 3.85 x 10^{-2} milligrams of aluminum per gram of bone at a neutron yield of 1 x 10^{9} neutrons per second and as low as 1.14 x 10^{-2} milligrams per aluminum per gram of bone at a yield of 5 x 10^{9}. It is assumed that there is a threshold of 5 milligrams of aluminum per gram of bone, above which humans experience deleterious effects. Both the DD-108M and DD-109M systems could therefore be used as a tool to quickly and non-invasively determine who may have a level of aluminum burden in their skeleton that might lead to future health risks. Additionally, by doubling the number of HPGe detectors used to measure an irradiated hand, the efficiency of the system would be doubled, and the detection capability further improved by increasing the captured signal. A caveat must be included that aluminum is present everywhere. The amount of background aluminum can affect the detection limit of the system. Especially for scenarios that involve analyzing those working with aluminum, care must be taken to ensure they don't have aluminum on their skin. When irradiating and measuring a hand, there is no method for separating out signal from aluminum on the skin and that arising from aluminum incorporated in the bone.

The techniques described herein were applied to a set of data acquired on human subjects. The data were acquired to analyze manganese in two groups of workers and the NAA experiment parameters were optimized as such for that element. Unfortunately, given the significant physical differences between manganese and aluminum, an experiment optimized for one is probably not optimized for the other. As such, the delay between the conclusion of neutron irradiation and the start of photon detection was too great for aluminum assessment. Nevertheless, the experiment did present an opportunity to analyze the experimental design, as mass spectroscopy assessments on the workers did include aluminum. The greatest amount of aluminum measured in a worker that also had NAA data available was found to be 211 micrograms of aluminum per gram of fingernail. By simulation with MCNP and calculation, I was able to demonstrate the detection limit of the NAA experiment for aluminum to be 1.59 x 10^{2} micrograms of aluminum per gram of bone. These calculations confirm why no aluminum-

28 signal was observed in the NAA data, as the detection limit was greater than the skeletal Al concentration normally found in healthy adults.

Future work on this project will follow three lines. First, the greatest source of error between simulation and experiment was most likely due to assuming the neutron yield during the irradiation rather than actually measuring it. Development of a simple process to account for flux variations during the irradiation should lead to an improvement in the absolute quantification and will be conducted.

Second will be verification that the radiation dose estimates provided by the simulation are accurate. The radiation dose estimates are highly dependent on the neutron flux so this will have to follow development of an accurate flux estimate. Once that is complete, development on measurements of neutron absorbed doses can be conducted for comparison with simulation. Of course, neutron absorbed dose measurements are very complicated by themselves due to their high dependence on neutron kinetic energy, so this aspect is considered to require significant efforts.

Finally, development will go into better estimating detector efficiency for real world measurements. The detector efficiency was both measured and simulated in this project but efficiency is highly geometry dependent. Simulating different geometry efficiencies is straightforward and development will go into validating those simulations. Specifically, validating that efficiency simulations maintain accuracy when moving from small sources that are completely in the field of view of the detector to geometries that are larger than the detector. This has direct implications when measuring a human hand, whose surface area exceeds that of the HPGe detector.

APPENDIX A. DD-108M MCNP INPUT FILE

```
MCNPX Visual Editor Version X_24E
   1   208  -2.699 -1 2 IMP:N=1 IMP:P=1 IMP:E=1
   2   208  -2.699 -4 5 IMP:N=1 IMP:P=1 IMP:E=1
   3   208  -2.699 -6 IMP:N=1 IMP:P=1 IMP:E=1
   4   209   -8.94 -7 IMP:N=1 IMP:P=1 IMP:E=1
   5   209   -8.94 -8 IMP:N=1 IMP:P=1 IMP:E=1
   6   999 -1.69e-010 -2 4 IMP:N=1 IMP:P=1 IMP:E=1
   7   999 -1.69e-010 -5 6 7 8 9 10 IMP:N=1 IMP:P=1 IMP:E=1
   8   204 -0.001225 1 -3 15 16 17 24 25 26 27 28 29 31 &
32 33 34 35 50 51 52 53 54 55 56 57 58 65 66 67 69 70 &
71 72 73 74 75 76 77 78 79 80 82 84 86 87 88 89 &
90 91 92 93 94 95 96 97 98 99 100 101 102 103 104 105 106 &
107 108 109 110 111 112 113 114 115 116 117 118 120 121 &
122 123 124 125 126 127 128 129 130 131 132 133 134 135 136 &
137 138 139 140 141 142 143 144 145 146 147 148 149 150 151 &
152 IMP:N=1 IMP:P=1 IMP:E=1
   9   498   -4.54 -9 IMP:N=1 IMP:P=1 IMP:E=1
  10   498   -4.54 -10 IMP:N=1 IMP:P=1 IMP:E=1
  13   204 -0.001225 3 IMP:N=0 IMP:P=0 IMP:E=0
  15     1     -1 -15 IMP:N=1 IMP:P=1 IMP:E=1
  16     2   -1.85 -16 IMP:N=1 IMP:P=1 IMP:E=1
  17     1     -1 -17 IMP:N=1 IMP:P=1 IMP:E=1
  24   208    -2.699 -24 IMP:N=1 IMP:P=1 IMP:E=1
  25   208    -2.699 -25 48 IMP:N=1 IMP:P=1 IMP:E=1
  26   208    -2.699 1 -26 IMP:N=1 IMP:P=1 IMP:E=1
  27   208    -2.699 1 -27 30 IMP:N=1 IMP:P=1 IMP:E=1
  28   208    -2.699 -28 29 IMP:N=1 IMP:P=1 IMP:E=1
  29   999 1.69e-010 -28 -29 IMP:N=1 IMP:P=1 IMP:E=1
  30   999 1.69e-010 -30 IMP:N=1 IMP:P=1 IMP:E=1
  31   208   -2.699 1 -31 IMP:N=1 IMP:P=1 IMP:E=1
  32   208   -2.699 31 -32 IMP:N=1 IMP:P=1 IMP:E=1
  33   208   -2.699 -3 -33 37 IMP:N=1 IMP:P=1 IMP:E=1
  34   208   -2.699 33 -34 38 IMP:N=1 IMP:P=1 IMP:E=1
  35   208   -2.699 34 -35 39 IMP:N=1 IMP:P=1 IMP:E=1
  37   999  -1.69e-010 -33 -37 IMP:N=1 IMP:P=1 IMP:E=1
  38   999  -1.69e-010 -34 -38 IMP:N=1 IMP:P=1 IMP:E=1
  39   999  -1.69e-010 -35 -39 IMP:N=1 IMP:P=1 IMP:E=1
  49   999  -1.69e-010 -48 IMP:N=1 IMP:P=1 IMP:E=1
c table legs and supports at 1/2 density b/c not solid aluminum
  50   208  -1.34 -50 IMP:N=1 IMP:P=1 IMP:E=1
  51   208  -1.34 -51 IMP:N=1 IMP:P=1 IMP:E=1
  52   208  -1.34 -52 IMP:N=1 IMP:P=1 IMP:E=1
```

```
  53   208  -1.34 -53 IMP:N=1 IMP:P=1 IMP:E=1
  54   208  -1.34 -54 IMP:N=1 IMP:P=1 IMP:E=1
  55   208  -1.34 -55 IMP:N=1 IMP:P=1 IMP:E=1
  56   208  -1.34 -56 IMP:N=1 IMP:P=1 IMP:E=1
  57   208  -1.34 -57 IMP:N=1 IMP:P=1 IMP:E=1
  58   208  -2.699 -58 59 IMP:N=1 IMP:P=1 IMP:E=1
  59   999  -1.69e-010 -59 IMP:N=1 IMP:P=1 IMP:E=1
c 62 is a cookie cutter cell for creating a cross sectional view have to
c give an importance of 1 to use (uncomment surface also when using)
c   62   0         -62
c **************moderator cells******************
c  Part #B2-M-1
  65   256  -0.93 -65 66 IMP:N=1 IMP:P=1 IMP:E=1
c  Area cutout of Part #B2-M-1
  66   0         #1 #6 -66    IMP:N=1 IMP:P=1 IMP:E=1
c  Part #B2-M-2
  67   256  -0.93 -67 78 IMP:N=1 IMP:P=1 IMP:E=1
c  Part #B2-M-3
  69   256  -0.93 -69:-70:-71 IMP:N=1 IMP:P=1 IMP:E=1
c  Part #B2-M-4 Inside
  70   256  -0.93 -72 IMP:N=1 IMP:P=1 IMP:E=1
c  Part #B2-M-4 Outside
  71   256  -0.93 -73 IMP:N=1 IMP:P=1 IMP:E=1
c  Part #B2-M-5
  72   256  -0.93 -74:-75:-76 IMP:N=1 IMP:P=1 IMP:E=1
c   Part #B2-Mod-1 composed of polyethylene
  73   256 -0.93 -77 78 79 IMP:N=1 IMP:P=1 IMP:E=1
c   Part #B2-Mod-1 cylindrical cutout
  74  0  #1 #2 #3 #4 #5 #6 #7 #9 #10 &
#25 #27 #28 #29 #30 #35 #58 #59 #69 #75 #78 -78 IMP:N=1 IMP:P=1 IMP:E=1
c   Part #B2-Mod-1 cylindrical cutout
  75  0  #1 #2 #3 #4 #5 #6 #7 #9 #10 &
#25 #27 #28 #29 #30 #35 #58 #59 #69 -79 &
IMP:N=1 IMP:P=1 IMP:E=1
c   Part #B2-Mod-2 rectangular box composed of polyethylene
  76   256  -0.93 78 79 -80  IMP:N=1 IMP:P=1 IMP:E=1
c   Part #B2-Mod-3 rectangular box composed of polyethylene
  78   256  -0.93 78 79 -82 IMP:N=1 IMP:P=1 IMP:E=1
c   Part #B2-M-6 rectangular box composed of polyethylene
  80   256  -0.93 78 -84 IMP:N=1 IMP:P=1 IMP:E=1
c   Part #B5-T-Left-1 rectangular box composed of polyethylene
  82  256   -0.93 -86 87 88 89 IMP:N=1 IMP:P=1 IMP:E=1
c   Part #B5-T-Left-1 cylindrical cutout
   83 0 #1 #25 #26 #27 #28 #29 #30 #49 &
#58 #59 #66 #69 #85 #116 -89 IMP:N=1 IMP:P=1 IMP:E=1
c   Part #B5-T-Left-1 center rectangular cutout
```

```
   84 0 #1 #25 #26 #27 #28 #29 #30 #49 &
#58 #59 #66 #69 -87 IMP:N=1 IMP:P=1 IMP:E=1
c   Part #B5-T-Left-1 end rectangular cutout
   85 0 #1 #25 #26 #27 #28 #29 #30 #49 &
#58 #59 #66 #69 -88 IMP:N=1 IMP:P=1 IMP:E=1
c   Part #B5-T-Left-2 rectangular box
   86  256   -0.93 -90 91 92 IMP:N=1 IMP:P=1 IMP:E=1
c   Part #B5-T-Left-2 cylindrical cutout
   87 0 #1 #25 #26 #27 #28 #29 #30 #49 &
#58 #59 #66 #69 #88 #118 #119 #120 -92 IMP:N=1 IMP:P=1 IMP:E=1
c   Part #B5-T-Left-2 end rectangular cutout
   88 0 #1 #25 #26 #27 #28 #29 #30 #49 &
#58 #59 #66 #69 -91 IMP:N=1 IMP:P=1 IMP:E=1
c   Part #B5-T-Left-3 center rectangular box
   89   256   -0.93 -93 94 95 96 97 98 IMP:N=1 IMP:P=1 IMP:E=1
c   Part #B5-T-Left-3 cylindrical cutout
   90 0 #1 #25 #26 #27 #28 #29 #30 #49 &
#58 #59 #66 #69 #89 #93 #94 -94 IMP:N=1 IMP:P=1 IMP:E=1
c   Part #B5-T-Left-3 top rectangular box
   91   256   -0.93 -95 93 IMP:N=1 IMP:P=1 IMP:E=1
c   Part #B5-T-Left-3 bottom rectangular box
   92   256   -0.93 -96 IMP:N=1 IMP:P=1 IMP:E=1
c   Part #B5-T-Left-3 top rectangular cutout
   93 0 #1 #25 #26 #27 #28 #29 #30 #49 &
#58 #59 #66 #69 #89 #91 -97 IMP:N=1 IMP:P=1 IMP:E=1
c   Part #B5-T-Left-3 bottom rectangular cutout
   94 0 #1 #25 #26 #27 #28 #29 #30 #49 &
#58 #59 #66 #69 #89 #92 -98 IMP:N=1 IMP:P=1 IMP:E=1
c   Part #B5-T-Left-4 center rectangular box
   95   256   -0.93 -99 100 101 102 103 104 IMP:N=1 IMP:P=1 IMP:E=1
c   Part #B5-T-Left-4 cylindrical cutout
   96 0 #1 #25 #26 #27 #28 #29 #30 #49 &
#58 #59 #66 #69 #89 #99 #100 -100 IMP:N=1 IMP:P=1 IMP:E=1
c   Part #B5-T-Left-4 top rectangular box
   97   256   -0.93 -101 IMP:N=1 IMP:P=1 IMP:E=1
c   Part #B5-T-Left-4 bottom rectangular box
   98   256   -0.93 -102 IMP:N=1 IMP:P=1 IMP:E=1
c   Part #B5-T-Left-4 top rectangular cutout
   99 0 #1 #25 #26 #27 #28 #29 #30 #49 &
#58 #59 #66 #69 #95 #97 -103 IMP:N=1 IMP:P=1 IMP:E=1
c   Part #B5-T-Left-4 bottom rectangular cutout
   100 0 #1 #25 #26 #27 #28 #29 #30 #49 &
#58 #59 #66 #69 #95 #98 -104 IMP:N=1 IMP:P=1 IMP:E=1
c   Part #B2-M-7 rectangular box
   101  256   -0.93 -105 106 IMP:N=1 IMP:P=1 IMP:E=1
c   Part #B2-M-7 cylindrical cutout
```

```
   102  0   #1 #6 -106 IMP:N=1 IMP:P=1 IMP:E=1
c   Part #B5-T-Left-5 rectangular box
   103  256   -0.93 -107 108 109 110 IMP:N=1 IMP:P=1 IMP:E=1
c   Part #B5-T-Left-5 large cylindrical cutout
   104  0   #1 #25 #26 #27 #28 #29 #30 #49 &
#58 #59 #103 #138 -108 IMP:N=1 IMP:P=1 IMP:E=1
c   Part #B5-T-Left-5 lower small cylindrical cutout
   105  0   #103 #140 -109 IMP:N=1 IMP:P=1 IMP:E=1
c   Part #B5-T-Left-5 upper small cylindrical cutout
   106  0   #103 #140 -110 IMP:N=1 IMP:P=1 IMP:E=1
c   Part Reflector Bottom rectangular box
   107  256   -0.93 #1 #6 66 -111 IMP:N=1 IMP:P=1 IMP:E=1
c  Part Reflector-Middle-1 rectangular box
   109   256  -0.93 78 -112 IMP:N=1 IMP:P=1 IMP:E=1
c  Part Reflector-Middle-2 rectangular box
   110   256  -0.93 78 79 -113 IMP:N=1 IMP:P=1 IMP:E=1
c  Part Reflector-Middle-3 rectangular box
   111   256  -0.93 78 79 -114 IMP:N=1 IMP:P=1 IMP:E=1
c  Part Reflector-Middle-4 rectangular box
   112   256  -0.93 78 79 -115 IMP:N=1 IMP:P=1 IMP:E=1
c  Part Reflector-Middle-5 rectangular box
   113   256  -0.93 78 -116 IMP:N=1 IMP:P=1 IMP:E=1
c  Part Reflector Slab rectangular box
   114   256  -0.93 -117 IMP:N=1 IMP:P=1 IMP:E=1
c  Part Reflector-Turbo-1  rectangular box
   115   256  -0.93 89 -118 119 IMP:N=1 IMP:P=1 IMP:E=1
c  Part Reflector-Turbo-1 end rectangular cutout
   116 0 #1 #25 #26 #27 #28 #29 #30 #49 &
#58 #59 #66 #69 -119 IMP:N=1 IMP:P=1 IMP:E=1
c  Part Reflector-Turbo-2 and B5-T-Right-2 (thin part) rectangular base
  117   256  -0.93 -120 121 IMP:N=1 IMP:P=1 IMP:E=1
c  Part Ref-T-2/B5-T-R-2 (thin part)rect on top of base with cylinder cutout
  118   256  -0.93 92 -121 IMP:N=1 IMP:P=1 IMP:E=1
c  Part Ref-T-2/B5-T-R-2 (thin part)rect with larger radius cylinder cutout
  119   256  -0.93 #58 #59 -122 123 IMP:N=1 IMP:P=1 IMP:E=1
c  Part Reflector-Turbo-2/B5-T-R-2 (thin part)cylindrical cutout
  120 0 #1 #25 #26 #27 #28 #29 #30 #49 &
#58 #59 #66 #69 #86 #88 #117 #118 -123 IMP:N=1 IMP:P=1 IMP:E=1
c  Part Reflector-Turbo-2/B5-T-R-2 (thin part) rectangular top
  121   256  -0.93 -124 IMP:N=1 IMP:P=1 IMP:E=1
c  Part Reflector Top rectangular top
  122   256  -0.93 106 -125 IMP:N=1 IMP:P=1 IMP:E=1
c  Part B2-1 through B2-6
  123   256  -0.93 -126:-127 128 IMP:N=1 IMP:P=1 IMP:E=1
c  Area cutout of B2-1 through B2-6
  124   0     #127 -128 135   IMP:N=1 IMP:P=1 IMP:E=1
```

```
c  Part B2-7
   125   256  -0.93 -129:-130 131 132 IMP:N=1 IMP:P=1 IMP:E=1
c  Part B2-7 cutout
   126   0     #125 #136 -131:-132  IMP:N=1 IMP:P=1 IMP:E=1
c  Part B2-1-Middle
   127   256  -0.93 -133:-134 135 IMP:N=1 IMP:P=1 IMP:E=1
c  Part B2-1-Middle semicircle cutout
   128   0     #123 -135    IMP:N=1 IMP:P=1 IMP:E=1
c  Part B2-2-Middle through B2-6-Middle
   129   256  -0.93 128 -136 IMP:N=1 IMP:P=1 IMP:E=1
c  Part B5-T-Right-1
   130   256  -0.93 -137 IMP:N=1 IMP:P=1 IMP:E=1
c  Part B5-T-Right-2 rect. box (thin section part of Ref-Turbo-2)
   131   256  -0.93 -138 IMP:N=1 IMP:P=1 IMP:E=1
c  Part B5-T-Right-3
   132   256  -0.93 -139:-140 IMP:N=1 IMP:P=1 IMP:E=1
c  Part B5-T-Right-4
   133   256  -0.93 -141:-142:-143 IMP:N=1 IMP:P=1 IMP:E=1
c  Part B2-7-Middle rectangular block with semicircle cutout
   134   256  -0.93 -144 145 IMP:N=1 IMP:P=1 IMP:E=1
c  Part B2-1-Middle semicircle cutout
   135   0     #134 #137 -145    IMP:N=1 IMP:P=1 IMP:E=1
c  Part B2-7-Middle rectangular block with complex cutout
   136   256  -0.93 131 132 -146 IMP:N=1 IMP:P=1 IMP:E=1
c  Part B2-7-Middle rectangular block with complex cutout
   137   256  -0.93 145 -147 IMP:N=1 IMP:P=1 IMP:E=1
c  Part B5-T-Right-5 rectangular block
   138   256  -0.93 108 -148 149 IMP:N=1 IMP:P=1 IMP:E=1
c  Part B5-T-Right-5 rectangular cutout
   139   0     #138 -149    IMP:N=1 IMP:P=1 IMP:E=1
c  Part B5-Turbo-Cap rectangular block
   140   256  -0.93 109 110 -150 151 152    IMP:N=1 IMP:P=1 IMP:E=1
c  Part B5-Turbo-Cap cylindrical/rectangular cutout
   141   0     #140 -151:-152    IMP:N=1 IMP:P=1 IMP:E=1

c    Outside of outer casing
     1       rcc 0 0 0 39.242 0 0 7.62
c    Inside of outer casing
     2       rcc 0.3 0 0 38.642 0 0 7.32
c    Outside world void
     3        so 350
c    Outside of target casing
     4       rcc 3.7846 0 0 22.7 0 0 4.7752
c    Inside of target casing
     5       rcc 4.0846 0 0 22.1 0 0 4.4752
c    Electrode on inside of target casing
```

```
    6       rcc 4.0846 0 0 0.5382 0 0 1.143
c    1/2 of copper target V
    7  1  box 18.9484 -2.8575 0.5 0 5.715 0 -11.303 0 0 0 0 0.9491999
c    Other 1/2 of copper target V
    8  2  box 18.9484 -2.8575 -0.5 0 5.715 0 -11.303 0 0 0 0 -0.9491999
c    Titanium surface on 1/2 of copper target V
    9  1  box 18.9484 -2.8575 0.4492 0 5.715 0 -11.303 0 0 0 0 0.0508
c    Titanium surface on other 1/2 of copper target V
   10  2 box 18.9484 -2.8575 -0.4492 0 5.715 0 -11.303 0 0 0 0 -0.0508
c   tissue
   15       rpp 9 21 -14.31 -13.81 -23 -14
c   bone
   16       rpp 9 21 -15.32 -14.32 -23 -14
c   skin
   17       rpp 9 21 -15.83 -15.33 -23 -14
c table
   24       rpp -1.28 -0.1 -35.12 35.12 -35.12 35.12
c ion source port +y to cell 28
   25       rcc 16.50492 10.8 0 0 4.0 0 5.08
c cylinder 26.01 cm from endcap
   26       rcc 35.559 0 0 3.683 0 0 11.2395
c ion source port
   27       rcc 16.50492 7.621 0 0 1.9304 0 4.08
c ion source port
   28       rcc 16.50492 9.5515 0 0 1.2446 0 6.0
c inside ion source port
   29       rcc 16.50492 9.8515 0 0 0.6446 0 5.7
c inside ion source port
   30       rcc  16.50492 7.921 0 0 1.3304 0 3.78
c structure on end of generator (+x end)
   31       rcc  39.242 0 0 1.3462 0 0 5.207
c structure on +x end of surface 31
   32       rcc  40.5882 0 0 2.4638 0 0 1.9939
c structure -x to generator endcap
   33       rcc  -17.7666 0 0 16.4855 0 0 8.0772
c structure -x to surface 33
   34       rcc  -31.4462 0 0 13.679 0 0 2.6289
c structure +x to surface 34
   35       rcc  -26.8869 0 2.6289 0 0 100 4.5593
c cylinder inside cell 33 to hollow it out
   37       rcc  -16.7666 0 0 15.485 0 0 7.0772
c cylinder inside cell 34 to hollow it out
   38       rcc  -30.4462 0 0 12.67 0 0 1.6289
c cylinder inside cell 35 to hollow it out
   39       rcc  -26.8869 0 3.6289 0 0 98 3.5593
c inside surface 25 (ion source port)
```

```
  48       rcc  16.50492 11.1 0 0 3.4 0 4.78
c table leg 1
  50       rpp  -69.861 -1.281 30.48 34.29 30.48 34.29
c table leg 2
  51       rpp  -69.861 -1.281 30.48 34.29 -34.29 -30.48
c table leg 3
  52       rpp  -69.861 -1.281 -34.29 -30.48 30.48 34.29
c table leg 4
  53       rpp  -69.861 -1.281 -34.29 -30.48 -34.29 -30.48
c undertable support 1
  54       rpp  -5.091 -1.281 -29.479 29.479 -33.85 -30.039
c undertable support 2
  55       rpp  -5.091 -1.281 -29.479 29.479 30.039 33.85
c undertable support 3
  56       rpp  -5.091 -1.281 30.039 33.85 -29.479 29.479
c undertable support 4
  57       rpp  -5.091 -1.281 -33.85 -30.039 -29.479 29.479
c
  58       rcc  15.13841 14.986 0 0 15.3 0 6.5
  59       rcc  15.13841 15.286 0 0 14.7 0 6.2
c cutaway box for creating a cross sectional view
c   62       rpp  -34 63 0.1 36 -36 36
c Part #B2-M-1 surface creating the rectangular box
  65       rpp  0 2.54 -30.3276 30.1752 -30.1752 0
c Part #B2-M-1 cylindrical cutout
  66       rcc  0 0 0 2.54 0 0 15.24
c Part #B2-M-2 surface creating the rectangular box
  67       rpp  2.54001 7.95021 -30.3276 8.5852 -30.1752 0
c Part #B2-M-3 long and tall section
  69       rpp  7.95022 13.36042 -30.3276 8.5852 -30.1752 -23.1648
c Part #B2-M-3 long and shallow section
  70       rpp  7.95022 8.86462 -30.3276 8.5852 -23.1648 -13.6398
c Part #B2-M-3 short and tall section
  71       rpp  7.95022 13.36042 -30.3276 -8.6106 -13.6398 0
c Part #B2-M-4 inside rectangular box
  72       rpp  13.36043 18.77063 -30.3276 -8.6106 -13.6398 0
c Part #B2-M-4 outside rectangular box
  73       rpp  13.36043 18.77063 -30.3276 8.5852 -30.1752 -23.1648
c Part #B2-M-5 long and tall rectangular box
  74       rpp  18.77064 24.18084 -30.3276 8.5852 -30.1752 -23.1648
c Part #B2-M-5 long and shallow rectangular box
  75       rpp  21.46304 24.18084 -30.3276 8.5852 -23.1648 -13.6398
c Part #B2-M-5 short and tall rectangular box
  76       rpp  18.77064 24.18084 -30.3276 -8.6106 -13.6398 0
c Part #B2-Mod-1 rectangular box
  77       rpp  7.95022 13.36042 -8.61059 8.5852 -13.6398 0
```

```
c Part #B2-Mod-1 cylindrical cutout -> big
  78       rcc  2.54001 0 0 25.24754 0 0 8.128
c Part #B2-Mod-1 cylindrical cutout -> small out of side
  79       rcc  15.13842 6.1468 0 0 2.4384 0 5.588
c Part #B2-Mod-2 rectangular box
  80       rpp  13.36043 18.77063 -8.61059 8.5852 -13.6398 0
c Part #B2-Mod-3 rectangular box
  82       rpp  18.77064 24.18084 -8.61059 8.5852 -13.6398 0
c Part #B2-Mod-3 cylindrical cutout -> big
c  83       rcc  18.77064 0 0 5.4102 0 0 8.128
c Part #B2-M-6 rectangular box
  84       rpp  24.18085 27.78755 -30.3276 8.5852 -30.1752 0
c Part #B2-M-6 cylindrical cutout
c  85       rcc  24.18085 0 0 3.6068 0 0 8.128
c Part #B5-T-Left-1 rectangular box
  86       rpp  2.54001 27.78765 8.7377 14.1479 -30.1752 0
c Part #B5-T-Left-1 rectangular center cutout
  87       rpp  8.86461 21.43761 8.7377 14.1479 -23.1648 -13.6398
c Part #B5-T-Left-1 rectangular end cutout
  88       rpp  6.37541 23.90141 8.7377 14.1479 -2.286 0
c Part #B5-T-Left-1 cylindrical cutout
  89       rcc  15.13841 8.7377 0 0 5.4102 0 7.5946
c   Part #B5-T-Left-2 rectangular box
  90       rpp  2.54001 27.78765 14.14791 19.55811 -30.1752 0
c Part #B5-T-Left-2 rectangular cutout
  91       rpp  6.37541 23.90141 14.14791 19.55811 -2.286 0
c Part #B5-T-Left-2 cylindrical cutout
  92       rcc  15.13841 14.14791 0 0 5.4102 0 7.5946
c Part #B5-T-Left-3 center rectangular box
  93       rpp  6.37541 23.90141 19.55812 24.96832 -30.1752 -5.461
c Part #B5-T-Left-3 cylindrical cutout
  94       rcc  15.13841 19.55812 0 0 5.4102 0 7.5946
c Part #B5-T-Left-3 top rectangular box
  95       rpp  23.90141 27.78765 19.55812 24.96832 -30.1752 2.2606
c Part #B5-T-Left-3 bottom rectangular box
  96       rpp  2.54001 6.37541 19.55812 24.96832 -30.1752 2.2606
c Part #B5-T-Left-3 top rectangular cutout
  97       rpp  20.47245 23.95225 19.55812 24.96832 -11.176 -5.461
c Part #B5-T-Left-3 bottom rectangular cutout
  98       rpp  6.37541 9.85521 19.55812 24.96832 -11.176 -5.461
c Part #B5-T-Left-4 center rectangular box
  99       rpp  6.37541 23.90141 24.96833 30.37853 -30.1752 -5.461
c Part #B5-T-Left-4 cylindrical cutout
  100       rcc  15.13841 24.96833 0 0 5.4102 0 7.5946
c Part #B5-T-Left-4 top rectangular box
  101       rpp  23.90141 27.78765 24.96833 30.37853 -30.1752 2.2606
```

```
c Part #B5-T-Left-4 bottom rectangular box
  102       rpp  2.54001 6.37541 24.96833 30.37853 -30.1752 10.9474
c Part #B5-T-Left-4 top rectangular cutout
  103       rpp  20.47245 23.95225 24.96833 30.37853 -11.176 -5.461
c Part #B5-T-Left-4 bottom rectangular cutout
  104       rpp  6.37541 9.85521 24.96833 30.37853 -11.176 -5.461
c Part #B2-M-7 rectangular box
  105       rpp  27.78765 33.19785 -30.3276 30.37853 -30.1752 0
c Part #B2-M-7 cylindrical cutout
  106       rcc  27.78765 -0.0254 0 5.4102 0 0 11.7602
c Part #B5-T-Left-5 rectangular box
  107       rpp  0 33.1216 30.37854 35.75874 -30.1752 0
c Part #B5-T-Left-5 large cylindrical cutout
  108       rcc  15.1384 30.37854 0 0 5.3802 0 5.9944
c Part #B5-T-Left-5 lower small cylindrical cutout
  109       rcc  8.1534 30.37854 -9.8806 0 10.79041 0 1.1811
c Part #B5-T-Left-5 upper small cylindrical cutout
  110       rcc  22.1234 30.37854 -9.8806 0 10.79041 0 1.1811
c Part Reflector Bottom rectangular box
  111       rpp  0 2.54 -16.1163 16.1163 0.0001 16.1291
c Part Reflector Middle-1 rectangular box
  112       rpp  2.54001 7.62001 -16.1163 8.5852 0.0001 12.3191
c Part Reflector Middle-2 rectangular box
  113       rpp  7.62002 12.70002 -16.1163 8.5852 0.0001 12.3191
c Part Reflector Middle-3 rectangular box
  114       rpp  12.70003 17.78003 -16.1163 8.5852 0.0001 12.3191
c Part Reflector Middle-4 rectangular box
  115       rpp  17.78004 22.86004 -16.1163 8.5852 0.0001 12.3191
c Part Reflector Middle-5 rectangular box
  116       rpp  22.86005 27.73685 -16.1163 8.5852 0.0001 12.3191
c Part Reflector Slab rectangular box
  117       rpp  2.54001 27.73685 -16.1163 8.5852 12.3192 16.1291
c Part Reflector-Turbo-1 rectangular box
  118       rpp  2.54001 27.78765 8.7377 14.1479 0.0001 16.1291
c Part Reflector-Turbo-1 end rectangular cutout
  119       rpp  6.37541 23.95225 8.7377 14.1479 0.0001 2.286
c Part Reflector-Turbo-2 rectangular base
  120       rpp  2.54001 6.37541 14.14791 19.55811 0.0001 16.1291
c Part Reflector-Turbo-2 rectangle on top of rectangular base
  121       rpp  6.37542 12.59842 14.14791 19.55811 2.2861 16.1291
c Part Reflector-Turbo-2 rectangle with larger cylinder cutout
  122       rpp  12.59843 23.90143 14.14791 19.55811 2.2861 16.1291
c Part Reflector-Turbo-2 larger radius cylindrical cutout
  123       rcc  12.59843 14.14791 0.0001 0 2.1336 0 9.0678
c Part Reflector-Turbo-2 rectangular top
  124       rpp  23.90144 27.73684 14.14791 19.55811 0.0001 16.1291
```

```
c Part Reflector Top
  125       rpp  27.78765 33.19785 -16.1163 16.28151 0.0001 16.1291
c Parts B2-1 through B2-6 (long rectangle)
  126       rpp  0 27.7876 -30.3149 -16.11631 0.0001 30.1753
c Parts B2-1 through B2-6 short rectangle with semicircle cutout
  127       rpp  0 27.7876 -16.11631 0.01269 16.12911 30.1753
c Part B2-1 through B2-6 semicircle cutout
  128       rcc  0 0.01269 18.56751 27.7876 0 0 1.3208
c Part B2-7 (long rectangle)
  129       rpp  27.78761 33.19785 -30.3149 -16.11631 0.0001 30.1753
c Part B2-7 short rectangle with semicircle cutout
  130       rpp  27.78761 33.19785 -16.11631 0.01269 16.12911 30.1753
c Part B2-7 rectangular cutout
  131       rpp  27.78761 33.19785 -1.79071 1.79071 18.5675 22.9617
c Part B2-7 semicircle cutout
  132       rcc  27.78761 0.01269 18.56751 5.41024 0 0 1.8034
c Part B2-1-Middle (long rectangle)
  133       rpp  0 2.54 16.28152 30.37853 0.0001 30.1753
c Part B2-1-Middle short rectangle with semicircle cutout
  134       rpp  0 2.54 0.0127 16.28152 16.12911 30.1753
c Part B2-1-Middle semicircle cutout
  135       rcc  0 0.012 18.56751 2.54 0 0 1.8034
c Parts B2-2-Middle through B2-6-Middle rectangular blocks
  136       rpp  2.54001 27.7876 0.0127 8.6233 16.12911 30.1753
c Part B5-T-Right-1 rectangular block
  137       rpp  2.54001 27.7876 8.62331 14.03351 16.12911 30.1753
c Part B5-T-Right-2 rectangular block (thin section part of Ref-Turbo-2)
  138       rpp  2.54001 27.73684 14.14791 19.55811 16.12911 30.1753
c Part B5-T-Right-3 long bottom rectangular block
  139       rpp  2.54001 6.37541 19.55812 24.96832 2.2861 30.1753
c Part B5-T-Right-3 large rectangular block
  140       rpp  6.37541 27.7876 19.55812 24.96832 10.9729 30.1753
c Part B5-T-Right-4 bottom rectangular block
  141       rpp  2.54001 5.58801 24.96833 30.37853 10.9729 30.1753
c Part B5-T-Right-4 center rectangular block
  142       rpp  5.58801 13.9954 24.96833 30.37853 22.0736 30.1753
c Part B5-T-Right-4 top rectangular block
  143       rpp  13.9954 27.7876 24.96833 30.37853 10.9729 30.1753
c Part B2-7-Middle rectangular block with semicircle cutout
  144       rpp  27.78765 33.19785 16.28152 25.83192 0.0001 16.1291
c Part B2-7-Middle semicircle cutout
  145       rcc  27.78765 25.83192 7.5947 5.41024 0 0 1.6002
c Part B2-7-Middle rectangular block with complicated cutout
  146       rpp  27.78765 33.19785 0.0127 25.83192 16.12911 30.1753
c Part B2-7-Turbo rectangular block
  147       rpp  27.78765 33.19785 25.83193 30.35313 0.0001 30.1753
```

```
c Part B5-7-Right-5 rectangular block
  148       rpp  0 33.19785 30.37854 35.75874 0.0001 30.1753
c Part B5-7-Right-5 rectangular cutout
  149       rpp  5.588 13.9954 30.37854 35.75874 11.0999 19.6089
c Part B5-Turbo-Cap rectangular block
  150       rpp  0 33.19785 35.75875 41.16895 -30.1753 30.1752
c Part B5-Turbo-Cap cylindrical cutout (on top of rect. cutout)
  151       rcc  11.176 38.62895 14.8082 0 2.54 0 2.6416
c Part B5-Turbo-Cap rectangular cutout
  152       rpp  5.588 16.5354 35.75875 38.62895 10.9728 19.0754

mode n p e
m1    1001.70c      -0.101172  $soft tissue ICRU 4 component density=1.0 g/c
      6000.70c        -0.111
      7014.70c    -0.02790536
      7015.70c    -9.464e-005
      8016.70c     -0.7616075
      8017.70c   -0.0002205451
c aluminum added to bone, replacing calcium
m2    1001.70c  -0.047226966  $cortical bone ICRP density = 1.85 g/cc
      1002.70c  -0.000007356273355
      3006.70c  -0.000000002389741814
      3007.70c  -0.0000000290998064
      6000.70c  -0.144327096
      7014.70c  -0.0418322693
      7015.70c  -0.0001537949535
      8016.70c  -0.4454866692
      8017.70c  -0.000615263786
      12024.70c -0.0017411957
      12025.70c -0.0002204929681
      12026.70c -0.0002425797374
      13027.70c -0.00003 $0.00666 g Al
      15031.70c -0.1049651607
      16032.70c -0.0029927899
      16033.70c -0.00002357590969
      16034.70c -0.0001321298285
      16036.70c -0.0000004590861203
      20040.70c -0.20350685865699
      20042.70c -0.00135823787201569
      20043.70c -0.000283403574531866
      20044.70c -0.00437911004795165
      20046.70c -0.0000839714294909234
      20048.70c -0.000392566432870067
      24050.70c -0.0000000501704078
      24052.70c -0.0000009674476168
      24053.70c -0.0000001096955218
```

```
     24054.70c -0.000000000273032227
     29063.70c -0.0000005808688021
     29065.70c -0.0000002588524835
     30000.70c -0.00009971690266
     79197.70c -0.0000001364547089
m204  7014.70c     -0.7528855  $air (US S. Atm at sea level)
     7015.70c   -0.002750515
     8016.70c      -0.231387
     8017.70c   -8.79605e-005
     18036.70c     -3.9e-005
     18038.70c       -8e-006
     18040.70c     -0.012842
m208  13027.70c           -1  $aluminum
m209  29000.50c           -1  $natural copper
m256  1001.70c  -0.143711  $polyethylene
     6000.70c  -0.856289
m498  22046.70c     -0.076779  $Titanium
     22047.70c     -0.071584
     22048.70c     -0.739078
     22049.70c     -0.056228
     22050.70c     -0.056331
m999  7014.70c     -0.7528855  $air (1e-4 torr pressure)
     7015.70c   -0.002750515
     8016.70c      -0.231475
     8017.70c   -8.79605e-005
     18036.70c     -3.9e-005
     18038.70c       -8e-006
     18040.70c     -0.012842
*tr1 0 0 2.2  -8 90 -98 90 0 90 82 90 -8
*tr2 0 0 -2.2  8 90 -82 90 0 90 98 90 8
mt208 al27.12t
mt236 grph.10t
mt256 poly.10t
phys:n 20 20 0
phys:p 100 0
phys:e 100 0
sdef erg=fdir=d3 par=n pos=18.3 0 0 axs=0 0 1 ext=0 &
vec=0 0 1 dir=d2 ara=10 rad=2.0si2  L 14.5 0 0.0716  14.5 0 -0.0716
sp2  D 0.5 0.5
c  ****************************************
c  flux over a cell tally
c  ****************************************
c f4:n 16
c e4:n 1e-7 100i 2.5
c e4:n 1e-5 1e-4 1e-3 1e-2 1e-1 1 2 3 4 5 10 20
c  ****************************************
```

```
c  Point Detector - neutron flux
c  ****************************************
c f5:n 12 0 45 1
c  ****************************************
c  Neutron Equivalent Dose Calculation
c  Equivalent Dose in Sieverts, using ICRP 60 Wr
c  ****************************************
f56:n 15
e56 0.01 0.1 2 4.9 T
em56 8.0108865e-10 1.6021773e-9 3.2043546e-9 1.6021773e-9
f66:n 16
e66 0.01 0.1 2 4.9 T
em66 8.0108865e-10 1.6021773e-9 3.2043546e-9 1.6021773e-9
f76:n 17
e76 0.01 0.1 2 4.9 T
em76 8.0108865e-10 1.6021773e-9 3.2043546e-9 1.6021773e-9
c  ****************************************
c  Photon and Electron Equivalent Dose Calculation
c  Equivalent Dose in Sieverts per source neutron
c  ****************************************
f16:p,e 15 16 17
e16 20
em16 1.60217646e-10
c  ****************************************
c  Photon and Electron Equivalent Dose Calculation
f26:p,e 15 16 17
df26 IU=1 FAC=-3 LOG IC=99
c  ****************************************
c  Neutron Equivalent Dose MCNP Dose Calculation
c  ****************************************
f36:n 15 16 17
df36 IU=1 FAC=-3 LOG IC=99
c  ****************************************
c  ****************************************
c  Neutron Equivalent Dose with F4 Tally
c  ****************************************
f14:n 15
fm14 2.209157322 2 -1 -4
e14 0.01 0.1 2 4.9 T
em14 8.0108865e-10 1.6021773e-9 3.2043546e-9 1.6021773e-9
f24:n 16
fm24 2.209157322 2 -1 -4
e24 0.01 0.1 2 4.9 T
em24 8.0108865e-10 1.6021773e-9 3.2043546e-9 1.6021773e-9
f34:n 17
fm34 2.209157322 2 -1 -4
```

```
e34 0.01 0.1 2 4.9 T
em34 8.0108865e-10 1.6021773e-9 3.2043546e-9 1.6021773e-9
c  ****************************************
c  Neutron Equivalent Dose with +F6 Tally
c  ****************************************
c +f6 15 16 17
c e6 0.01 0.1 2 4.9 T
c em6 8.0108865e-10 1.6021773e-9 3.2043546e-9 1.6021773e-9
c  ****************************************
c  Photon Dose in Sv (or Gy b/c Wr=1)
c  ****************************************
f86:p 15
e86 20
em86 1.602173e-10
f96:p 16
e96 20
em96 1.602173e-10
f106:p 17
e106 20
em106 1.602173e-10
c  ****************************************
c  Neutron Activation Tally for cell 16
c  ****************************************
c f4:n 69
c calculates #al-28 atoms in cell 2 from (n,gamma) of Al-27 in atoms/cm3
c fm4 0.00000123871148745 208 102
c  ****************************************
c  Energy Deposition Tally
c  ****************************************
c  Energy deposited by both photons and neutrons, calculated in MeV/g
c f56:n,p 46
c  ****************************************
nps 10000000
```

APPENDIX B. DD-109M MCNP INPUT FILE

```
MCNPX Visual Editor Version X_24E
   1   208  -2.699 -1 :-20 :-21 :-22 :-23 :(-24 25 )
   2   204 -0.001225 1 2 3 4 5 6 7 8 9 10 11 12 13 14 15 16 17 18 19 &
20 21 22 23 24 25 90 97 98 99 100 101 103 104 105 106 &
107 108 109 110 111 112 113 114 115 116 117 118 119 120 121 122 &
123 124 126 -200
   3   256   -0.93 (-2 15 16 ):-3 :-4 :-5 :-6 :-7 15 17 18 19 #4
   4   204 -0.001225 #12 #13 -8
   5   204 -0.001225 200
   6   208  -2.699 (-9 10 ):(-11 12 ):(-13 14 )
   7     0        #3 #4 #12 #13 #14 -10
   8     0        #3 #4 #13 #14 -12 :-14
  10   317   -4.98 -15
  11   209   -8.96 #10 -16
  12   498  -4.506 -17
  13   208  -2.699 -18 19
  14     0        #4 #12 -19
  15     0        #6 #8 -25
  16   256   -0.93 -90
  17   252  -11.35 -100  $lead
  18   252  -11.35 -101  $lead
  20   256   -0.93 -103
  21   256   -0.93 -104
  22   256   -0.93 -105
  23   256   -0.93 -106
  25   256   -0.93 -107
  26   256   -0.93 -108
 305   256   -0.93 -109
 306   256   -0.93 -110
  30   492   -7.86 -111
  31   492   -7.86 -112
  32   492   -7.86 -113
  33   492   -7.86 -114
  34   492   -7.86 -115
  35   524   -0.64 -116
  36   492   -7.86 -117
  37   492   -7.86 -118
  38   492   -7.86 -119
  39   492   -7.86 -120
  40   492   -7.86 -121
  41   524   -0.64 -122
  42   252  -11.35 -123
  44   228   -2.35 -124
```

```
  47   256   -0.93 -126  $block opening to cave
  50   777  -19.3 -97 $gold foil
  51   777  -19.3 -98 $gold foil
  52   777  -19.3 -99 $gold foil

c    Aluminum cover - face
   1       rpp -20.3 20.3 -38.1 38.1 6.3325 6.65
c    square of moderator
   2       rpp -19.9824 19.9824 -6.2 33.8 2.5124 6.3324
c    moderator
   3       rpp -19.9824 -16.4774 -6.2 33.8 -6.052 2.5124
c    moderator
   4       rpp 16.4774 19.9824 -6.2 33.8 -6.052 2.5124
c    moderator
   5       rpp 10.4574 16.4774 -6.2 33.8 1.8774 2.5124
c    moderator
   6       rpp -16.4774 -10.4574 -6.2 33.8 1.8774 2.5124
c    outside of cylinder of moderator
   7       rcc 0 17.8 -6.052 0 0 8.5644 9.525
c    inside of cylinder of moderator
   8       rcc 0 17.8 -6.052 0 0 8.5644 8.67375
c    outside of aluminum cylinder, in contact with moderator
   9       rcc 0 17.8 0.5039 0 0 1.27 15.1765
c    inside of aluminum cylinder, in contact with moderator
  10       rcc 0 17.8 0.5039 0 0 1.27 12.7635
c    outside of aluminum cylinder (thinner), in contact with moderator
  11       rcc 0 17.8 -8.3861 0 0 8.89 13.9065
c    inside of aluminum cylinder (thinner), in contact with moderator
  12       rcc 0 17.8 -8.3861 0 0 8.89 12.7635
c    outside of aluminum cylinder (thicker)
  13       rcc 0 17.8 -30.2555 0 0 21.8694 15.1765
c    inside of aluminum cylinder (thicker)
  14       rcc 0 17.8 -28.3505 0 0 19.9644 12.7635
c    target:  copper/water mix
  15       rcc 0 17.8 2.5759 0 0 0.3175 1.905
c    target:  copper
  16       rcc 0 17.8 2.5124001 0 0 0.381 3.81
c    target:  titanium
  17       rcc 0 17.8 1.62339 0 0 0.889 2.2225
c    outside of aluminum skirt around target
  18       rcc 0 17.8 0.03589999 0 0 2.4765 6.2992
c    inside of aluminum skirt around target
  19       rcc 0 17.8 0.03589999 0 0 2.4765 2.2225001
c    Aluminum cover - top
  20       rpp -20.6175 20.6175 38.1 38.4175 -6.685 6.65
c    Aluminum cover - bottom
```

```
  21      rpp -20.6175 20.6172 -38.4175 -38.1 -6.685 6.65
c   Aluminum cover - side
  22      rpp -20.6175 -20.3 -38.1 38.1 -6.685 6.65
c   Aluminum cover - side
  23      rpp 20.3 20.6175 -38.1 38.1 -6.685 6.65
c   Aluminum cover - backplate
  24      rpp -20.6175 20.6175 -38.1 38.1 -7.002501 -6.685
  25      rcc 0 17.8 -7.1 0 0 0.6 15.2
c   The world
 200      sph 0 0 0 500
c ************************************************************
c moderator
  90      rpp -20.3 20.3 -38.1 38.422 6.66 12.16
c phantom
c  91       rcc 0 17.8 12.295 0 0 1 4.25
c gold foil
  97      rcc 0 17.8 12.295 0 0 0.00508 0.635
c gold foil
  98      rcc -51.5 17.8 12.295 0 0 0.00508 0.635
c gold foil
  99      rcc -51.6 17.8 0 0.00508 0 0 0.635
c lead
 100      rpp -9.525 9.525 12.72 22.85 12.17 12.295
c lead
 101      rpp -9.525 9.525 12.597 12.719 12.17 22.33
c moderator
 103      rpp 9.5251 40.6175 12.597 38.42 12.17 25.77
c moderator
 104      rpp -40.62 40.6175 -38.1 12.596 12.171 25.77
c moderator
 105      rpp -40.62 40.6175 -38.1 38.42 25.771 59.871
c moderator
 106      rpp -40.62 40.6175 44.02 71.02 -110.2555 59.871
c moderator
 107      rpp -40.62 9.5251 22.851 38.42 12.16 25.771
c moderator
 108      rpp -40.62 -20.62 -38.1 38.42 -70.2555 12.159
c moderator
 109      rpp -40.62 40.6175 -38.1 38.42 -110.2555 -70.2555
c moderator
 110      rpp 20.6175 40.6175 -38.1 38.42 -70.2555 12.17
c stainless steel
 111      rpp 38 40 38.42 40.42 -110.2555 59.871
c stainless steel
 112      rpp -40 -38 38.42 40.42 -110.2555 59.871
c stainless steel
```

```
  113        rpp -40.62 40.6175 40.42 42.42 30.42 32.42
c stainless steel
  114        rpp -40.62 40.6175 40.42 42.42 -12.42 -10.42
c stainless steel
  115        rpp -40.62 40.6175 40.42 42.42 -52.42 -50.42
c southern pine wood
  116        rpp -40.62 40.6175 42.42 44.02 -110.2555 59.871
c stainless steel
  117        rpp 38 40 71.02 73.02 -110.2555 59.871
c stainless steel
  118        rpp -40 -38 71.02 73.02 -110.2555 59.871
c stainless steel
  119        rpp -40.62 40.6175 73.02 75.02 -52.42 -50.42
c stainless steel
  120        rpp -40.62 40.6175 73.02 75.02 -12.42 -10.42
c stainless steel
  121        rpp -40.62 40.6175 73.02 75.02 30.42 32.42
c southern pine wood
  122        rpp -40.62 40.6175 75.02 76.62 -110.2555 59.871
c stainless steel
  123        rpp -40.62 40.6175 76.62 77.62 -110.2555 59.871
c concrete
  124        rpp -150 150 -53.3 -38.5 -150 150
c moderator
  126        rpp -40.62 -20.3 12.596 22.851 12.17 25.77

mode  n p e
m204  7014.70c     -0.7528855  $air (US S. Atm at sea level)
      7015.70c   -0.002750515
      8016.70c      -0.231387
      8017.70c   -8.79605e-005
      18036.70c     -3.9e-005
      18038.70c       -8e-006
      18040.70c     -0.012842
m208  13027.70c           -1  $aluminum
m209  29063.70c        0.6915  $natural copper
      29065.70c        0.3085
m228  1001.70c      -0.005558  $concrete (ordinary with ENDF-VI), 2.35
      8016.70c      -0.498076
      11023.70c     -0.017101
      12024.70c     -0.001999
      12025.70c     -0.000264
      12026.70c     -0.000302
      13027.70c     -0.045746
      14028.70c     -0.289486
      14029.70c     -0.015181
```

```
     14030.70c     -0.010425
     16032.70c     -0.001216
     16033.70c       -1e-005
     16034.70c     -5.7e-005
     19039.70c      -0.01788
     19040.70c       -2e-006
     19041.70c     -0.001357
     20040.70c      -0.08019
     20042.70c     -0.000562
     20043.70c      -0.00012
     20044.70c      -0.00188
     20046.70c       -4e-006
     20048.70c     -0.000186
     26054.70c     -0.000707
     26056.70c      -0.01139
     26057.70c     -0.000265
     26058.70c     -3.6e-005
m252  82206.70c     -0.242902  $lead density = 11.35 g/cm3
     82207.70c     -0.223827
     82208.70c      -0.53327
m256  1001.70c      -0.143711  $polyethylene
     6000.70c      -0.856289
m317  1001.70c          0.333  $copper and water mixture
     8016.70c          0.167
     29063.70c       0.34575
    29065.70c       0.15425
m492  6000.70c         -0.002  $Steel, HT9 Stainless,
     14028.70c     -0.003675
     14029.70c     -0.000193
     14030.70c     -0.000132
     15031.70c       -0.0003
     16032.70c     -0.000189
     16033.70c       -2e-006
     16034.70c       -9e-006
     23000.70c        -0.003
     24050.70c     -0.004799
     24052.70c     -0.096256
     24053.70c     -0.011123
     24054.70c     -0.002821
     25055.70c        -0.006
     26054.70c     -0.048409
     26056.70c     -0.780435
     26057.70c     -0.018188
     26058.70c     -0.002468
     28058.70c      -0.00337
     28060.70c     -0.001333
```

```
     28061.70c     -5.9e-005
     28062.70c     -0.000189
     28064.70c      -5e-005
     42092.70c     -0.001422
     42094.70c     -0.000905
     42095.70c     -0.001575
     42096.70c     -0.001668
     42097.70c     -0.000965
     42098.70c     -0.002463
     42100.70c     -0.001003
     74183.70c       -0.005
m498  22046.70c     -0.076779  $Titanium density 4.506 g/cm3
     22047.70c     -0.071584
     22048.70c     -0.739078
     22049.70c     -0.056228
     22050.70c     -0.056331
m524  1001.70c      -0.057889  $Southern Pine Wood, -.64
     6000.70c      -0.482667
     8016.70c      -0.459444
m777  79197.70c    1  $gold
imp:n   1 3r        0          1 37r        $ 1, 47
imp:p   1 3r        0          1 37r        $ 1, 47
imp:e   1 3r        0          1 37r        $ 1, 47
mt208 al27.12t
mt256 poly.10t
phys:n 20 20 0
phys:p 100 0
phys:e 100 0
sdef erg=fdir=d3 par=n pos=0 17.8 1.62338 axs=0 0 1 ext=0 &
vec=0 0 1 dir=d2 ara=10 rad=2.0
c ********************************************************************
c *  Reaction kinematics valid for deuteron kinetic energy = 110 keV *
c *  Reaction kinematics calculated with DROSG-2000                  *
c ********************************************************************
si2 L 1 0.999912028 0.999652741 0.999215271 0.998601995 0.997824541 &
0.996862316 0.995740805 0.994430298 0.992944828 0.991307631 0.989475339 &
0.987468954 0.985318642 0.98296744 0.980477623 0.977783237 0.974916815 &
0.971919946 0.968713242 0.965336099 0.961836881 0.958122893 0.954292506 &
0.950244253 0.94602881 0.941705652 0.937160258 0.932449975 0.927640831 &
0.922605429 0.917407699 0.912120116 0.906602609 0.90100132 0.895167868 &
0.889176915 0.883111416 0.876810691 0.870355696 0.863835505 0.857077397 &
0.85026037 0.843203841 0.835998956 0.828744666 0.821248805 0.81360845 &
0.805928282 0.798004853 0.789941019 0.781847028 0.773508466 0.765146196 &
0.756538698 0.74779809 0.739043499 0.730043012 0.720914077 0.711780905 &
0.702401554 0.693024454 0.683401201 0.673657707 0.663926213 0.653948927 &
0.643856583 0.633785968 0.623470308 0.613182832 0.602651022 0.592013179 &
```

0.581413184 0.570570241 0.55962691 0.548731033 0.537593975 0.52636233 &
0.515187671 0.503773977 0.49242356 0.480835744 0.469163327 0.457563562 &
0.445729165 0.433816346 0.421985437 0.409923034 0.397948631 0.385745023 &
0.373473545 0.361299106 0.348899199 0.336437906 0.324082536 0.311505793 &
0.298874241 0.286357333 0.273623491 0.261009993 0.248182704 0.235311749 &
0.22256955 0.209618563 0.196630695 0.183779793 0.170725434 0.157813385 &
0.144701602 0.131564359 0.118577272 0.105396307 0.092196799 0.079155056 &
0.065925598 0.05285883 0.03960861 0.026351421 0.013264113 6.12574e-17 &
-0.013264113 -0.026351421 -0.03960861 -0.05285883 -0.065925598 &
-0.079155056 -0.092196799 -0.105396307 -0.118577272 -0.131564359 &
-0.144701602 -0.157813385 -0.170725434 -0.183779793 -0.196630695 &
-0.209618563 -0.22256955 -0.235311749 -0.248182704 -0.261009993 &
-0.273623491 -0.286357333 -0.298874241 -0.311505793 -0.324082536 &
-0.336437906 -0.348899199 -0.361299106 -0.373473545 -0.385745023 &
-0.397948631 -0.409923034 -0.421985437 -0.433816346 -0.445729165 &
-0.457563562 -0.469163327 -0.480835744 -0.49242356 -0.503773977 &
-0.515187671 -0.52636233 -0.537593975 -0.548731033 -0.55962691 &
-0.570570241 -0.581413184 -0.592013179 -0.602651022 -0.613182832 &
-0.623470308 -0.633785968 -0.643856583 -0.653948927 -0.663926213 &
-0.673657707 -0.683401201 -0.693024454 -0.702401554 -0.711780905 &
-0.720914077 -0.730043012 -0.739043499 -0.74779809 -0.756538698 &
-0.765146196 -0.773508466 -0.781847028 -0.789941019 -0.798004853 &
-0.805928282 -0.81360845 -0.821248805 -0.828744666 -0.835998956 &
-0.843203841 -0.85026037 -0.857077397 -0.863835505 -0.870355696 &
-0.876810691 -0.883111416 -0.889176915 -0.895167868 -0.90100132 &
-0.906602609 -0.912120116 -0.917407699 -0.922605429 -0.927640831 &
-0.932449975 -0.937160258 -0.941705652 -0.94602881 -0.950244253 &
-0.954292506 -0.958122893 -0.961836881 -0.965336099 -0.968713242 &
-0.971919946 -0.974916815 -0.977783237 -0.980477623 -0.98296744 &
-0.985318642 -0.987468954 -0.989475339 -0.991307631 -0.992944828 &
-0.994430298 -0.995740805 -0.996862316 -0.997824541 -0.998601995 &
-0.999215271 -0.999652741 -0.999912028 -1
sp2 0.006420429 0.006420429 0.00641793 0.006412932 0.006407933 &
0.006402935 0.006392938 0.006382942 0.006372945 0.006360449 &
0.006345454 0.006330458 0.006312964 0.00629547 0.006275476 &
0.006255483 0.00623299 0.006207998 0.006183006 0.006158014 &
0.006130523 0.006100533 0.006070542 0.006040552 0.006008062 &
0.005975573 0.005940584 0.005905595 0.005868108 0.00583062 &
0.005793132 0.005753145 0.005715657 0.00567317 0.005633183 &
0.005590697 0.005548211 0.005503225 0.00545824 0.005415753 &
0.005368269 0.005323283 0.005278298 0.005230813 0.005183328 &
0.005135844 0.005088359 0.005040874 0.00499339 0.004945905 &
0.004895921 0.004848436 0.004798452 0.004750968 0.004703483 &
0.004653499 0.004606015 0.00455853 0.004508546 0.004461061 &
0.004413577 0.004366092 0.004318607 0.004273622 0.004226137 &
0.004181152 0.004136166 0.004091181 0.004046195 0.00400121 &

0.003958723 0.003916237 0.003873751 0.003831264 0.003791277 &
0.00375129 0.003711303 0.003671316 0.003633828 0.00359634 &
0.003558852 0.003523864 0.003488875 0.003453886 0.003421397 &
0.003388907 0.003356418 0.003326427 0.003296437 0.003266447 &
0.003238955 0.003211464 0.003183973 0.003158981 0.003133989 &
0.003111497 0.003089004 0.003066511 0.003046517 0.003026524 &
0.00300903 0.002991535 0.002974041 0.002959046 0.002944051 &
0.002929055 0.002916559 0.002904063 0.002894067 0.00288407 &
0.002874073 0.002866576 0.002859078 0.00285158 0.002846582 &
0.002841584 0.002839084 0.002836585 0.002834086 0.002831587 &
0.002831587 0.002834086 0.002834086 0.002836585 0.002841584 &
0.002844083 0.002849081 0.00285408 0.002861577 0.002869075 &
0.002876572 0.002886569 0.002894067 0.002904063 0.002916559 &
0.002926556 0.002939052 0.002951548 0.002966543 0.002979039 &
0.002994034 0.00300903 0.003026524 0.003041519 0.003059013 &
0.003076508 0.003094002 0.003113996 0.00313149 0.003151484 &
0.003171477 0.003191471 0.003213963 0.003233957 0.00325645 &
0.003276443 0.003298936 0.003321429 0.003343922 0.003368914 &
0.003391406 0.003413899 0.003438891 0.003463883 0.003486376 &
0.003511368 0.00353636 0.003561351 0.003586343 0.003611335 &
0.003636327 0.003661319 0.003686311 0.003711303 0.003736295 &
0.003761287 0.003786279 0.00381377 0.003838762 0.003863754 &
0.003888746 0.003913738 0.00393873 0.003963722 0.003986214 &
0.004011206 0.004036198 0.00406119 0.004083683 0.004108675 &
0.004131168 0.00415366 0.004176153 0.004201145 0.004223638 &
0.004243631 0.004266124 0.004288617 0.00430861 0.004328604 &
0.004351097 0.00437109 0.004388585 0.004408578 0.004428572 &
0.004446066 0.004463561 0.004481055 0.004498549 0.004516044 &
0.004531039 0.004548533 0.004563528 0.004576024 0.004591019 &
0.004606015 0.004618511 0.004631007 0.004643502 0.004653499 &
0.004665995 0.004675992 0.004685989 0.004695986 0.004703483 &
0.004710981 0.004718478 0.004725976 0.004733473 0.004738472 &
0.00474347 0.004748469 0.004750968 0.004755966 0.004758465 &
0.004760965 0.004760965 0.004763464 0.004763464
ds3 L 2.87434 2.8743 2.87419 2.87401 2.87374 2.87341 2.873 &
2.87252 2.87196 2.87133 2.87062 2.86984 2.86899 2.86806 &
2.86706 2.86599 2.86485 2.86363 2.86234 2.86098 2.85955 &
2.85805 2.85648 2.85483 2.85312 2.85134 2.84949 2.84757 &
2.84558 2.84353 2.8414 2.83922 2.83696 2.83464 2.83226 &
2.82981 2.8273 2.82472 2.82209 2.81939 2.81663 2.8138 &
2.81092 2.80798 2.80499 2.80193 2.79882 2.79565 2.79242 &
2.78914 2.78581 2.78242 2.77898 2.77549 2.77195 2.76836 &
2.76472 2.76103 2.75729 2.75351 2.74968 2.74581 2.74189 &
2.73793 2.73392 2.72988 2.72579 2.72167 2.71751 2.71331 &
2.70907 2.70479 2.70048 2.69614 2.69177 2.68736 2.68292 &
2.67845 2.67395 2.66942 2.66487 2.66029 2.65568 2.65105 &

```
2.6464 2.64172 2.63702 2.6323 2.62756 2.62281 2.61803 &
2.61324 2.60843 2.60361 2.59877 2.59392 2.58906 2.58419 &
2.57931 2.57441 2.56951 2.56461 2.55969 2.55477 2.54985 &
2.54492 2.53999 2.53506 2.53013 2.52519 2.52026 2.51533 &
2.51041 2.50548 2.50056 2.49565 2.49074 2.48584 2.48095 &
2.47607 2.47119 2.46633 2.46148 2.45664 2.45181 2.447 &
2.4422 2.43741 2.43265 2.42789 2.42316 2.41845 2.41375 &
2.40908 2.40442 2.39979 2.39518 2.39059 2.38602 2.38148 &
2.37696 2.37247 2.36801 2.36357 2.35916 2.35478 2.35043 &
2.3461 2.34181 2.33755 2.33331 2.32911 2.32495 2.32081 &
2.31671 2.31264 2.30861 2.30462 2.30066 2.29673 2.29284 &
2.28899 2.28518 2.28141 2.27767 2.27398 2.27032 2.2667 &
2.26313 2.25959 2.2561 2.25265 2.24924 2.24588 2.24256 &
2.23928 2.23604 2.23285 2.22971 2.22661 2.22356 2.22055 &
2.21759 2.21467 2.2118 2.20898 2.20621 2.20348 2.2008 &
2.19817 2.19559 2.19306 2.19058 2.18814 2.18576 2.18343 &
2.18114 2.17891 2.17673 2.1746 2.17252 2.17049 2.16852 &
2.16659 2.16472 2.1629 2.16113 2.15942 2.15776 2.15615 &
2.15459 2.15309 2.15164 2.15024 2.1489 2.14761 2.14638 &
2.14519 2.14407 2.143 2.14198 2.14101 2.14011 2.13925 &
2.13845 2.13771 2.13702 2.13638 2.1358 2.13528 2.13481 &
2.13439 2.13403 2.13373 2.13348 2.13329 2.13315 2.13307 2.13304
c  ****************************************
c  flux over a cell tally
c  ****************************************
f4:n 50
e4:n 1e-7 100i 3.0
f14:n 51
e14:n 1e-7 100i 3.0
f24:n 52
e24:n 1e-7 100i 3.0
c  ****************************************
c  Neutron Equivalent Dose with *F8 Tally
*f8:n 51
e8 0.01 0.1 2 20 T
c  divided em bins by cell mass of 120.7458
em8 6.6342745e-12 1.32685e-11 2.6537098e-11 1.32685e-11
c  ****************************************
c  Neutron Equivalent Dose Calculation
c  Equivalent Dose in Sieverts, using ICRP 60 Wr
c  ****************************************
c f56:n 15
c e56 0.01 0.1 2 4.9 T
c em56 8.0108865e-10 1.6021773e-9 3.2043546e-9 1.6021773e-9
c  ****************************************
c  Photon and Electron Equivalent Dose Calculation
```

```
c  Equivalent Dose in Sieverts per source neutron
c  ****************************************
c f16:p,e 15 16 17
c e16 20
c em16 1.60217646e-10
c  ****************************************
c  Photon and Electron Equivalent Dose Calculation
c f26:p,e 15 16 17
c df26 IU=1 FAC=-3 LOG IC=99
c  ****************************************
c  Neutron Equivalent Dose MCNP Dose Calculation
c  ****************************************
f36:n 50
df36 IU=1 FAC=-3 LOG IC=99
c  ****************************************
c  Neutron Equivalent Dose with F4 Tally
c  ****************************************
c f14:n 15
c fm14 2.209157322 2 -1 -4
c e14 0.01 0.1 2 4.9 T
c em14 8.0108865e-10 1.6021773e-9 3.2043546e-9 1.6021773e-9
c  ****************************************
c  Neutron Equivalent Dose with +F6 Tally
c  ****************************************
c +f6 15 16 17
c e6 0.01 0.1 2 4.9 T
c em6 8.0108865e-10 1.6021773e-9 3.2043546e-9 1.6021773e-9
c  ****************************************
c  Photon Dose in Sv (or Gy b/c Wr=1)
c  ****************************************
c f86:p 15
c e86 20
c em86 1.602173e-10
c  ****************************************
c  Neutron Activation Tally for cell 16
c  ****************************************
c f4:n 16
c calculates #al-28 atoms in cell 16 from (n,gamma) of Al-27 in atoms/cm3
c fm4 0.00001454488467 136 102
c sd4 1
c f8:n 16
c calculate number of atoms of Al-28 produced in cell 16
c ft8 res 8017 13028
c  ****************************************
c  Energy Deposition Tally
c  ****************************************
```

```
c  Energy deposited by both photons and neutrons, calculated in MeV/g
c f56:n,p 46
c  ****************************************
nps 10000000
```

APPENDIX C. HPGE MCNP INPUT FILE

```
MCNPX Visual Editor Version X_24E
   1     1   -5.32 -2 4 -3 (32 :11 :-33 )#17 #15 #14 #19 #40 #41 &
IMP:P=1 IMP:E=1
   2   208 -2.6989 (-24 25):(-27 26) IMP:P=1 IMP:E=1 $Al
   5   458   -1.38 5 -4 -46 -102 IMP:P=1 IMP:E=1 $mylar
 500   208 -2.6989 -5 500 -46 IMP:P=1 IMP:E=1
  10   204 -0.001225 -1 200 201 202 203 221 222 223 &
224 225 226 227 228 229 230 231 232 233 234 235 236 237 300 &
#1 #2 #5 #11 #14 #15 #17 #19 #20 #40 #41 #500 IMP:P=1 IMP:E=1
  11     0         1 IMP:P=0 IMP:E=0
  14     0         -49 -3 (-50 :51 ) IMP:P=1 IMP:E=1
  15     0         -52 102 53 -34 (36 :-35 :38 :-37 :41 :-40 :43 :-44 ) &
IMP:P=1 IMP:E=1
  17     1   -5.32 -3 -11 (-32 :19 )#14 IMP:P=1 IMP:E=1 $dead layer, inner
  18     1   -5.32 2 -52 (-33 :-3 )#40 #15 #19 #10 &
#500 #5 #42 #43 IMP:P=1 IMP:E=1$dead layer, outer crystal
  19   208 -2.6989 (-106 107):(-108 109):-110 IMP:P=1 IMP:E=1
  20   204 -0.001225 -107 IMP:P=1 IMP:E=1
  21   252  -11.35 -221 IMP:P=1 IMP:E=1
  22   252  -11.35 -222 IMP:P=1 IMP:E=1
  23   252  -11.35 -223 IMP:P=1 IMP:E=1
  24   252  -11.35 -224 IMP:P=1 IMP:E=1
  25   252  -11.35 -225 IMP:P=1 IMP:E=1
  26   252  -11.35 -226 IMP:P=1 IMP:E=1
  27   252  -11.35 -227 IMP:P=1 IMP:E=1
  28   252  -11.35 -228 IMP:P=1 IMP:E=1
  29   252  -11.35 -229 IMP:P=1 IMP:E=1
  30   252  -11.35 -230 IMP:P=1 IMP:E=1
  31   252  -11.35 -231 IMP:P=1 IMP:E=1
  32   252  -11.35 -232 IMP:P=1 IMP:E=1
  33   252  -11.35 -233 IMP:P=1 IMP:E=1
  34   252  -11.35 -234 IMP:P=1 IMP:E=1
  35   252  -11.35 -235 IMP:P=1 IMP:E=1
  36   252  -11.35 -236 IMP:P=1 IMP:E=1
  37     4   -0.64 -237 IMP:P=1 IMP:E=1
  40     1   -5.32 (-53 33 )(36 :-35 :38 :-37 :41 :-40 :43 :-44 )-34 -52 4 &
IMP:P=1 IMP:E=1 $outer dead layer in the rounded region
  41     1   -5.32 102 -52 -4 (-4 :-53 )#40 #15 IMP:P=1 &
IMP:E=1 $ dl on the top of the detector
  42   902   -1 -300 IMP:P=1 IMP:E=1 $phantom
  43   252  -11.35 -201:-202:-203 IMP:P=1 IMP:E=1
  44   252  -11.35 -200 IMP:P=1 IMP:E=1
```

```
  1     so 100  $world
  2     cx 3.775  $crystal
  3     px 4.91  $crystal
  4     px -4.24  $crystal
  5     px -4.28  $Al/Mylar window
500      px -4.29
 11     cx 0.7  $inside cylinder
 19     px -2.92
 24     rcc 8.46 0 0 0.3 0 0 4.28
 25     rcc 8.46 0 0 0.3 0 0 0.7
 26     rcc -4.269 0 0 12.729 0 0 4.2
 27     rcc -4.269 0 0 12.729 0 0 4.28
 32     sph -2.85 0 0 0.7
 33     tx -3.41 0 0 2.975 0.83 0.83
 34     px -3.41
 35     pz -2.975
 36     pz 2.975
 37     py -2.975
 38     py 2.975
 40      p 0 0.70710678859302 0.70710678859302 -2.99
 41      p 0 0.70710681270686 0.70710681270686 2.99
 43      p 0 0.70710678859302 -0.70710678859302 3
 44      p 0 0.70710678859302 -0.70710678859302 -3
 45     cx 4.2
 46     cx 4.28
 47     cx 4.7
 48     cx 4.85
 49     cx 0.5
 50     sph -2.85 0 0 0.5
 51     px -2.85
 52     cx 3.79
 53     tx -3.41 0 0 2.975 0.855 0.855
 54     cx 5.5
 55     cx 5.6
102      px -4.27
106      rcc 15.207 0 0 11.5 0 0 5.6
107      rcc 15.307 0 0 11.3 0 0 5.5
108      rcc -4.643 0 0 19.85 0 0 4.85
109      rcc -4.643 0 0 19.85 0 0 4.7
110      rcc -4.943 0 0 0.3 0 0 4.85
200      rpp -11.75 -4.944 -10 10 8.651 13.4
201      rpp -11.75 -4.944 -15.8 -5.8 -5.6 8.65
202      rpp -11.75 -7.2 -5.8 5.79 -5.6 8.65
203      rpp -11.75 -4.944 5.8 15.8 -5.6 8.65
221      rpp -4.943 4.793 -10 10 8.651 13.4
222      rpp 4.7931 14.793 -10 10 8.651 13.4
```

```
 223      rpp 14.793 24.7929 -10 10 8.651 13.4
 224      rpp 24.793 34.793 -10 10 8.651 13.4
 225      rpp -4.943 15.2069 -15.8 -5.79 -5.6 -0.85
 226      rpp -4.943 15.2069 -15.8 -5.79 -0.85 3.9
 227      rpp -4.943 15.2069 -15.8 -5.79 3.9 8.65
 228      rpp 15.207 35.207 -15.8 -5.79 -5.6 -0.85
 229      rpp 15.207 35.207 -15.8 -5.79 -0.85 3.9
 230      rpp 15.207 35.207 -15.8 -5.79 3.9 8.65
 231      rpp -4.943 15.2069 5.8 15.8 -5.6 -0.85
 232      rpp -4.943 15.2069 5.8 15.8 -0.85 3.9
 233      rpp -4.943 15.2069 5.8 15.8 3.9 8.65
 234      rpp 15.207 35.207 5.8 15.8 -5.6 -0.85
 235      rpp 15.207 35.207 5.8 15.8 -0.85 3.9
 236      rpp 15.207 35.207 5.8 15.8 3.9 8.65
 237      rpp -30 40 -30 40 -7.543 -5.601
 300      rcc -5.7 0 -3 0 0 2.829421211 0.75

mode  p
m1    32070       -0.20526  $Germanium
      32072       -0.27446
      32073       -0.07760
      32074       -0.36523
      32076       -0.07745
m4    1001        -0.059642  $wood, from pnnl, -0.64
      6000        -0.497018
      7014        -0.00497
      8016        -0.427435
      12000       -0.001988
      16000       -0.00497
      19000       -0.001988
      20000       -0.001988
m204  7014        -0.7528855  $air (US S. Atm at sea level)
      7015        -0.002750515
      8016        -0.231387
      8017        -8.79605e-005
      18036       -3.9e-005
      18038       -8e-006
      18040       -0.012842
m208  13027       -1  $aluminum
m252  80204       -0.014  $lead density = 11.34 g/cm3
      82206       -0.241
      82207       -0.221
      82208       -0.524
m458  1001        -0.04196  $Polyeth Terephthalate (Mylar),
      6000        -0.625016
      8000        -0.333024
```

```
m902  1001         -1
phys:p 4 0 0 0 0 J 0
nps 400000000
f8:p 1
e8 0 16384i 3.26362
ft8 geb 0.0016731 0.0002759 -0.0001063
sdef pos= -5.5 0 -2  rad=d1 ext=d2  erg=d3 axs=0 0 1 cel=42
si1 0 0.95
sp1 -21 1
si2 0 5
sp2 0 1 $uniform probability over range
si3 L 1.17149 1.33083 1.836
sp3 D 5.05875456615321E-01 4.665239295858052E-01 2.76006137996279E-02
```

REFERENCES

[1] Runge, J.M. (2018) Runge J.M. (2018) A Brief History of Aluminum and Its Alloys. In: *The metallurgy of anodizing aluminum*. Springer, Cham. https://doi.org/10.1007/978-3-319-72177-4_1

[2] Chemical Rubber Company, & Lide, D. R. (Eds.). (2003). *CRC handbook of chemistry and physics: A ready-reference book of chemical and physical data* (84th ed). CRC Press.

[3] Nordberg, G., Fowler, B. A., & Nordberg, M. (eds.). (2015). *Handbook on the toxicology of metals* (4th ed). Elsevier, Academic Press.

[4] Priest, N. D. (2004). The biological behaviour and bioavailability of aluminium in man, with special reference to studies employing aluminium-26 as a tracer: Review and study update. *J. Environ. Monit.*, *6*(5), 375–403. https://doi.org/10.1039/B314329P

[5] Becaria, A., Campbell, A., & Bondy, S. (2002). Aluminum as a toxicant. *Toxicology and Industrial Health*, *18*(7), 309–320. https://doi.org/10.1191/0748233702th157oa

[6] Gräske, A., Thuvander, A., Johannisson, A., Gadhasson, I., Schütz, A., Festin, R., & Wicklund Glynn, A. (2000). Influence of aluminium on the immune system – an experimental study on volunteers. *BioMetals*, 13, 123-133.

[7] Soni, M. G., White, S. M., Flamm, W. G., & Burdock, G. A. (2001). Safety evaluation of dietary aluminum. *Regulatory Toxicology and Pharmacology*, *33*(1), 66–79. https://doi.org/10.1006/rtph.2000.1441

[8] Pennington, J. A. T., & Schoen, S. A. (1995). Estimates of dietary exposure to aluminium. *Food Additives and Contaminants*, *12*(1), 119–128. https://doi.org/10.1080/02652039509374286

[9] Tomljenovic, L. (2011). Aluminum and alzheimer's disease: After a century of controversy, is there a plausible link? *Journal of Alzheimer's Disease*, *23*(4), 567–598. https://doi.org/10.3233/JAD-2010-101494

[10] Matczak, W., & Gromiec, J. (2002). Evaluation of occupational exposure to toxic metals released in the process of aluminum welding. *Applied Occupational and Environmental Hygiene*, *17*(4), 296–303. https://doi.org/10.1080/10473220252826600

[11] European Food Safety Authority (EFSA). (2008). Safety of aluminium from dietary intake - scientific opinion of the panel on food additives, flavourings, processing aids and food contact materials (Afc). *EFSA Journal*, *6*(7). https://doi.org/10.2903/j.efsa.2008.754

[12] Yokel, R. A., & McNamara, P. J. (2001). Aluminium toxicokinetics: An updated minireview. *Pharmacology and Toxicology*, *88*(4), 159–167. https://doi.org/10.1034/j.1600-0773.2001.d01-98.x

[13] Canada & Health Canada. (2021). *Guidelines for Canadian drinking water quality: Guideline technical document - aluminum.* https://epe.lac-bac.gc.ca/100/201/301/weekly_acquisitions_list-ef/2021/21-11/publications.gc.ca/collections/collection_2021/sc-hc/H144-13-18-2021-eng.pdf

[14] Chappard, D., Insalaco, P., & Audran, M. (2003). Aluminum osteodystrophy and celiac disease. *Calcified Tissue International*, *74*(1), 122–123. https://doi.org/10.1007/s00223-003-0001-0

[15] Priest, N., Newton, D., Day, J., Talbot, R., & Warner, A. (1995). Human metabolism of aluminium-26 and gallium-67 injected as citrates. *Human & Experimental Toxicology*, *14*(3), 287–293. https://doi.org/10.1177/096032719501400309

[16] Talbot, R. J., Newton, D., Priest, N. D., Austin, J. G., & Day, J. P. (1995). Inter-subject variability in the metabolism of aluminium following intravenous injection as citrate. *Human & Experimental Toxicology*, *14*(7), 595–599. https://doi.org/10.1177/096032719501400707

[17] Krewski, D., Yokel, R. A., Nieboer, E., Borchelt, D., Cohen, J., Harry, J., Kacew, S., Lindsay, J., Mahfouz, A. M., & Rondeau, V. (2007). Human health risk assessment for aluminium, aluminium oxide, and aluminium hydroxide. *Journal of Toxicology and Environmental Health, Part B*, *10*(sup1), 1–269. https://doi.org/10.1080/10937400701597766

[18] Keith, L. S., Jones, D. E., & Chou, C.-H. S. J. (2002). Aluminum toxicokinetics regarding infant diet and vaccinations. *Vaccine*, *20*, S13–S17. https://doi.org/10.1016/S0264-410X(02)00165-2

[19] Elinder, C. G., Ahrengart, L., Lidums, V., Pettersson, E., & Sjogren, B. (1991). Evidence of aluminium accumulation in aluminium welders. *Occupational and Environmental Medicine*, *48*(11), 735–738. https://doi.org/10.1136/oem.48.11.735

[20] Riihimäki, V., Valkonen, S., Engström, B., Tossavainen, A., Mutanen, P., & Aitio, A. (2008). Behavior of aluminum in aluminum welders and manufacturers of aluminum sulfate—Impact on biological monitoring. *Scandinavian Journal of Work, Environment & Health*, *34*(6), 451–462. https://doi.org/10.5271/sjweh.1291

[21] DeKom, J. F. M., Dissels, H. M. H., Van DerVoet, G. B., & De Wolff, F. A. (1997). Serum aluminium levels of workers in the bauxite mines. *Journal of Toxicology: Clinical Toxicology*, *35*(6), 645–651. https://doi.org/10.3109/15563659709001248

[22] Sjogren, B., Lundberg, I., & Lidums, V. (1983). Aluminium in the blood and urine of industrially exposed workers. *Occupational and Environmental Medicine*, *40*(3), 301 –304. https://doi.org/10.1136/oem.40.3.301

[23] Bharathi, P., Vasudevaraju, M., Govindaraju, A. P., Palanisamy, K., Sambamurti, & Rao, K.S.J. (2008). Molecular toxicity of aluminium in relation to neurodegeneration. *Indian Journal of Medical Research, 128*, 545-556.

[24] Alfrey, A. C., Mishell, J. M., Burks, J., Contiguglia, S. R., Rudolph, H., Lewin, E., & Holmes, J. H. (1972). Syndrome of dyspraxia and multifocal seizures associated with chronic hemodialysis: *ASAIO Journal*, *18*(1), 257–261. https://doi.org/10.1097/00002480-197201000-00064

[25] Alfrey, A. C. (1993). Aluminum toxicity in patients with chronic renal failure: *Therapeutic Drug Monitoring*, *15*(6), 593–597. https://doi.org/10.1097/00007691-199312000-00025

[26] Cannata-Andia, J. B., & Fernandez-Martin, J. L. (2002). The clinical impact of aluminium overload in renal failure. *Nephrology Dialysis Transplantation*, *17*(suppl 2), 9–12. https://doi.org/10.1093/ndt/17.suppl_2.9

[27] Brown, R. O., Morgan, L. M., Bhattacharya, S. K., Johnson, P. L., Minard, G., & Dickerson, R. N. (2008). Potential aluminum exposure from parenteral nutrition in patients with acute kidney injury. *Annals of Pharmacotherapy*, *42*(10), 1410–1415. https://doi.org/10.1345/aph.1L061

[28] Aluminum in large and small volume parenterals used in total parenteral nutrition, Title 21 C.F.R. 201.323, (2021). https://www.ecfr.gov/cgi-bin/ECFR?page=browse

[29] K/doqi clinical practice guidelines for bone metabolism and disease in children with chronic kidney disease. (2005). *American Journal of Kidney Diseases*, *46*, 4. https://doi.org/10.1053/j.ajkd.2005.07.028

[30] Andress, D. L., Maloney, N. A., Endres, D. B., & Sherrard, D. J. (2009). Aluminum -associated bone disease in chronic renal failure: High prevalence in a long-term dialysis population. *Journal of Bone and Mineral Research*, *1*(5), 391–398. https://doi.org/10.1002/jbmr.5650010503

[31] Perl, DanielP., & Good, PaulF. (1987). Uptake of aluminium into central nervous system along nasal-olfactory pathways. *The Lancet*, *329*(8540), 1028. https://doi.org/10.1016/S0140-6736(87)92288-4

[32] Niu, Q. (Ed.). (2018). *Neurotoxicity of aluminum* (Vol. 1091). Springer Singapore. https://doi.org/10.1007/978-981-13-1370-7

[33] Verstraeten, S. V., Aimo, L., & Oteiza, P. I. (2008). Aluminium and lead: Molecular mechanisms of brain toxicity. *Archives of Toxicology*, *82*(11), 789–802. https://doi.org/10.1007/s00204-008-0345-3

[34] Gonçalves, P. P., & Silva, V. S. (2007). Does neurotransmission impairment accompany aluminium neurotoxicity? *Journal of Inorganic Biochemistry*, *101*(9), 1291–1338. https://doi.org/10.1016/j.jinorgbio.2007.06.002

[35] Igbokwe, I. O., Igwenagu, E., & Igbokwe, N. A. (2019). Aluminium toxicosis: A review of toxic actions and effects. *Interdisciplinary Toxicology*, *12*(2), 45–70. https://doi.org/10.2478/intox-2019-0007

[36] Stedman, J. D., & Spyrou, N. M. (1997). Elemental analysis of the frontal lobe of "normal" brain tissue and that affected by Alzheimer's disease. *Journal of Radioanalytical and Nuclear Chemistry*, *217*(2), 163–166. https://doi.org/10.1007/BF02034435

[37] Marchkesbery, W. R., Ehmann, W. D., Hossain, T. I. M., Alauddin, M., & Goodin, D. T. (1981). Instrumental neutron activation analysis of brain aluminum in Alzheimer disease and aging. *Annals of Neurology*, *10*(6), 511–516. https://doi.org/10.1002/ana.410100604

[38] Evans, R. D. (1955). *The atomic nucleus*. Tata McGraw-Hill.

[39] Shultis, J. K., Faw, R. E. (2002). *Fundamentals of nuclear science and engineering*. Marcel Dekker, Inc.

[40] Flugge, S. (1959). *Encyclopedia of physics: Neutrons and related gamma ray problems* (Vol. XXXVIII/2). Springer – Verlag.

[41] Bevelacqua, J. J. (2010). Standard model of particle physics—A health physics perspective. *Health Physics*, *99*(5), 613–623. https://doi.org/10.1097/HP.0b013e3181de7127

[42] Krane, K. S. (1988). *Introductory nuclear physics*. John Wiley & Sons.

[43] Shultis, J. K., Faw, R. E. (2000). *Radiation shielding*. American Nuclear Society, Inc.

[44] Almenas, K., Lee, R. (1992). *Nuclear Engineering*. Springer – Verlag.

[45] Magill, J., Galy, J. (2005). *Radioactivity radionuclides radiation*. Springer

[46] Report 10b, *Journal of the International Commission on Radiation Units and Measurements*, Volume os6, Issue 1, 31 March 1964, Page NP, https://doi.org/10.1093/jicru/os6.1.Report10b

[47] National Council on Radiation Protection and Measurements (Ed.). (1971). *Report No. 038 - Protection against neutron radiation.* National Council on Radiation Protection and Measurements.

[48] Schieck, H. P. (2014). *Nuclear reactions an introduction*. Springer.

[49] Nargolwalla, S. S., Przybylowicz, E. P. (1973). *Activation analysis with neutron generators.* John Wiley & Sons.

[50] International Atomic Energy Agency. (2012). *Neutron generators for analytical purposes, Radiation technology reports No. 1*. International Atomic Energy Agency.

[51] Greenberg, R. R., Bode, P., & De Nadai Fernandes, E. A. (2011). Neutron activation analysis: A primary method of measurement. *Spectrochimica Acta Part B: Atomic Spectroscopy*, *66*(3–4), 193–241. https://doi.org/10.1016/j.sab.2010.12.011

[52] Coyne, M. D., Neumann, C., Zhang, X., Byrne, P., Liu, Y., Weaver, C. M., & Nie, L. H. (2018). Compact DD generator-based *in vivo* neutron activation analysis (Ivnaa) system to determine sodium concentrations in human bone. *Physiological Measurement*, *39*(5), 055004. https://doi.org/10.1088/1361-6579/aabe66

[53] Liu, Y., Koltick, D., Byrne, P., Wang, H., Zheng, W., & Nie, L. H. (2013). Development of a transportable neutron activation analysis system to quantify manganese in bone *in vivo*: Feasibility and methodology. *Physiological Measurement*, *34*(12), 1593–1609. https://doi.org/10.1088/0967-3334/34/12/1593

[54] Mostafaei, F., Blake, S. P., Liu, Y., Sowers, D. A., & Nie, L. H. (2015). Compact DD generator-based neutron activation analysis (Naa) system to determine fluorine in human bone *in vivo*: A feasibility study. *Physiological Measurement*, *36*(10), 2057–2067. https://doi.org/10.1088/0967-3334/36/10/2057

[55] Davis, K., Aslam, Pejović-Milić, A., & Chettle, D. R. (2008). *In vivo* measurement of bone aluminum in population living in southern Ontario, Canada. *Medical Physics*, *35*(11), 5115–5123. https://doi.org/10.1118/1.2996177

[56] Gräfe, J. L., McNeill, F. E., Byun, S. H., Chettle, D. R., & Noseworthy, M. D. (2011). The feasibility of in vivo detection of gadolinium by prompt gamma neutron activation analysis following gadolinium-based contrast-enhanced MRI. *Applied Radiation and Isotopes*, *69*(1), 105–111. https://doi.org/10.1016/j.apradiso.2010.07.023

[57] Knoll, G. F. (2000). *Radiation detection and measurement* (3rd edition). John Wiley & Sons, Inc.

[58] Taylor, J. R. (1997). *An introduction to error analysis* (2nd edition). University Science Books.

[59] Bonamente, M. (2017). *Statistics and analysis of scientific data* (2nd edition). Springer.

[60] Justus, A. L. (2019). Multiple facets of the poisson distribution applicable to health physics measurements. *Health Physics*, *117*(1), 36–57. https://doi.org/10.1097/HP.0000000000001013

[61] Currie, L. A. (1968). Limits for qualitative detection and quantitative determination. Application to radiochemistry. *Analytical Chemistry*, *40*(3), 586–593. https://doi.org/10.1021/ac60259a007

[62] Strom, D. J., & MacLellan, J. A. (2001). Evaluation of eight decision rules for low-level radioactivity counting: *Health Physics*, *81*(1), 27–34. https://doi.org/10.1097/00004032-200107000-00005

[63] Miller, G., Martz, H. F., Little, T. T., & Guilmette, R. (2002). Using exact poisson likelihood functions in bayesian interpretation of counting measurements: *Health Physics*, *83*(4), 512–518. https://doi.org/10.1097/00004032-200210000-00009

[64] Klumpp, J., & Brandl, A. (2015). Simultaneous source detection and analysis using a zero -inflated count rate model. *Health Physics*, *109*(1), 35–53. https://doi.org/10.1097/HP.0000000000000291

[65] Rucker, T. L. (2001). Calculation of decision levels and minimum detectable concentrations from method blank and sample uncertainty data – utopian statistics. *Journal of Radioanalytical and Nuclear Chemistry, 248*(1), 191-196.

[66] Alvarez, J. L. (2007). Poisson-based detection limit and signal confidence intervals for few total counts. *Health Physics*, *93*(2), 120–126. https://doi.org/10.1097/01.HP.0000261331.73389.bd

[67] Hurtgen, C., Jerome, S., & Woods, M. (2000). Revisiting Currie—How low can you go? *Applied Radiation and Isotopes*, *53*(1–2), 45–50. https://doi.org/10.1016/S0969-8043(00)00171-8

[68] Potter, W. E. (1999). Neyman-pearson confidence intervals for extreme low-level, paired counting: *Health Physics*, *76*(2), 186–190. https://doi.org/10.1097/00004032-199902000-00011

[69] Brodsky, A. (1992). Exact calculation of probabilities of false positives and false negatives for low background counting. *Health Physics, 63*(2), 198-204.

[70] De Geer, L.-E. (2004). Currie detection limits in gamma-ray spectroscopy. *Applied Radiation and Isotopes*, *61*(2–3), 151–160. https://doi.org/10.1016/j.apradiso.2004.03.037

[71] Sood, A. (2017, July 10). The monte carlo method and MCNP – a brief review of our 40 year history [Powerpoint slides]. LA-UR-17-25633.

[72] Shonkwiler, R. W., Mendivil, F. (2000). *Explorations in monte carlo methods*. Springer.

[73] Goorley, J. T. et al. (2013). *Initial MCNP6 release overview – MCNP6 version 1.0*. Los Alamos National Laboratory. LA-UR-13-22934.

[74] Werner, C. J. (editor). (2017). *MCNP user's manual code version 6.2* (Revision 0). Los Alamos National Laboratory. LA-UR-17-29981.

[75] Jevremovic, T. (2009). *Nuclear principles in engineering*. Springer.

[76] Vainionpaa, J. H., Harris, J. L., Piestrup, M. A., Gary, C. K., Williams, D. L., Apodaca, M. D., Cremer, J. T., Ji, Q., Ludewigt, B. A., & Jones, G. (2013). *High yield neutron generators using the DD reaction*. 118–122. https://doi.org/10.1063/1.4802303

[77] Pelowitz, D. B. (editor). (2011). *MCNP user's manual version 2.7.0*. Los Alamos National Laboratory. LA-CP-11-00438.

[78] Adelphi Technology, Inc. (2016). *Neutron generator models DD-109M & DD110M operation manual*.

[79] Adelphi Technology, Inc. *DD109M specifications*. Technical specification.

[80] Parsons, D. K., White, M.C. (2014). *The los alamos CP2011 ACE format charged particle transport library for MCNP6*. Los Alamos National Laboratory, USA, LA-UR-14-23361.

[81] Drosg, M. (2016). DROSG-2000, *Codes and database for 60 neutron source reactions, documented in the IAEA report IAEA-NDS-87 Rev. 10*. International Atomic Energy Agency Nuclear Data Services.

[82] Hanson, A. O., Taschek, R. F., Williams, J. H. (1949). Monoergic neutrons from charged particle reactions. *Reviews of Modern Physics, 21*(4), 635-650.

[83] ICRP. (2002). Basic anatomical and physiological data for use in radiological protection reference values. ICRP Publication 89. *Annals of the ICRP 32*(3-4).

[84] ICRP. (1975). Report on the task group on reference man. ICRP Publication 23. Pergamon Press.

[85] White, D. R., Booz, J., Griffith, R. V., Spokas, J. J., Wilson, I. J. (1989). Report 44 Tissue substitutes in radiation dosimetry and measurement. *Journal of the International Commission on Radiation Units and Measurements, 23*(1). https://doi.org/10.1093/jicru/os23.1.Report44

[86] ICRP. (1991). 1990 recommendations of the international commission on radiological protection. ICRP Publication 60. *Annals of the ICRP 21*(1-3).

[87] Radioactive drugs for certain research uses, Title 21 C.F.R. 361.1, (2021). https://www.ecfr.gov/cgi-bin/ECFR?page=browse

[88] Cerrito, L. (2017). *Radiation and detectors introduction to the physics of radiation and detection devices*. Springer

[89] Lutz, G. (1999). *Semiconductor radiation detectors device physics*. Springer.

[90] Ortec. *GEM series coaxial HGPe detector product configuration guide*. Technical specification.

[91] Neumann, C. (2019). *In-vivo quantification of magnesium in hand bone using neutron activation analysis* [Unpublished master's thesis]. Purdue University.

[92] Kamboj, S., & Kahn, B. (1996). Evaluation of monte carlo simulation of photon counting efficiency for germanium detectors: *Health Physics*, *70*(4), 512–519. https://doi.org/10.1097/00004032-199604000-00008

[93] Browne, E., & Tuli, J. K. (2013). Nuclear data sheets for a = 251–259(Odd). *Nuclear Data Sheets*, *114*(8–9), 1041–1185. https://doi.org/10.1016/j.nds.2013.08.002

[94] McCutchan, E. A., & Sonzogni, A. A. (2014). Nuclear data sheets for a = 88. *Nuclear Data Sheets*, *115*, 135–304. https://doi.org/10.1016/j.nds.2013.12.002

[95] Liu, Y., Rolle-McFarland, D., Mostafaei, F., Zhou, Y., Li, Y., Zheng, W., Wells, E., & Nie, L. H. (2018). *In vivo* neutron activation analysis of bone manganese in workers. *Physiological Measurement*, *39*(3), 035003. https://doi.org/10.1088/1361-6579/aaa749

[96] Rolle-McFarland, D., Liu, Y., Mostafaei, F., Zauber, S. E., Zhou, Y., Li, Y., Fan, Q., Zheng, W., Nie, L. H., & Wells, E. M. (2019). The association of bone, fingernail and blood manganese with cognitive and olfactory function in Chinese workers. *Science of The Total Environment*, *666*, 1003–1010. https://doi.org/10.1016/j.scitotenv.2019.02.208

[97] McLachlan, D. R. C., Bergeron, C., Smith, J. E., Boomer, D., & Rifat, S. L. (1996). Risk for neuropathologically confirmed Alzheimer's disease and residual aluminum in municipal drinking water employing weighted residential histories. *Neurology*, *46*(2), 401–405. https://doi.org/10.1212/WNL.46.2.401

[98] Martyn, C. N., Osmond, C., Edwardson, J. A., Barker, D. J. P., Harris, E. C., & Lacey, R. F. (1989). Geographical relation between alzheimer's disease and aluminium in drinking water. *The Lancet*, *333*(8629), 59–62. https://doi.org/10.1016/S0140-6736(89)91425-6

[99] Parfitt, A. M. (1988). The localization of aluminum in bone: Implications for the mechanism of fixation and for the pathogenesis of aluminum-related bone disease. *The International Journal of Artificial Organs*, *11*(2), 79–90. https://doi.org/10.1177/039139888801100205

VITA

Curriculum Vitae: Patrick J. Byrne

Education

1995-1999	Purdue University, West Lafayette, IN
	B.S. Environmental Health
1999-2001	University of Michigan, Ann Arbor, MI
	M.Eng. Radiological Health

Awards

2013-2014	NIOSH Pilot Project Research Training Program Grant
2000-2001	Office of Civilian Radioactive Waste Management Fellowship
1999-2000	National Academy for Nuclear Training Graduate Fellowship
1998-1999	National Academy for Nuclear Training Undergraduate Scholarship

Certifications

American Board of Radiology (Medical Nuclear Physics)

American Board of Health Physics

American Board of Science in Nuclear Medicine (Physics and Instrumentation)

Memberships

Health Physics Society

Society of Nuclear Medicine and Molecular Imaging

American Association of Physicists in Medicine

American College of Radiology

PUBLICATIONS

Liu Y, Koltick D, **Byrne P**, Wang H, Zheng W, and Nie LH. Development of a Transportable Neutron Activation Analysis System to Quantify Mn in Bone In Vivo: Feasibility and Methodology. Physiol Meas. 34 (2013) 1593-1609.

Liu Y, **Byrne P**, Wang H, Koltick D, Zheng W, and Nie LH. A Compact DD Neutron Generator-based NAA System to Quantify Manganese (Mn) in Bone In Vivo. Physiol Meas. 35 (2014) 1899-1911.

Byrne P, Mostafaei F, Liu Y, Blake S, Koltick D, and Nie LH. The Study of In Vivo Quantification of Aluminum (Al) in Human Bone With a Compact DD Generator-based Neutron Activation Analysis (NAA) System. Physiol Meas. 37 (2016) 649-660.

Coyne M, Neumann C, Zhang X, **Byrne P**, Liu Y, Weaver C, and Nie LH. Compact DD Generator-based In Vivo Neutron Activation Analysis (NAA) System to Determine Sodium Concentrations in Human Bone. Physiol Meas. 39 (2018) 055004.

Byrne P, Coyne M, Nie LH. Improved MCNP Simulation Considering Neutron Angular Distribution and its Experimental Verification. Int J At Nucl Phys. (2020) 5:021.